DEPARTMENT OF MECHANICAL ENGINEERING AND MECHANICS
COLLEGE OF ENGINEERING AND TECHNOLOGY
OLD DOMINION UNIVERSITY
NORFOLK, VIRGINIA 23529

NUMERICAL STUDY OF THREE-DIMENSIONAL SEPARATION AND FLOW CONTROL AT A WING/BODY JUNCTION

By

Balakrishnan Lakshmanan, Graduate Research Assistant

Principal Investigator: Robert L. Ash

Progress Report
For the period ended April 30, 1989

Prepared for
National Aeronautics and Space Administration
Langley Research Center
Hampton, VA 23665

Under
Research Contract NAG-1-530
John B. Anders, Technical Monitor
HSAD-Viscous Flow Branch

August 1989

DEPARTMENT OF MECHANICAL ENGINEERING AND MECHANICS
COLLEGE OF ENGINEERING AND TECHNOLOGY
OLD DOMINION UNIVERSITY
NORFOLK, VIRGINIA 23529

NUMERICAL STUDY OF THREE-DIMENSIONAL SEPARATION AND FLOW CONTROL AT A WING/BODY JUNCTION

By

Balakrishnan Lakshmanan, Graduate Research Assistant

Principal Investigator: Robert L. Ash

Progress Report
For the period ended April 30, 1989

Prepared for
National Aeronautics and Space Administration
Langley Research Center
Hampton, VA 23665

Under
Research Contract NAG-1-530
John B. Anders, Technical Monitor
HSAD-Viscous Flow Branch

Submitted by the
Old Dominion University Research Foundation
P.O. Box 6369
Norfolk, Virginia 23508-0369

August 1989

NUMERICAL STUDY OF THREE-DIMENSIONAL SEPARATION AND FLOW CONTROL AT A WING/BODY JUNCTION

ABSTRACT

The problem of three-dimensional separation and flow control at a wing/body junction has been investigated numerically using a three-dimensional Navier-Stokes code. The numerical code employs an algebraic grid generation technique for generating the grid for unmodified junction and an elliptic grid generation technique for filleted fin junction. The results for laminar flow past a blunt fin/flat plate junction demonstrate that after grid refinement, the computations agree with experiment and reveal a strong dependency of the number of vortices at the junction on Mach number and Reynolds number. The numerical results for pressure distribution, particle paths and limiting streamlines for turbulent flow past a swept fin show a decrease in the peak pressure and in the extent of the separated flow region compared to the laminar case. The results for a filleted juncture indicate that the streamline patterns lose much of their vortical character with proper filleting. Fillets with a radius of three and one-half times the fin leading edge diameter or two times the incoming boundary layer thickness, significantly weaken the usual "necklace" interaction vortex for the Mach number and Reynolds number considered in the present study.

ACKNOWLEDGMENTS

This is a progress report for the research project "Studies of Vortex Stability and Control." The period of performance for the research is November 1, 1988 through April 30, 1989. The work was supported in part by the NASA Langley Research Center Grant NAG-1-530. The research grant was monitored by John B. Anders Jr. of the High-Speed Aerodynamics Division (Viscous Flow Branch).

TABLE OF CONTENTS

TABLE OF CONTENTS (continued)

TABLE OF CONTENTS (concluded)

LIST OF FIGURES

LIST OF FIGURES (Continued)

LIST OF FIGURES (Continued)

LIST OF FIGURES (Continued)

LIST OF FIGURES (Concluded)

LIST OF SYMBOLS

a	Speed of sound
CFL	Courant Fredrich Levy number
C_{cp}	Turbulence model constant
C_f	Skin friction coefficient
C_{kleb}	Turbulence model constant
D	Van Driest damping factor and diameter of the fin
E	Total energy per unit mass ($E = e_i + 1/2\ (u^2 + v^2 + w^2)$)
e_i	Specific internal energy ($e_i = c_v T$)
$\underline{F}$	Flux vector along the local coordinate direction
F_{kleb}	Klebanoff intermittency function
F_{max}	Velocity scale in outer turbulence model
F_{outer}	Outer function in outer turbulence model
F_{wake}	Wake function in outer turbulence model
$g^{1/2}$	Jacobian
$\underline{g}^{\ell}$	Contravariant base vector in the x^{ℓ} direction
$g^{\ell}_{(i')}$	Component of the contravariant base vector $\underline{g}^{\ell}$ along the x^{ℓ} direction
$g_{(i')}$	Contravariant unit base vector along the $x^{\ell'}$ direction
H	Height of the fin
i	Grid volume index in ξ-direction
j	Grid volume index in η-direction
k	Turbulence model constant ($k = 0.0168$); thermal conductivity; grid index in ζ-direction.
ℓ	Buleev length scale and separation length

LIST OF SYMBOLS (Continued)

ℓ_{max}	Length scale in outer turbulence model
$L\xi$, Ln, $L\zeta$	Explicit finite-difference operators in ξ, n, and ζ directions
M	Mach number
n	Coordinate normal to the surface
$\underline{n}$	Unit normal at surface
p	Static pressure
Pr_ℓ	Laminar flow Prandtl number
Pr_t	Turbulent flow Prandtl number
$\underline{q}$	vector of conserved variables
q_w	Heat flux at walk
R	Radius of the fillet at the juncture
Re_D	Reynolds number based on diameter ($Re_D = \rho U_\infty D/\mu_\infty$)
Re_ℓ	Unit Reynolds number based on free stream conditions
$\underline{S}$	Surface normal
T	Static temperature
T_w	Wall temperature
t	time
U	Streamwise velocity
u	Velocity in x-direction
v	Velocity in y-direction
w	Velocity in z-direction
u_ζ	Contravariant velocity component in ζ-direction
u_n	Contravariant velocity component in n-direction
u_ζ	Contravariant velocity component in ζ-direction
X_0	Distance from the flat plate leading edge to fin leading edge

LIST OF SYMBOLS (Continued)

x_{snock}	Location of the theoretical inviscid shock at a specified spanwise position
$x^{1'}, x^{2'}, x^{3'}$	Global cartesian coordinates ($(x^{1'}, x^{2'}, x^{3'}) = (x,y,z)$)
x_s	$x - x_{snock}$
x^1, x^2, x^3	Local body oriented coordinates ($(x^1,x^2,x^3) = (\xi,\eta,\zeta)$)

Greek Symbols

γ	Ratio of specific heats ($r = C_p/C_v$)
δ	Boundary layer thickness
ε	Dynamic turbulent eddy viscosity
ε_i, ε_o	Inner and outer dynamic turbulent eddy viscosity
ξ	Local body oriented coordinate
η	Local body oriented coordinate
ζ	Local body oriented coordinate
$\Delta\xi$	Mesh spacing in ξ-direction
$\Delta\eta$	Mesh spacing in η-direction
$\Delta\zeta$	Mesh spacing in ζ-direction
Δt_ξ, Δt_η, Δt_ζ	Time steps used for L_ξ, L_η, L_ζ operators
k	Von Karman's constant (k=0.4)
Λ	Fin sweep angle
λ	Second coefficient of viscosity ($\lambda = -2/3$)
μ	Dynamic molecular viscosity
ρ	Density
θ	Sharp fin leading edge angle
ϕ	Peripheral Angle in Buleev length scale and also angle measured in cylindrical coordinates from the fin nose
ω	Magnitude of vorticity ($\omega = \lvert \vec{\nabla} \times \vec{v} \rvert$)

Subscripts

0	Evaluated based on upstream conditions
sep	Based on separation conditions
w	Evaluated at wall
∞	Evaluated in freestream
t2	Total conditions behind the bow shock
$t\infty$	Total conditions of the freestream

Chapter 1

INTRODUCTION

Three-dimensional separation at intersecting surfaces such as wing-fuselage and wing-pylon junctions, and air breathing engine inlets is a complex physical phenomenon. The intersecting surface flow exhibits complex flow patterns which may significantly affect the performance of the aircraft. Major effects include increased pressure and heat transfer in the vicinity of the intersections and loss of control effectiveness due to flow separation. A variety of simplified geometrical configurations have been studied to gain insight into the physical aspects of three-dimensional separated flows including (1) sharp fin mounted on a flat plate, (2) blunt fin mounted on a flat plate, (3) swept compression corner, and (4) semicone affixed to a flat plate.

In the present work we concentrate our attention to the flow past a blunt fin/flat plate junction whch is a typical example of junction flow. When a high-speed flow passes over a blunt obstruction mounted on a flat plate the detached bow shock formed ahead induces a strong adverse pressure gradient to the plate boundary layer. This disturbance propagates through the subsonic portion of the boundary layer and can result in a 3-D separated flow region composed of horseshoe vortices near the plate surface and a lambda-type shock pattern ahead of the fin. These vortices entrain a part of the free-stream flow and spiral downstream. The separation shock emanating

from the separated flow region impinges on the fin shock producing a shock-shock interaction. Depending on the severity of the incoming shock, the shock-shock interaction leads to the formation of supersonic jet. This interaction leads to intense heating and high pressure locally around the fin leading edge.

Extensive experimental and computational studies pertinent to the physics of the problem have been carried out in the past for flow past a wing/body junction and these are reviewed briefly in Chap. 2. The description of the governing equations and all possible boundary conditions employed in the study is given in Chap. 3. The development of the finite volume concept, method of solution and operation of the numerical code are given in detail in Chap. 4. The specific physical conditions of investigation are described in Chap. 5 and discussion of all results are provided in Chap. 6.

Chapter 2

PHYSICS OF WING/BODY JUNCTURE FLOWS

In this chapter, the physics of wing/body juncture flows at low speed and high speed are discussed. Key findings from the previous studies have been included in the physics of the problem to indicate the characteristics of the junction flow. The discussion begins with detailed description of low speed unmodified juncture flows for laminar, turbulent and transitional conditions. Next, the description of controlled juncture flows are presented. The high speed unmodified and modified juncture flows is considered next to clearly highlight the difference in the flow structure with reference to low speed. Finally the status of turbulence modeling as applied to the computation of junction flow is briefly reviewed.

2.1 Low Speed Flows

2.1.1 Low Speed Unmodified Juncture Flows

If a protuberance is placed on a flat plate over which there is a fluid flow, the protuberance produces an adverse pressure gradient in its vicinity. This adverse pressure gradient created upstream of the protuberance causes the plate boundary layer to deviate from the surface resulting in a three-dimensional separation. The separated boundary layer rolls up downstream of the separation line to form a system of vortices. These vortices are swept around the base of the

protuberance and assumes a characteristic shape which has led to its name the horseshoe vortex.

Norman [1]* investigated experimentally the basic features of secondary flows and the conditions under which these flows led to transition and turbulence. The experimental study defined and described qualitatively the vortex system, the horseshoe vortex system, the spiraling-trailing vortex system, the vortex system resulting from the instability of the top shear layer, and the interactions of these sytems on transition. Schwind [2] studied the low speed junction flow using smoke visualization technique and observed five types of vortex regimes. Schwind observed that as the velocity is increased the number of vortices observed also increases and at higher velocities the two clockwise rotating vortices began to oscillate with amplitude increasing with velocity. Schwind further points out that although the flow passed from regime 1 to regime 5 types as the velocity is increased, the velocity at which the flow changed from one regime to another was by no means well defined and different flow regimes could exist at one velocity. Baker [3] demonstrated experimentally the existence of both steady and unsteady vortex systems. The oscillatory behavior of the horseshoe vortex was found to be complex. As the Reynolds number is increased the steady horseshoe vortex system began to oscillate intermittently and randomly at two different frequencies. As the Reynolds number is increased further, the period of oscillation of the vortices became longer, the high frequency oscillation becoming more common. At yet higher Reynolds number the oscillations became irregular and the horseshoe vortex system became turbulent. It was

*Numbers in brackets indicate References.

concluded that the frequency of these oscillations is solely determined by the value of Reynolds number and the ratio of diameter of the protuberance to the incoming boundary layer thickness.

Kaul et al. [4] studied numerically the incompressible junction flow using the Navier-Stokes equations. The equations were cast in generalized coordinates, and solved in time as a hyperbolic system by adding a pressure term in the continuity equation. The equations were marched until steady state was reached. The calculations indicated a strong non-uniform pressure loading along the length of the cylinder. A new mechanism for the existence of recirculation bubbles behind the cylinder end walls with relatively low ratio of cylinder height to the incoming boundary layer thickness was observed.

The turbulent flow around a wing/body junction is much more complex than the laminar counterpart. It consists of a turbulent boundary layer interacting with a viscous wake that is pressure driven in some regions, Reynold's stress driven in other regions and viscous dominated in most other regions. The essential features of the flow and the horseshoe root vortex are shown in Fig. 2.1. The wing is partially submerged in the oncoming flat plate boundary layer. The body is sufficiently long that a turbulent boundary layer exists upstream of the wing. The flow around the wing outside the boundary layer is assumed to be inviscid. The vorticity present in the incoming boundary layer wraps around the wing leading edge to form a horseshoe vortex. The oncoming fluid is decelerated by the adverse pressure gradient created due to the presence of the wing leading to three-dimensional separation. It is in this part that the primary root vortex, and possibly secondary vortices are established.

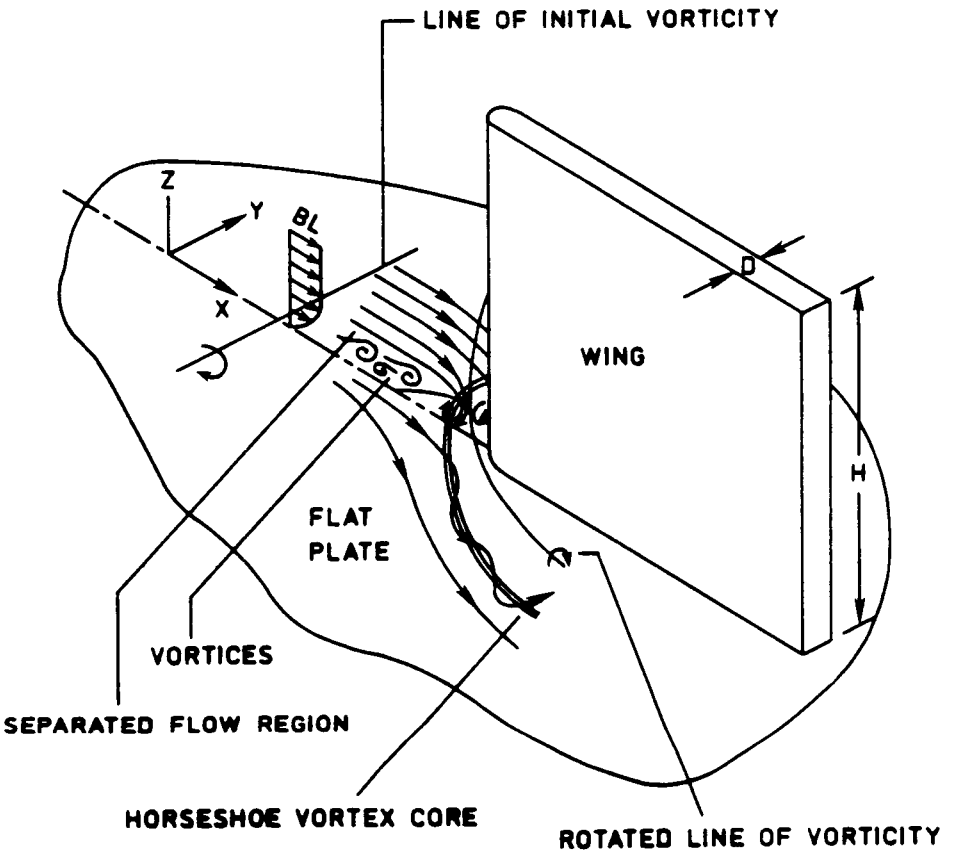

Fig. 2.1 Flow structure at the low speed wing/body junction.

Meanwhile, fluid off to the side of the wing, passes without experiencing much disturbance. Consequently, the fluid elements in one part of a vortical line are decelerated relative to fluid in other parts. The subsequent wrapping of the vortical line elements around the wing leading edge results in the appearance of horseshoe vortex. The effect of this skewing of the transverse vorticity line results in the generation of streamwise vorticity and a three-dimenstional flow velocity. Whereas, the flow upstream of the wing has one component velocity, which is directed in the streamwise direction, the flow in the root vortex has components in the plane normal to the streamwise direction due to the presence of streamwise vorticity. The horseshoe vortex experiences viscous diffusion and the effects of counter rotation takes place because of the anisotrophy of the Reynold's stresses. The flow slowly varies in the streamwise direction and is in some sense in equilibrium. The flow does not return to its original state downstream from the wing. Further, there are complex interactions between the vortices, the separated flow near the trailing edge and the viscous wake of the wing. The vortices remain immersed in the boundary layer from which they originated, and they do not lift up away from the body.

Shabaka and Bradshaw [5, 6] and Oguz [7] made mean flow and turbulence measurements in wing-fuselage junctions. The special emphasis of the experiment was to investigate the relative importance of turbulence terms and examine the spatial extent of the interaction flow field. McMahon et al. [8] studied the details of turbulent flow in a wing-fuselage type junction using surface oil-flow visualization technique combined with hot wire anemonemtry. The experimental data

collected includes measurement of three mean velocity components and six Reynolds stresses at selected streamwise locations. To complete the entire picture of the flow field some measurements were taken inside the reversed flow region using hot-wire techniques. It was shown that unambiguous measurements of the mean flow direction can be made in three-dimensional separated flows. The collected data have been used to deduce the flow behavior in and around the juncture. Also, the similarities between the mean-flow strain rates and the turbulent stresses, and the relative trends among the turbulence quantities have been discussed. Hsing and Teng [9] carried out experiments on the behavior of three-dimensional turbulent boundary layer in the simplified wing-body junction at low subsonic speed. The results of the boundary layer behavior in the attached flow region have revealed the effects of pressure gradient and curvature of the streamline. Briley and McDonald [10] studied numerically the wing/body junction flow with swept leading edges using the Navier-Stokes equations. A general nonorthogonal coordinate system that resolved the viscous sublayer was employed. The numerical predictions did not agree with measurements well downstream of the leading edge. The algebraic turbulence model employed in the study was fairly crude, but false diffusion errors, notoriously large in the recirculating region may have also contributed.

2.1.2 Low Speed Controlled Juncture Flows

The physics of low speed controlled juncture flows differ slightly from unmodified juncture flows in that the separation at the wing leading edge is eliminated by suitable geometrical modifications to

the wing. Such modifications include fillets, sweep and suction holes in the wing. These simple techniques help in improving the air flow around the wing/fuselage junctions and can be easily incorporated in existing fleets of aircraft. Preliminary results [11] indicate that there is some reduction in juncture drag at moderate angles of attack with the use of leading edge fillets. The use of sweep and suction at the wing leading edge considerably reduces the extent of separation and helps to maintain laminar flow around the juncture.

Mehta [12] experimentally investigated the effect of wing nose shapes on the nature of the generated secondary flow. The experimental study investigated in detail the correlation of the strength, size and position of the horseshoe vortex with the nose shape of the wing. The study clearly demonstrated that the nature of the horseshoe vortex system in a wing/body junction is strongly dependent on the wing nose shape with size and strength of the vortex system increasing with the nose bluntness. In most practical cases, this vortex flow persists right up to the wing trailing edge, with very little attenuation, so the only practical way to control it is by suitably adjusting the wing leading edge shape. Kubendran and Harvey [11] have made measurements in the wake region of a simulated wing-fuselage juncture, with and without leading-edge fillets, to understand the effect of leading edge modifications on the flow field around the juncture. Preliminary results have indicated some reduction in juncture drag using leading edge fillets at moderate angles of attack. Some improvements in the flow characteristics on the surface downstream of the juncture were also noticed when leading edge fillets were used. As the fillet size was increased, flow

characteristics start deteriorating at some point, and an optimum fillet size was needed to achieve an overall improvement in the flow field.

The numerical study of controlled juncture flows using fairings at the junction have been studied by Sung and Lin [13] and Kubendran et al. [14] using the incompressible Navier-Stokes equations. It has been found that the leading edge fairing is quite effective in reducing the leading edge flow separation and non-uniformity of the wave velocity profile and the addition of the trailing edge fairing can contribute to further improvement.

2.2 High Speed Flows

2.2.1 High Speed Unmodified Juncture Flows

High speed flow past a blunt fin mounted on a flat plate, results in a complex, three-dimensional, viscous-inviscid interaction flow field. The detached bow shock formed ahead of the protuberance causes the boundary layer to separate from the surface upstream of the fin location. This results in a separated flow region composed of horseshoe vortices near the surface and a lambda-type shock pattern in the plane of symmetry ahead of the fin. The major effects of the shock-wave/turbulent boundary-layer interaction are increased pressure loads and heat transfer levels on and in the vicinity of the protuberance. The existing experimental data suggest that the separated flow is very unsteady due to the oscillation of the separation location with amplitude larger than the undisturbed boundary layer thickness. This relatively large movement of the separation location is attributed to the pulsating and scavenging action of the flow comprising the multiple horseshoe vortices, results in comparatively large

oscillation of the impinging shock wave. In addition to the pressure peaks and heating rates at shock impingement on the fin leading edge, there are very large pressures and heating rates on the plate surface in the immediate vicinity of the fin root. It is believed that such shock wave turbulent boundary layer interactions have caused structural damage on hypersonic wing/body junctions [15].

Certain aspects of the separated flow ahead of a blunt fin are somewhat similar to two-dimensional separated flows ahead of ramps or steps. The pressure increase across the fin bow shock wave presents a strong adverse pressure gradient to the boundary layer flow on the flat plate surface, causing the boundary layer to separate adjacent to the plate surface. The effects of pressure increase are propagated upstream through the subsonic pocket of the boundary layer and leads to the separation of the boundary layer on the flat plate. As sketched in Fig. 2.2, the reversed flow forms a horseshoe vortex in which the flow quickly spirals downstream, away from the plane of symmetry. Immediately downstream of this vortex, there appears to be one or more additional vortices. The reversed flow in the vortices is constantly replenished by the separated stream flow, and spirals downstream very rapidly. Thus, the vortices bring the high energy air stream into proximity with the surface. Extremely high heating rates and large pressure fluctuations have been observed in local regions on the surface adjacent to the protuberance. The existing oil flow visualization techniques suggest that the direction of flow in the vortices is predominantly outboard and bears little similarity to two-dimensional separated flows in the plane of symmetry. The predominance of the transverse flow masks the nature of the flow along the

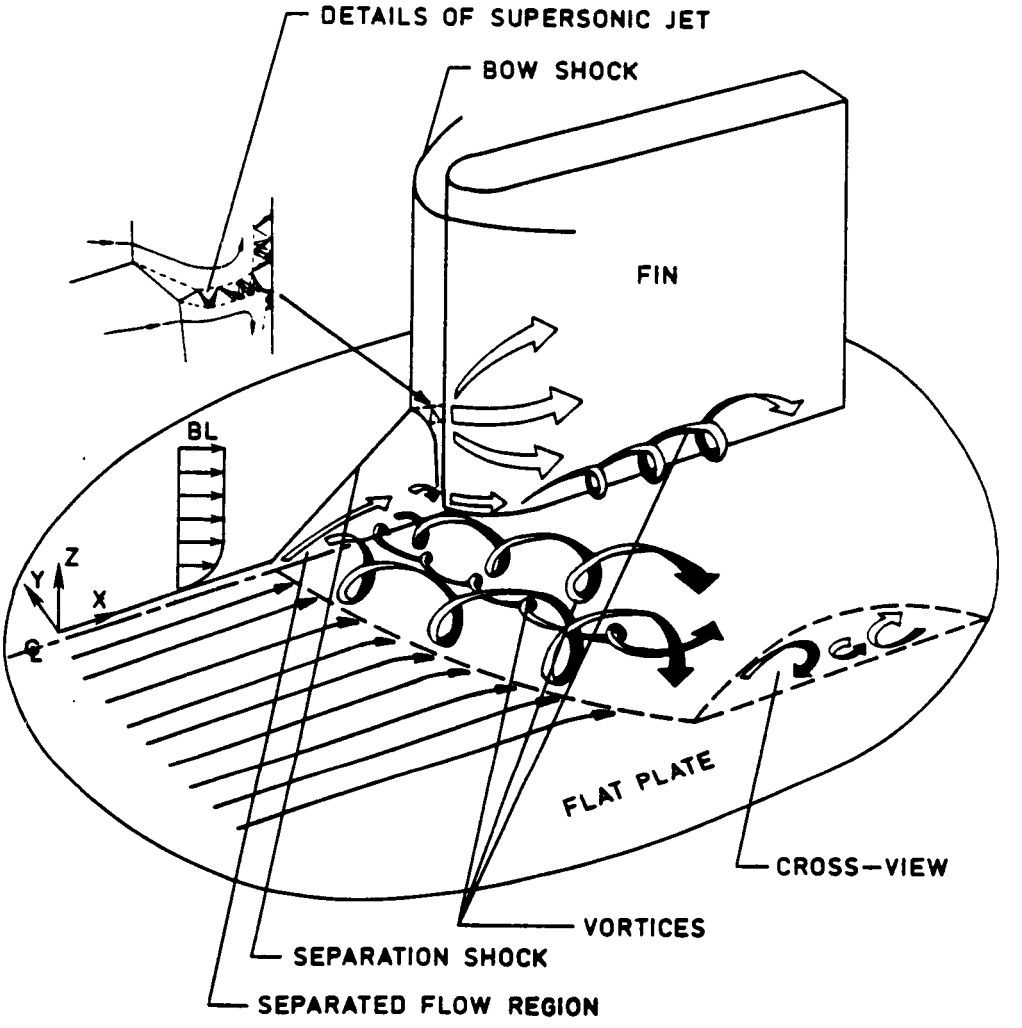

Fig. 2.2 Flow structure at the high speed wing/body junction.

boundary between two vortices, but there appears a third, small and counter rotating horseshoe vortex between the two large vortices. The flow at the root of the fin is highly three-dimensional and complex. There are large pressure, as well as high velocity gradients in this region. The compressed separated flow ahead of the fin accelerates to supersonic speeds in escaping around the fin to lower pressure regions. A strong vortex starts at the root of the fin and spreads out as it follows the fin root downstream. The fin bow shock causes the boundary layer to separate from the surface ahead of the fin, resulting in a separated flow region composed of horseshoe vortices near the surface, and a lambda-type shock pattern ahead of the fin. The shock wave emanating from the separated flow region impinges on the fin bow shock, and causes intense heating and high pressure locally around the fin leading edge.

Young et al. [16], Price and Stallings [17] and Westkaemper [18] observed that the extent of turbulent separation is insensitive to Mach number, Reynolds number and boundary layer thickness for a wide range of flow conditions, for fin diameters that are larger or comparable to the undisturbed boundary layer thickness. Specifically, for Mach numbers from 1.2 to 21, turbulent boundary layers separate approximately two diameters ahead of the fin leading edge. Laminar or transitional boundary layer separation ahead of a fin is much more extensive than turbulent separation and depends on both Mach number and Reynolds number. Limited data available in the literature indicate that the extent of separation ahead of a fin increases with increasing Reynolds number based on the separation distance. Laminar separation lengths exceeding six diameters have been observed by Young

et al. [16] for both Mach 3 and Mach 5 flows. However, separation is a strong disturbance to a laminar boundary layer and causes earlier transition than for attached, undisturbed boundary layers. In virtually all of the tests carried out in the earlier study [16], transition occurred either ahead of the separation location or in the free shear layer bounding the reverse flow region ahead of the fin (transitional separation). The extent of transitional separation diminished toward the turbulent value ($\ell_{sep} \rightarrow 2D$) as the separation location approaches the undisturbed boundary layer transitional location of the plate boundary layer. Mach number, Reynolds number, and boundary layer thickness effects on the extent of laminar or transitional separation have not been clearly differentiated.

Sidney [19] investigated experimentally the supersonic junction flow problem using flow visualization technique. The major objective of the experiment was to resolve the fine details of the flow structure. The variation of primary separation distance was discussed as a function of Mach number, Reynolds number and obstacle dimensions. The structure of the separated flow upstream of the obstacle was found to change with relatively small changes in Reynolds number. Experiments have been conducted by previous investigators to study the effect of transition properties on the diameter of the fin [17, 18, 20-27], sweep angle [17, 28, 29], height of the protuberance [17, 18, 20], Mach number [17, 20, 23, 25], and Reynolds number [17, 20, 25, 28, 29]. Attempts have been made to correlate the experimental data, but confusion over the conditions necessary for the model to be considered semi-infinite have caused some difficulty, particularly with respect to the vertical scale of the flow field. However most of the

experiments revealed clearly that the dominant parameters controlling the centerline flow field are the diameter and sweep angle of the fin. Dolling and Bogdonoff [30] studied experimentally blunt fin induced shock wave/turbulent boundary layer interaction. The first objective of the experiment was to investigate the spanwise development of the disturbed flow field and to determine its dependance on the model geometry and incoming flow conditions. The second objective of the experiment was to determine the vertical extent of the interaction on the fin. The results show that, on the test surface near the fin and on the fin itself, the leading edge diameter plays a dominant role in determining the interactions scale and characteristics.

Hung and Buning [31] studied the blunt fin induced shock wave/-turbulent boundary layer interaction problem using the 3D compressible Navier-Stokes equations. It was noted that varying the incoming boundary layer thickness by an order of magnitude showed that the size of the horseshoe vortex and the spatial extent of the interaction are dominated by inviscid flow and only weakly dependant on the Reynolds number. Hung [32] also noted that by changing the blunt fin to a flat faced fin the extent of separation increased drastically, and the main horseshoe vortex bifurcated into two vortices rotating in the same direction.

2.2.2 High Speed Controlled Juncture Flows

Very little work is done in high speed controlled juncture flows. Price and Stallings [17] and Stollery [33] studied the effect of fin sweep in turbulent boundary layers and noted that the separation of the flow ahead of the fin can be reduced drastically by leading edge

sweep. Gaitonde and Knight [34] studied numerically the effect of suction to control the sharp fin/flat plate junction flow. The computation indicated that the particular bleed schedule of five percent employed in the study was incapable of controlling or significantly modifying the undesirable separation and the large vortical structure. It may be possible to significantly influence the flow field by minor modifications to the configuration such as raising the fin a slight distance from the flat plate could provide interesting results.

2.3 Turbulence Modeling for Wing/Body Juncture Flows

Complex flows of the type found in wing/body junction are markedly influenced by three-dimensionality, pressure gradients, and viscous and turbulence effects. An important effect of calculating the flow described above is turbulence modeling. The simplest model used for the calculation of turbulent shear flows are algebraic eddy viscosity models [35]. These models have been employed primarily for calculating two-dimensional flows. However, the formulation of eddy viscosity models contain a large amount of empiricism that is generally not valid in complex three-dimensional flows. Three other types of turbulence models have been developed in the literature that are applicable to junction flow, such as two-equation models [36], algebraic Reynolds stress models [37], and the full Reynolds stress transport equations [38]. Of the models available, only the algebraic eddy viscosity model and the two equation models have been employed in the computation of wing/body junction flow [39]. The application of the full Reynolds stress transport equations to three-dimensional flows involve the solution of six additional partial differential equations for the

stresses and greatly increase the computational effort required. The algebraic Reynolds stress models have been developed as an attractive alternative to the full Reynolds stress equations. However, this model has not been refined sufficiently to make them applicable to three-dimensional flow fields. In particular, more work needs to be done before these models can adequately compute the near wall turbulence.

The literature review indicates that most of the experiments carried out in the junction flow lack detailed measurements in the separated flow region and do not sufficiently portray the structure of the vortical flow. The same level of criticism can be levelled against the previous computational studies in that they fail to examine the effect of grid refinement and turbulence model in the flow field simulation. Although techniques for controlling the junction flow have been studied experimentally and computationally in the past, quantitative information about their effect on the vortex strength is lacking in most of the earlier studies.

The primary objective of the present study is to obtain further understanding of the structure of resulting three-dimensional separation and to compute the junction flow with sufficient resolution. The specific objective of the study is to investigate numerically the effect of fillets and sweep in controlling the juncture horseshoe vortex and to provide quantitative information on the amount of weakening of the vortex.

Chapter 3

PHYSICAL MODEL AND THEORETICAL FORMULATION

In this chapter, a brief description of the governing partial differential equations representing the flow, along with the boundary and initial conditions employed in the present study are presented. The theoretical formulation of the problem starts with the nondimensional form of the compressible three-dimensional Navier-Stokes equations cast in the generalized body-oriented coordinate system. Brief discussions on the turbulence model, mesh system, and thin-layer approximation are also provided.

3.1 Governing Equations in Non-Dimensional Form

In the absence of body forces and source terms, the governing equations for the conservation of mass, momentum, and energy in a stationary control volume v, surrounded by a control surface S, can be expressed in integral form as [40]

$$\frac{\partial}{\partial t}\int_v \underline{q}\ dv + \int_s (\underline{q}\ \underline{u} + \underline{b}) \cdot \underline{n}\ ds = 0 \qquad (3.1)$$

where

$$\underline{q} = [\rho,\ \rho u,\ \rho v,\ \rho w,\ \rho E]^T$$

$$E = e_i + \frac{1}{2}(u^2 + v^2 + w^2)$$

$$\underline{b} = [\, \underline{b}_{\rho}, \underline{b}_{m}, \underline{b}_{e}]$$

$$\underline{b}_{\rho} = 0$$

$$\underline{b}_{m} = p\, \underline{\underline{I}} + M_{\infty}\, Re^{-1}\, \underline{\underline{\zeta}}$$

$$\underline{\underline{\zeta}} = -\lambda\, \mathrm{div}\, \underline{u}\, \underline{\underline{I}} - \mu\, [(\mathrm{grad}\, \underline{u}) + (\mathrm{grad}\, \underline{u})^{T}]$$

$$\underline{b}_{e} = -\gamma\, M_{\infty}\, (Re\ Pr)^{-1} \mu\ \mathrm{grad}\ e_{i} + p\underline{u} + M_{\infty}\, Re^{-1}\ \underline{\underline{\zeta}} \cdot \underline{u}$$

The nondimensionalization of the governing equations is carried out by normalizing the cartesian velocity components (u,v,w) by sound speed a_{∞}, the density ρ by ρ_{∞}, the specific internal energy e_i and the total energy E by a_{∞}^2, and p by $\rho_{\infty} a_{\infty}^2$. The viscosity coefficients λ and μ are normalized with respect to the molecular viscosity μ_{∞}. The constant γ, is the ratio of specific heats, Re is the Reynolds number based on freestream velocity, and Pr is the Prandtl number. The density ρ, static pressure p and the internal energy e_i are related through the following equations of state:

$$p = (1/\gamma)\, \rho T \tag{3.2}$$

$$e_i = T/\gamma(\gamma-1) \tag{3.3}$$

$$a^2 = T \tag{3.4}$$

where T is normalized by the freestream static temperature. Equation (3.1) is a simple expression for the basic conservation laws of fluid flow and is valid for a global control volume and also for each locally discretized control volume (i, j, k) shown in Fig. 3.1. For the sake of notational convenience, the superscript without a prime is used for the transformed coordinate (x^1, x^2, x^3) interchangeable with the local coordinates (ξ, η, ζ) and the superscript with a prime is used for the global coordinates (x,y,z). A similar notation convention is used for all other tensor quantities. For example, $u^{i'} = (u^{1'}, u^{2'}, u^{3'}) = (u,v,w)$.

The partial differential equation corresponding to Eq. (3.1) written in tensor convention is expressed as follows:

$$\frac{\partial}{\partial t}\left[\underline{q}\,(g)^{1/2}\right] + \frac{\partial}{\partial x^i}\left[\underline{q}\,\underline{u} + \underline{b}\right)\cdot\, g^{1/2}\,\underline{g}^i\right] = 0 \tag{3.5}$$

or

$$\underline{q}_{,t} + {}^{i}\underline{F}_{,i} = 0$$

$$\text{where } \underline{q} \equiv \underline{q}\,(g)^{1/2}, \quad {}^{i}\underline{F} \equiv \left[(\underline{q}\,\underline{u} + \underline{b})\cdot(g^{1/2})\,\underline{g}^i\right]$$

In eq. (3.5) $(g^{1/2})$ is the Jacobian and $\underline{g}^i$ is the contravariant base vector in the x^i direction. Here, the Einstein summation convention is used for repeated indices. Since Eq. (3.5) is a

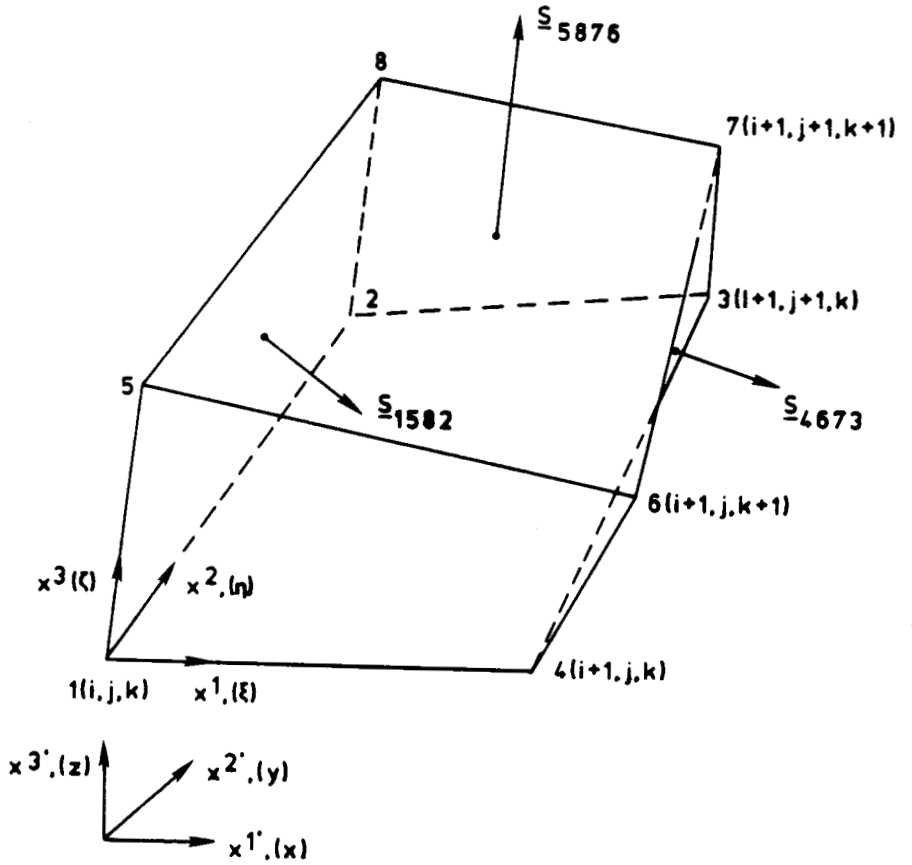

Fig. 3.1 A hexahedron finite volume v(i,j,k) with coordinate systems

homogeneous equation in $\underline{q}$, it can be written as

$$\tilde{q}_{,t} + (\overset{i}{\underline{\underline{A}}}\,\tilde{q})_{,i} = 0, \quad \tilde{q} \equiv \underline{q}_{,t} \quad \overset{i}{\underline{\underline{A}}} \equiv \partial \underline{F}^{i}/\partial \underline{q} \tag{3.6}$$

Equation (3.6) provides the basis for the implicit procedure. Writing Eq. (3.5) explicitly, one has

continuity

$$[(g)^{1/2}\,\rho]_{,t} + [\rho \underline{u}.(g)^{1/2}\,\underline{g}^{\ell}]_{,\ell} = 0 \tag{3.7a}$$

momentum for $x^{i'}$ direction

$$[(g)^{1/2}\,\rho u^{i'}]_{,t} + \{\rho \underline{u}^{i'}\underline{u} \cdot (g)^{1/2}\,\underline{g}^{\ell}_{(i')} + p(g)^{1/2} g^{\ell}_{(i')}$$

$$-M_{\infty}\,Re^{-1}\,\lambda\,\frac{\partial u^{n'}}{\partial x^{n'}}\,(g)^{1/2}\,g^{\ell}_{(i')}$$

$$-M_{\infty}\,Re^{-1}\,\mu\,\left[\frac{\partial u^{n}}{\partial x^{n'}}(g)^{1/2}\,g^{\ell}_{(n')} + \frac{\partial u^{i'}}{\partial x^{n'}}\,(g)^{1/2}\,g^{\ell}_{(n')}\right]\}_{,\ell} = 0 \tag{3.7b}$$

energy

$$[(g)^{1/2}\rho E]_{,\ell} + \{(\rho E + p)\underline{u}.(g)^{1/2}\underline{g}^{\ell}$$

$$- \frac{\gamma M_\infty}{Re}\frac{\mu}{Pr}\frac{\partial e_i}{\partial x^i}(g)^{1/2}g^{\ell}_{(i')} - \frac{M_\infty\lambda}{Re}\,\mathrm{div}\,\underline{u}\,\underline{u}\cdot(g)^{1/2}\underline{g}^{\ell}$$

$$- \frac{M_\infty\mu}{Re}\left[u^{m'}\frac{\partial u^{m'}}{\partial x^k}(g)^{1/2}\,g^{\ell}_{(k')} + u^{m'}\frac{\partial u^{n'}}{\partial x^{m'}}(g)^{1/2}\,g^{\ell}_{(n')}\right]\}_{,\ell} = 0 \quad (3.7c)$$

where $g^{\ell}_{(i')}$ is the component of the contravariant base vector $\underline{g}^{\ell}$ along the $x^{i'}$ direction and $g_{i'}$ is the contravariant unit base vector.

The above system of equations is assumed to be valid for turbulent flows if the molecular transport coefficients are replaced by

$$\mu = \mu_\ell + \mu_t \quad (3.8a)$$

$$\frac{\mu}{Pr} = \frac{\mu_\ell}{Pr_\ell} + \frac{\mu_T}{Pr_t} \quad (3.8b)$$

where μ_t represents the turbulent eddy viscosity and Pr_t the turbulent Prandtl number. The molecular dynamic viscosity is evaluated using the Sutherland's law of viscosity.

3.2 Turbulence Model

A turbulence model for the three-dimensional configuration of Fig. 2.2 is complicated and is still under development. As $z \to \infty$ the fin surface influences the turbulence; on the otherhand as $z \to 0$ the turbulence is dominated by the flat plate surface. In the junction between the fin and flat plate, the effect of turbulence is truly three-dimensional. The two-layer turbulent eddy viscosity model of Baldwin and Lomax [35] is extended to generalized coordinates to determine the turbulent transport coefficients. This model is particularly advantageous for certain shock-induced separated flows that contain a multiple region in which the length scales are not clearly defined. However, the present work does not account for the amplification of turbulent intensity after a sudden compression of the flow through the bow shock wave. The implementation of more realistic turbulence models for the present work awaits further study.

In each (J-K) plane, the computational domain is like a corner formed by two perpendicular walls as sketched in Fig. 3.2. For the sake of convenience coordinates (y,z) are used to define each (J-K) plane. The two-layer algebraic turbulence eddy viscosity model is applied in each region in the following manner.

Inner Region

For the inner region, the eddy viscosity model is expressed as

$$\varepsilon_{inner} = \rho (k\, \ell\, D)^2 |\omega| \qquad (3.9)$$

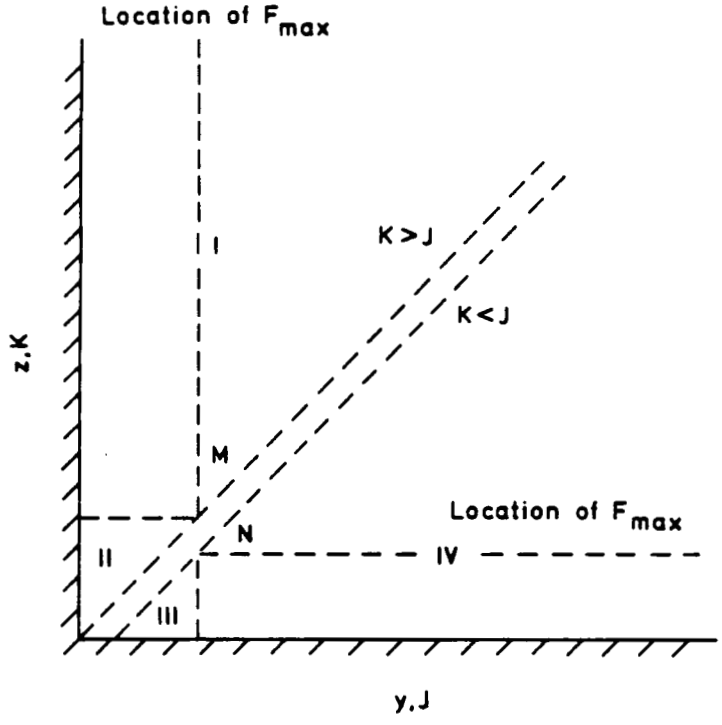

Fig. 3.2 Definition of four regions in (J-K) plane

where $k = 0.4$ is Von Karman's constant, ℓ is Buleev's length scale [41-43], D is the Van Driest damping factor and ω is the absolute value of the vorticity $(\omega = |\vec{\nabla} \times \bar{v}|)$, i.e.,

$$|\omega| = \sqrt{\left(\frac{\partial u}{\partial y} - \frac{\partial v}{\partial x}\right)^2 + \left(\frac{\partial v}{\partial z} - \frac{\partial w}{\partial y}\right)^2 + \left(\frac{\partial w}{\partial x} - \frac{\partial u}{\partial z}\right)^2} \qquad (3.10)$$

The general definition of the Buleev length scale is

$$\ell(x,y,z) = \left\{ \frac{1}{2} \int_0^{2\pi} \frac{d\phi}{s} \right\}^{-1} \qquad (3.11)$$

where s defines the distance from the field point (x,y,z) to a point on the boundary, and ϕ is the pheripheral angle as shown in Fig. 3.3. For a two-dimensional external corner flow, the Buleev length scale ℓ is the distance normal to the surface. For an open corner formed by two orthogonal planes, the Buleev length scale is given by

$$\ell = \frac{2yz}{y + z + (y^2 + z^2)^{1/2}} \qquad (3.12)$$

This formula is designed to account for the size of turbulence eddies or the turbulence mixing length near the corner under the influence of both walls.

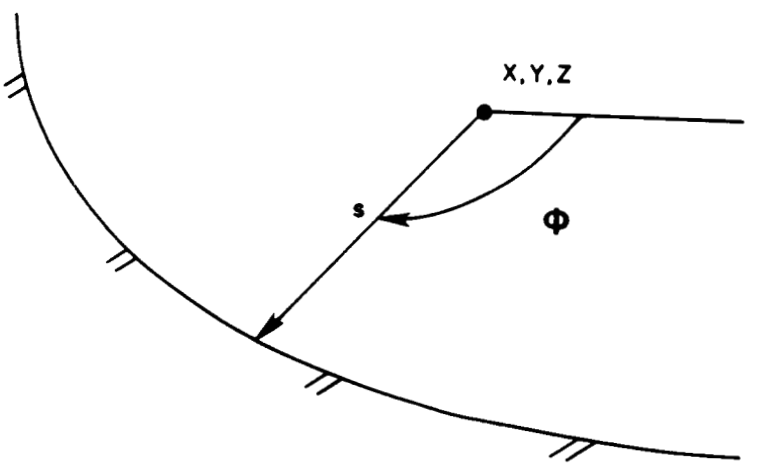

Fig. 3.3 Definition of Buleev length scale

Outer Region

In the outer region the outer eddy viscosity is given by

$$\varepsilon_{outer} = \rho K C_{cp} F_{wake} F_{kleb} \tag{3.13}$$

where K is the Clauser constant, C_{cp} is an additional constant. The outer wake function, F_{wake}, is defined by

$$F_{wake} = \text{the smaller of} \begin{cases} \ell_{max} F_{max.} \\ C_{wk} \ell_{max} u_e^2 / F_{max.} \end{cases} \tag{3.14a}$$

The quantity F_{max} is the maximum value of $F(y)$ that occurs in a profile and ℓ_{max} is the maximum value of ℓ where the maximum value of F_{outer} occurs. The relation for F_{outer} is

$$F_{outer} = \ell \omega D \tag{3.14b}$$

The wake function is a product of a length scale ℓ_{max} and the velocity scale F_{max} representative of the energy-containing eddies in the outer portion of the boundary layer. In effect, the distribution of vorticity is used to determine length scales so that the need to find the boundary layer edge is eliminated. The Klebanoff intermittency factor is given by:

$$F_{kleb}(\ell) = \left\{ 1 + 5.5 \left(\frac{C_{kleb} \ell}{\ell_{max}} \right)^6 \right\}^{-1} \tag{3.15}$$

where C_{kleb} is a constant. The quantity U_e is the difference between maximum and minimum total velocity in the profile.

$$U_e = \left(\sqrt{u^2 + v^2 + w^2}\right)_{max} - \left(\sqrt{u^2 + v^2 + w^2}\right)_{min} \qquad (3.16)$$

The second term in U_e is taken to be zero (except in wakes). The numerical value of the constants appearing in the foregoing relation are given as follows:

$$K = 0.0168, \quad C_{cp} = 1.6, \quad C_{kleb} = 0.3 \ .$$

The inner and outer eddy viscosity laws are combined to form the composite turbulence eddy viscosity model in the following manner. First, profiles of ε_{inner} and ε_{outer} are determined on each coordinate line orthogonal to the boundary. The first point nearest to the boundary where ε_{inner} exceeds ε_{outer} is denoted the "cross-over point." The turbulent viscosity ε is equal to ε_{inner} for all the points in the region between the boundary and the crossover point, and is equal to ε_{outer} for all the points above and including the crossover point.

In the vicinity of the corner, the (J-K) plane is divided into four regions I, II, III and IV as shown in Fig. 3.2. In regions I and II, D is evaluated at $z = 0$. The search for F_{max} and the corresponding ℓ_{max} proceeds from the wall, either from $y = 0$ for region IV, or from $z=0$ for region I. The values of F_{max} in region II and III are treated as constants equal to the value of F_{max} at M and N, respectively.

3.3 Thin Layer Approximation

Prandtl's classical boundary layer equations are obtained from the full Navier-Stokes equations by performing an order of magnitude analysis of the terms and neglecting terms of the order of the inverse power of the Reynolds number. This procedure leads to (1) neglecting the streamwise diffusion compared to normal diffusion; (2) the replacement of a normal momentum equation with the assumption of zero pressure gradient across the boundary layer thickness. The concept of thin-layer approximation to the full Navier-Stokes equation is similar to the boundary layer approximation with the only exception of retaining all three momentum equations. This procedure makes no assumption about the pressure variation across the boundary layer thickness. The thin-layer approximation is particularly advantageous for computing certain high Reynolds number flows and separated turbulent flows because it removes the troublesome singularities encountered at the separation points and permits straight forward computation of separated flows. As a result of the thin-layer approximation, the governing equations become simple and less complicated than those based on approximations that attempt to use streamwise gradients parallel to the body surface. The considerable simplification in numerical algorithm and physical concept motivate the straight forward implementation of the approximation into computer codes for high Reynolds number flows.

In the present research work this concept is extended in all three coordinate directions for a general coordinate system. All the viscous terms containing the cross derivatives $\partial^2/\partial x^i \partial x^j$ when $i \neq j$ are neglected while retaining the normal derivatives $\partial^2/\partial x^i \partial x^j$ when

$i = j$ in each direction. For example, along each coordinate direction the λ div $\underline{u}$ in Eq. (3.7b) will be expressed as

$$\frac{\partial}{\partial x^2}\left[\ldots \lambda \frac{\partial u^{n'}}{\partial x^{n'}} (g)^{1/2} g^{2}(i') + \text{---}\right] = \frac{\partial}{\partial x^2}\left[\lambda (g)^{1/2} g^{2}(i')\right.$$

neglected retained neglected

$$\times \left(\left[\frac{\partial u^{1'}}{\partial x^{1}} \cdot \frac{\partial x^{1}}{\partial x^{1'}} \right] + \frac{\partial u^{1'}}{\partial x^{2}} \cdot \frac{\partial x^{2}}{\partial x^{1'}} + \left[\frac{\partial u^{1'}}{\partial x^{3}} \cdot \frac{\partial x^{3}}{\partial x^{1'}} \right] \right.$$

$$+ \left[\frac{\partial u^{2'}}{\partial x^{1}} \cdot \frac{\partial x^{1}}{\partial x^{2'}} \right] + \frac{\partial u^{2'}}{\partial x^{2}} \cdot \frac{\partial x^{2}}{\partial x^{2'}} + \left[\frac{\partial u^{2'}}{\partial x^{3}} \cdot \frac{\partial x^{3}}{\partial x^{2'}} \right]$$

$$\left. + \left[\frac{\partial u^{3'}}{\partial x^{1}} \cdot \frac{\partial x^{1}}{\partial x^{3'}} \right] + \frac{\partial u^{3'}}{\partial x^{2}} \cdot \frac{\partial x^{2}}{\partial x^{3'}} + \left[\frac{\partial u^{3'}}{\partial x^{3}} \cdot \frac{\partial x^{3}}{\partial x^{3'}} \right] \right) + - - - \Bigg]$$

$$= \frac{\partial}{\partial x^2}\left[\ldots + \lambda (g)^{1/2} g^{2}(i') \times \left(\frac{\partial u^{1'}}{\partial x^{2}} \cdot \frac{\partial x^{2}}{\partial x^{1'}} + \frac{\partial u^{2'}}{\partial x^{2}} \cdot \frac{\partial x^{2}}{\partial x^{2'}} + \frac{\partial u^{3'}}{\partial x^{2}} \cdot \frac{\partial x^{2}}{\partial x^{3'}} \right) + \text{---}\right]$$

The above expression can be expressed in tensor form for each X^{ℓ}-direction as follows:

$$= \frac{\partial}{\partial x^{\ell}}\left[\text{---} \lambda \frac{\partial u^{n'}}{\partial x^{\ell}} \frac{\partial x^{\ell}}{\partial x^{n'}} (g)^{1/2} g^{\ell}_{(i')} + \text{-- -}\right] \qquad (3.17)$$

It should be noted, that not all the retained terms are larger than the neglected terms. Retention of all the second order normal derivative terms make the approximation convenient and consistent such that all dominant terms are retained for a general coordinate system except at the juncture between two walls. Near the juncture between

two walls the neglected cross derivatives can be of the same order of magnitude as the normal derivatives. But the flow at the juncture carries with it a low momentum fluid and hence neglecting the cross derivatives will not alter significantly the basic physics of the flow field. When not needed (because of the absence of a thin shear layer), the viscous terms can be completely neglected in any particular direction, and the present algorithm will reduce back to a thin-layer approximation for the presence of viscous shear layers in two or only one direction.

3.4 Mesh System

For simple configurations like swept and sharp fins on a flat plate, an algebraic grid generation technique is used to generate the mesh. This technique offers an easy control of the grid spacing and distribution. A modified elliptic grid generation technique [44] with direct control over the grid spacing is used to generate the mesh at a filleted fin/flat plate junction. The equation of the super ellipse $(\frac{X}{a})^n + (\frac{Y}{b})^n = 1$, is used to generate the grid for circular and continuous fillets in the plane of symmetry. The three-dimensional grid for a sharp fin (Fig. 3.4) is obtained by simply stacking horizontal grid in the direction normal to the flat plate surface. The three-dimensional grid structure for a swept and filleted fin (Fig. 3.5 and 3.6) is obtained by simply rotating the grid in the plane of symmetry about the center of the fin leading edge. The grid is clustered near the fin and plate surfaces using an exponential grid stretching formula to provide adequate resolution of the viscous

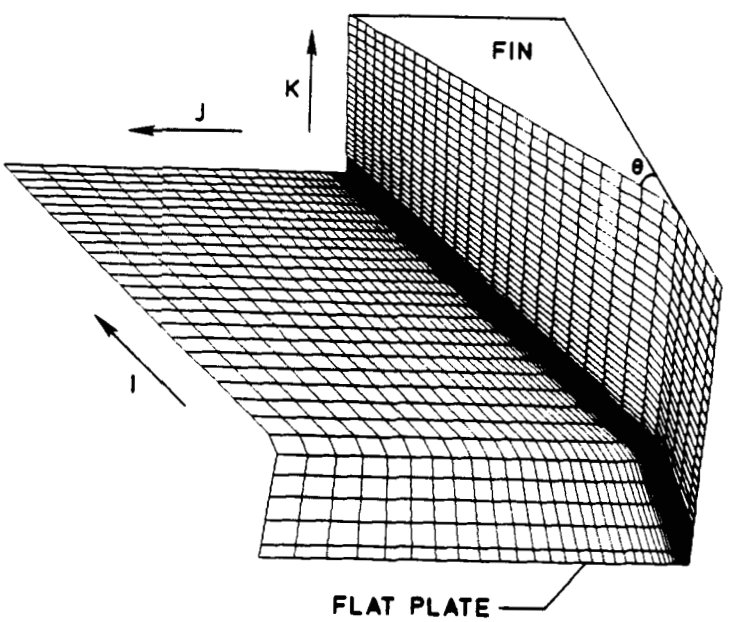

Fig. 3.4 Mesh distribution on sharp fin and flat plate

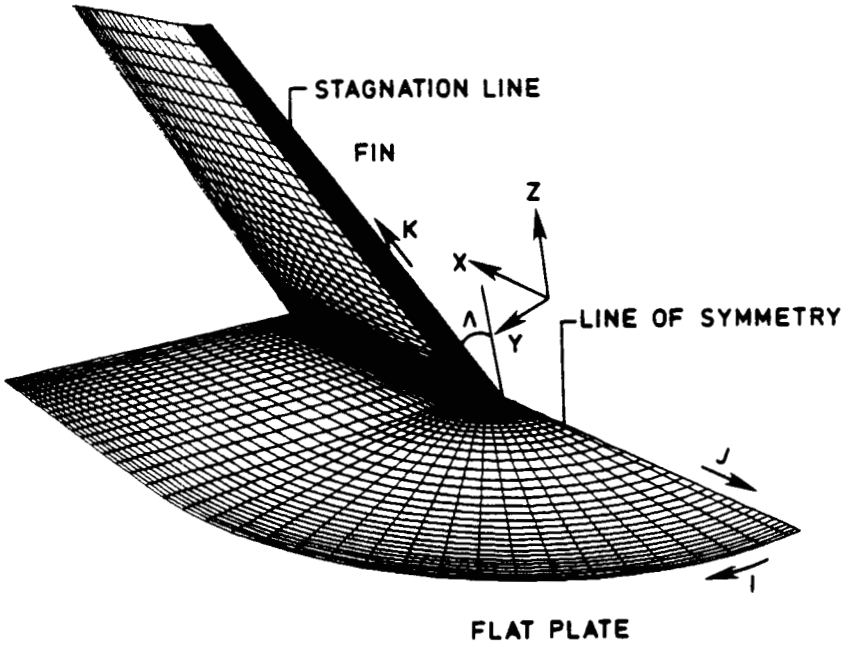

Fig. 3.5 Mesh distribution on swept fin and flat plate

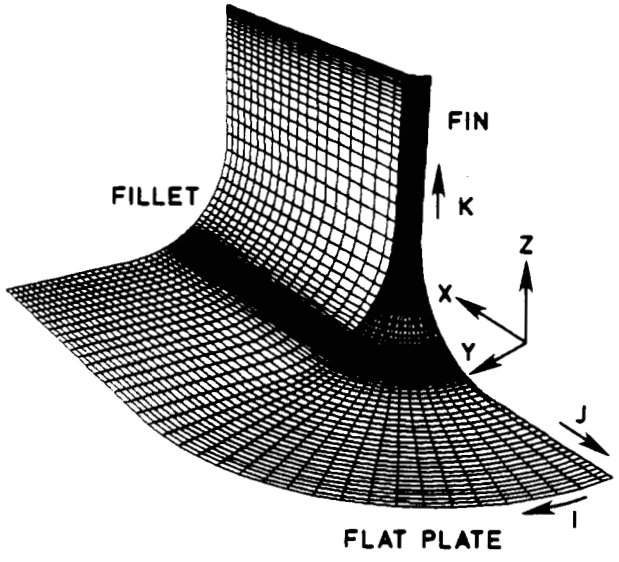

Fig. 3.6 Mesh distribution on filleted fin and flat plate

effects. Since the flow is assumed to be steady and symmetrical only one-half of the flow is computed.

3.5 Boundary Conditions

The physical boundary conditions to be imposed are problem dependent. At present, the 3D Navier-Stokes code has been applied to blunt fin/flat plate geometries. In this case, a supersonic laminar boundary layer develops on the flat plate. The deflection of the fin leading edge generates a bow shock wave which interacts with the boundary layer on the flat plate.

The boundary conditions applied may be categorized as follows:

3.5.1 Inflow Boundary

The incoming flow is supersonic (except in the subsonic portion of the boundary layer) and the inflow boundary is essentially perpendicular to the oncoming flow. Consequently all flow characteristics point from outside towards the computational domain and the appropriate boundary condition is to specify u, v, w, ρ and e_i. For the 3-D blunt fin, the upstream boundary layer profile is obtained from a two-dimensional compressible boundary layer code [45].

3.5.2 Outflow Boundary

The outgoing flow is assumed to be supersonic (except in the subsonic portion of the boundary layer), and the outflow boundary is essentially perpendicular to the outgoing flow. In this case all the flow characteristics point from inside to outside of the computational domain, and thus the outflow variables must be determined from the

interior flow solutions by zeroth order extrapolation. The fin is assumed to be infinite in length and height so that zero-gradient boundary conditions are appropriate at the outer boundaries in the corresponding directions. The outer boundary of $J = J_{max}$ is situated far enough to avoid any influence on the interaction region. Theoretically one can prescribe a boundary layer profile on the isolated flat plate at each x-location along the outer boundary as shown in Fig. 3.7. These profiles are obtained from solving the compressible boundary layer equations for flow over a flat plate.

3.5.3 Solid Boundary

At a solid wall boundary the following boundary conditions are enforced

$$\begin{aligned} \bar{V}\cdot\underline{n} &= 0 \\ \frac{\partial p}{\partial n} &= 0 \\ T = T_w \text{ or } k\frac{\partial T}{\partial n} &= q_w \end{aligned} \qquad (3.18)$$

where $\bar{v} = (u, v, w)$ is the cartesian velocity vector, p is the static pressure, T_w is the specified wall temperature, q_w is the specified wall heat flux and k is the coefficient of thermal conductivity. The boundary condition for the static pressure is an approximation to the exact boundary condition derivable from the normal component of the momentum equations, and has been applied for a variety of flows involving shock wave boundary layer interaction.

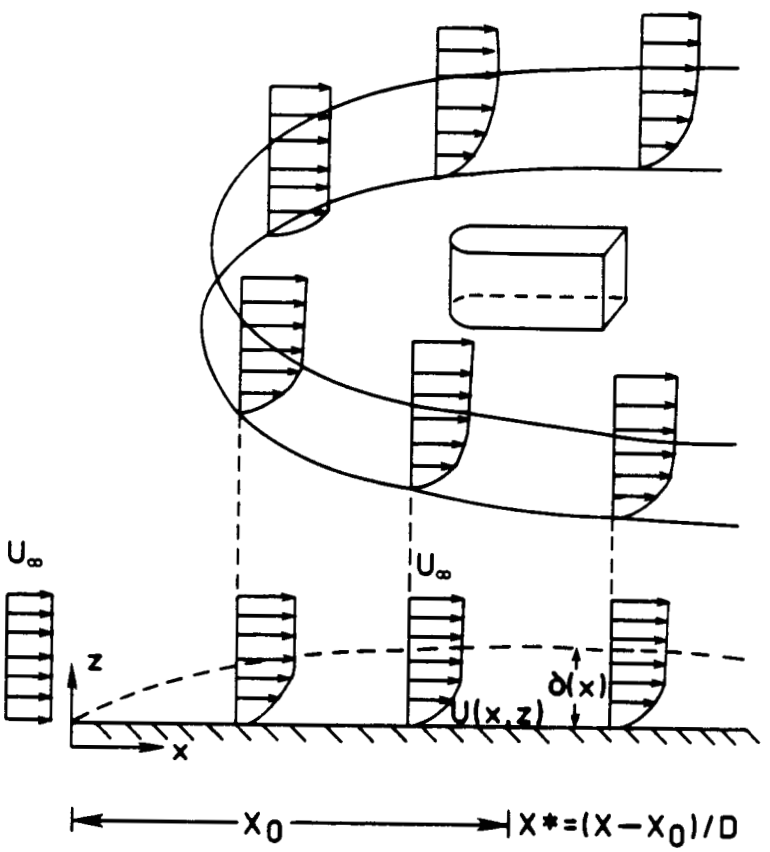

Fig. 3.7 Boundary layer profiles on the flat plate at $J=J_{max}$

3.5.4 Symmetry Boundary

The fin is at zero angle of attack, and the following boundary conditions apply on the plane of symmetry.

$$\bar{V}.\underline{n} = 0$$

$$\frac{\partial(\rho \bar{V} x \underline{n})}{\partial n} = 0 \qquad (3.19)$$

$$\frac{\partial p}{\partial n} = 0$$

$$\frac{\partial T}{\partial n} = 0$$

3.6 Initial Conditions and Blunt Body Starting Conditions

The simplest way to start a computational solution is by assuming that all initial conditions are the same as the incoming flow solutions. This may result in over compression near the stagnation region followed by an over expansion around the shoulder. This may cause the numerical scheme to become unstable, thereby resulting in negative density. To avoid this, Pulliam and Stegar [46] used a small time step during start-up by gradually enforcing the no slip wall boundary condition. Rizk, Chaussee, and McRae [47] treated the bow shock as a discontinuity and started with an assumed pressure distribution, in addition to the soft start technique. In the present research work, a simple formula is employed to avoid over expansion around the shoulder [40]. As depicted in Fig. 3.8 near the nose region, the normal velocity component is set to zero on the surface of

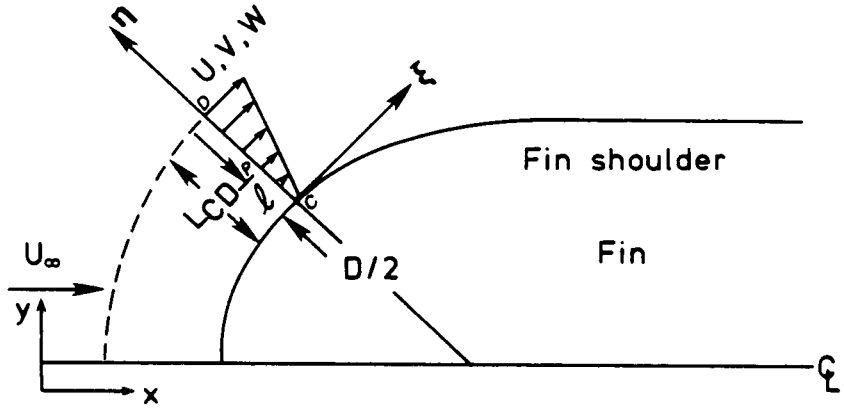

Fig. 3.8 Region near the nose for setting blunt body starting conditions

the body at C, and then increased linearly to the incoming flow velocity at a predetermined location, say D. The formula for velocity at a point between C and D is

$$\underline{u}_P = \underline{u}_D - (1 - \ell/L_{CD}) \left[(\underline{u} \cdot \underline{g}^n)/g^{nn} \right]_C \qquad (3.20)$$

where L_{CD} is the fixed length between two points C and D and ℓ is the variable length from the surface. The density and energy are set equal to the incoming flow conditions. This simple device may be interpreted as a defect in normal momentum and hence kinetic energy in the small region near the blunt nose. This device alleviates the nonphysical flow field development and allows large time steps during the start up phase. Though different possible boundary conditions were discussed the exact boundary conditions used in the present study are the same as given in the previous numerical study of supersonic junction flow [40].

Chapter 4

METHOD OF SOLUTION

In this section, the finite volume formulation is developed for solving the compressible Navier-Stokes equations at high Reynolds number. The governing equations are integrated numerically using the MacCormack's [48] explicit-implicit scheme in time split fashion to reduce the three-dimensional equations to three sets of locally one-dimensional equations.

4.1 Finite Volume Formulation

A finite volume cell, indexed by (i,j,k), is defined by eight corner points connected with straight lines, as shown in Fig. 3.1. Each edge of the finite volume cell is identified by a coordinate location (x_i^1, x_j^2, x_k^3) interchangeable with (ξ_i, η_j, ζ_k), where

$$
\begin{aligned}
x_i^1 &= \xi_i = (i-1)\,\Delta\xi, \quad i = 1, IL \\
x_j^2 &= \eta_j = (j-1)\,\Delta\eta, \quad j = 1, JL \\
x_k^3 &= \zeta_k = (k-1)\,\Delta\zeta, \quad k = 1, KL.
\end{aligned}
\tag{4.1}
$$

and the grid spacing along the local coordinate direction is given by

$$\Delta x^1 = \Delta\xi = 1/(IL-1)$$

$$\Delta x^2 = \Delta\eta = 1/(JL-1) \qquad (4.2)$$

$$\Delta x^3 = \Delta\zeta = 1/(KL-1)$$

The enclosed surface of each finite volume cell consists of a family of three coordinate surfaces that delineates the hexahedronal mesh cell. The above formula yields a unit cube for the transformed computational domain. The choice of a cube of unit dimension in the computational domain is arbitrary, and the other investigators have chosen the lengths of each side to yield $\Delta x^1 = \Delta x^2 = \Delta x^3 = 1$ so that the volume of each computational cell is given by $dv = g^{1/2}\, \Delta x^1\, \Delta x^2\, \Delta x^3$. It should be understood in Eq. (3.5) that $g^{1/2}$ is the volume of the cell $dv\,(i,j,k)$, the term $g^{1/2}\underline{g}^{\ell}$ represents the contravariant surface normal for the surface x^{ℓ} = constant and $\underline{u} \cdot g^{\ell}$ is the corresponding contravariant velocity evaluated at the bounding surfaces. Therefore, in Eqs. (3.7) $(g)^{1/2}\underline{g}^{\ell}_{(i')}$ is the surface area for X^{ℓ} = constant projected on the cartesian coordinate of $x^{i'}$ = constant.

In the finite difference approach, $(g^{1/2})$ and $g^{1/2}\underline{g}^{\ell}$ are defined at each grid point location, and are typically evaluated by a two-point central difference in all three directions. This leads to an inconsistancy in the volume and surface normal calculations such that the geometry conservation law is not satisfied and hence the difference scheme cannot recapture the free stream. This inconsistency does not occur in the present approach.

Note that any open-surface element for a given boundary enclosing the surface has a unique, effective surface vector $\underline{S}$ that is independent of the shape of the surface. This is because, applying the

divergence theorem to a constant vector, the integral of the outward-oriented surface normal over a closed surface vanishes as given below

$$\int_S \Phi \, \underline{n} \, ds = \int_V \nabla \Phi \, d v = 0 \quad \text{for} \quad \phi = \text{constant} \tag{4.3}$$

For example, the surface vector $\underline{S}_{5876}$ in Fig. 3.1 is independent of the choice of which the partitioning surface diagonal is used to define cell volumes. Indeed whether all the four vertices lie in a plane or not, the effective surface vector is equal to one-half the cross-product of its diagonal segments, i.e.,

$$\underline{S}_{5876} = 0.5 \times (\underline{r}_{75} \times \underline{r}_{86}) \tag{4.4}$$

Given eight corner points of each finite volume cell, a simple way to calculate the volume is to divide each face into two planar triangles. The volume is then dependent on which diagonal is used on each face since the diagonals of four nonplanar points do not intersect. In order for neighboring cells to be contiguous, without overlaps, neighboring cells must have the same surface partitioning. In the present study a simple formula developed by Kordulla and Vinokur [49] is employed to calculate the volume of each cell as

$$\begin{aligned} 6 \text{ VOL} &= \underline{r}_{71} \cdot [(\underline{r}_{31} \times \underline{r}_{21}) + (\underline{r}_{21} \times \underline{r}_{81}) + (\underline{r}_{41} \times \underline{r}_{31}) \\ &\quad + (\underline{r}_{61} \times \underline{r}_{41}) + (\underline{r}_{51} \times \underline{r}_{61}) + (\underline{r}_{81} \times \underline{r}_{51})] \\ &= \underline{r}_{71} \cdot [(\underline{r}_{31} \times \underline{r}_{24}) + (\underline{r}_{81} \times \underline{r}_{52}) + (\underline{r}_{61} \times \underline{r}_{45}) \\ &= 2 \, \underline{r}_{71} \cdot (\underline{S}_{1432} + \underline{S}_{1285} + \underline{S}_{1465}) \end{aligned} \tag{4.5}$$

With the volume and surface evaluated in integral form, Eq. (3.5) can be discretized as

$$dv_{i,j,k} \frac{\Delta \underline{q}_{i,j,k}}{\Delta t} + \delta[(\underline{q}\,\underline{u} + \underline{b}) \cdot \underline{s}]_{i,j,k} = 0 \qquad (4.6)$$

where $\underline{q}_{i,j,k}$ is a vector of the dependent variable located at the center of the cell and $(\underline{q}\,\underline{u} + \underline{b})$. $\underline{S}$ is the corresponding flux evaluated at the surface of each finite volume cell. In the present study, the discretized finite volume formulation, Eq. (4.6) is used for computation. In later discussions, for the purpose of explanation, Eq. (3.5) will be used. However, details of terms which have to be evaluated are based on Eqs. (3.7a) -(3.7c) with corresponding interpretations of $(g)^{1/2}$ as the volume at the centroid and $(g)^{1/2}\underline{g}^{\ell}$ as the surface normal evaluated at the boundary of each finite volume cell.

It is interesting to see that the finite volume formulation does not require a global coordinate transformation. In fact, the only data needed concerning the mesh are the three cartesian coordinates of each of the eight vertices of every cell in the mesh system. Moreover, the surface and volume of each cell are well defined and consistently evaluated, in contrast to a finite difference approach where the transformation coefficient and the Jacobian are evaluated from surrounding points.

In finite volume formulation, only the cell volume $(g)^{1/2}$ and the surface normal $(g^{1/2})\underline{g}^{\ell}$ are needed for inviscid flow computations. To evaluate the viscous terms, the distance between two

adjacent mesh cells is needed. In the present approach, instead of calculating this distance from the centroid, the vector between two adjacent cells (i,j,k) and (i+1,j,k) (see Fig. 4.1) is set in the same direction as the surface normal to the surface S_b, and is evaluated by

$$\underline{d}_{i,j,k} \cdot \underline{S}_b = |\underline{d}_{i,j,k}| \; |\underline{S}_b| = 0.5 \left(g^{1/2}_{i+1,j,k} + g^{1/2}_{i,j,k}\right) \qquad (4.7)$$

When shape variations are large, a more appropriate formula should be used for evaluating the metrics as given by the following formula.

$$\underline{d}_{i,j,k} \cdot (\underline{S}_a + 2\,\underline{S}_b + \underline{S}_c) = |\underline{d}_{i,j,k}| \; |\underline{S}_a + 2\,\underline{S}_b + \underline{S}_c| \qquad (4.8)$$

This implies that in a viscous dominated region, for instance near the wall, the grid lines would be required to be nearly orthogonal for an accurate evaluation of viscous terms.

4.2 Explicit MacCormack Algorithm

The MacCormack's explicit algorithm is implemented using a symmetric sequence of time split operators. The concept of splitting, generally known as the method of alternating directions, has been most popularly used to split the complex operators into a sequence of simpler ones. This concept is applied here to reduce the set of three-dimensional equations, Eq. (3.5), into three sets of one-dimensional equations.

Equation (3.5) can be split into three locally one-dimensional (LOD) operators as follows:

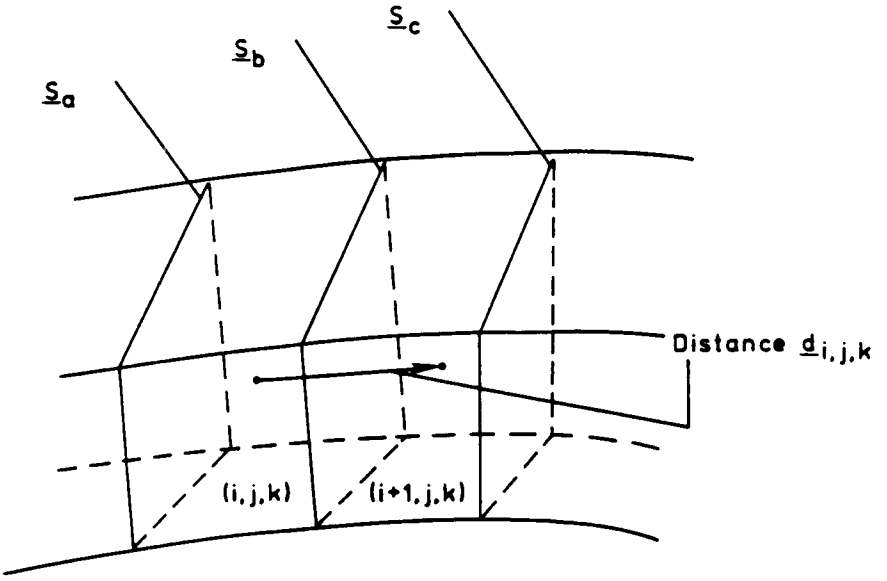

Fig 4.1 Distance $\underline{d}_{i,j,k}$ between two adjacent cells

$$\text{Lx:}\quad \underline{q}_{,t} + {}^{i}\hat{\underline{F}}_{,i} = 0 \text{ (no summation in i) } i = 1,\ 2,\ \text{or } 3 \qquad (4.9)$$

Here, each of the split operators contains the spatial derivatives of flux in only one direction. Since, this concept is limited to the LOD scheme, the summation convention will not be used in this section.

Let Δt be the time step, n the time level, and ${}^{i}\hat{\underline{F}}$ the flux across the cell surface x^i = constant. The LOD predictor-corrector scheme in a generalized coordinate system can be expressed as follows:

Predictor:

explicit
$$\Delta\hat{\underline{q}}^{n} = -\Delta t\left(\frac{\Delta_{+}\ {}^{i}\hat{\underline{F}}}{\Delta x^{i}}\right) \qquad (4.10a)$$

update
$$\overline{\Delta\hat{\underline{q}}^{n+1}} = \hat{\underline{q}}^{n} + \Delta\,\hat{\underline{q}}^{n}$$

Corrector:

explicit
$$\overline{\Delta\,\hat{\underline{q}}^{n+1}} = -\Delta t\left(\frac{\Delta_{-}\ {}^{i}\hat{\underline{F}}}{\Delta x^{i}}\right) \qquad (4.10b)$$

update
$$\hat{\underline{q}}^{n+1} = \frac{1}{2}\left(\hat{\underline{q}}^{n} + \Delta\hat{\underline{q}}^{n+1}\right)$$

Here, the overbars in the corrector sweeps indicate that the quantities are determined with updated predictor values. The Δ_{+} and Δ_{-}

indicate forward and backward two-point differences. Although the operators are all one-sided by themselves, the resulting algorithm is second order accurate in space and time.

Each of the Lx^i operators discussed above consists of a predictor-corrector set, and requires no block or scalar tridiagonal inversion. Because of the noncommutativity of Lx^i operators, the combined numerical scheme is accurate only to first order. To retain the second-order accuracy, a symmetric sequence of LOD operators, developed by Strang [50] is used. Specifically, the solution vector $\hat{\underline{q}}$ is updated in time according to the following relation:

$$\hat{\underline{q}}^{n+2} = L_\eta(\Delta t_\eta)\, L_\zeta(\Delta t_\zeta)\, L_\xi(2\Delta t_\xi)\, L_\zeta(\Delta t_\zeta)\, L_\eta(\Delta t_\eta)\, \hat{\underline{q}}^{n} \qquad (4.11)$$

By this procedure the solution is advanced two time steps from t to $t + 2\Delta t$.

1. Temporal Accuracy

In order to retain a second order accurate scheme in time for the operator sequence of Eq. (4.11), the total time applied to each operator must be the same, i.e.,

$$\Delta t_\xi = \Delta t_\eta = \Delta t_\zeta = \Delta t \qquad (4.12)$$

2. Numerical Stability

Because of the complexity of the full Navier-Stokes equation, it is not possible to obtain a closed-form stability expression for the MacCormack scheme applied to these equations. However, the linearized set of equations, can be subjected to von Neumann type stability

analysis. In order to maintain numerical stability, the time for each operator must satisfy the following stability condition:

$$\Delta t_{\xi} \leq \Delta t_{\xi_{CFL}}$$

$$\Delta t_{\eta} \leq \Delta t_{\eta_{CFL}} \tag{4.13}$$

$$\Delta t_{\zeta} \leq \Delta t_{\zeta_{CFL}}$$

where the maximum allowable time steps $\Delta t_{\xi_{CFL}}$, $\Delta t_{\eta_{CFL}}$ and $\Delta t_{\zeta_{CFL}}$, are given in Appendix A.

The explicit MacCormack's algorithm of has several advantages. First, the method is second-order accurate in time and space. Second, it is relatively easy to code the explicit algorithm. Third, the explicit algorithm is easily vectorizable. Fourth, the algorithm is robust, in the sense that its overall stability is relatively insensitive to the initial conditions employed. In practical terms, this implies that the initial condition need not be close to the final solution. In all the computations to date on three-dimensional problems, the flow initial conditions are obtained by simply propagating the prescribed boundary layer at the outer boundary of $J = J_{max}$ throughout the mesh.

Computations involving the compressible Navier-Stokes equations sometimes "blow up" because of large gradients, for example when the flow field contains strong shock waves. In many instances, it is not practical to refine the mesh in these regions, particularly if they are far removed from the region of interest. For such situations a fourth order damping term is added to the scheme to suppress the

numerical oscillations. This smoothing term has a very small magnitude except in regions of pressure oscillations where the truncation error is already degrading the computed solution, and should be nearly zero as steady state is approached.

4.3 Implicit MacCormack Algorithm

For computations involving full Navier-Stokes equations, grid lines have to be clustered in the direction normal to the wall. In such situations, the explicit CFL stability limit becomes very restrictive and a large number of iterations are required to reach a steady state solution. The stability analysis of the implicit schemes shows that there are no restrictions on the time of integration and that it is unconditionally stable.

Bi-diagonal Scheme and Locally One-Dimensional Time Splitting

The bi-diagonal implicit scheme in generalized coordinates at time level n is introduced into explicit predictor and corrector steps as follows:

Predictor:

explicit $$\Delta \hat{\underline{q}}^n = -\Delta t \left(\frac{\Delta_+ \, {}^i\hat{\underline{F}}}{\Delta x^i} \right)$$

implicit $$\left(I - \Delta t \, \frac{\Delta_+ |^i \, \hat{\underline{A}} \, |n.}{\Delta x^i} \right) \overline{\delta \hat{\underline{q}}^{n+1}} = \Delta \hat{\underline{q}}^n \qquad (4.14a)$$

update $$\overline{\hat{\underline{q}}^{n+1}} = \hat{\underline{q}}^n + \delta \hat{\underline{q}}^{n+1}$$

Corrector:

$$\text{explicit} \qquad \overline{\Delta \hat{\underline{q}}^{n+1}} = -\Delta t \left(\frac{\Delta_- {}^{i}\hat{\underline{F}}}{\Delta x^{i}} \right)$$

$$\text{implicit} \qquad \left(I + \Delta t \, \frac{\Delta_- | {}^{i}\hat{\underline{A}} |^{n+1}}{\Delta x^{i}} \right) \delta \hat{\underline{q}}^{n+1} = \overline{\Delta \hat{q}^{n+1}} \qquad (4.14b)$$

Update: $$\hat{\underline{q}}^{n+1} = \frac{1}{2} \left(\hat{\underline{q}}^{n} + \overline{\hat{\underline{q}}^{n+1}} + \delta \hat{\underline{q}}^{n+1} \right)$$

The matrices $| {}^{i}\hat{\underline{A}} |$ are matrices with positive eigenvalues.

$$| {}^{i}\hat{A} | = \hat{M}_i^{-1} \, (| {}^{i}\underline{D} |) \, \hat{M}_i$$

where

$$| {}^{i}\underline{D} | = \begin{bmatrix} {}^{i}\lambda_1 & & & & 0 \\ & {}^{i}\lambda_2 & & & \\ & & {}^{i}\lambda_3 & & \\ & & & {}^{i}\lambda_4 & \\ 0 & & & & {}^{i}\lambda_5 \end{bmatrix}$$

The $\hat{M}_i$ are the similarity transformation matrices which diagonalize the Eulerian Jacobian ${}^{i}\hat{\underline{A}}$ in Eq. (3.6) by setting $\mu = \lambda = 0$. The diagonal terms of the matrix $| {}^{i}\underline{D} |$ contains three distinct representative eigenvalues defined by

$$ {}^{i}\lambda_{u} = \max\left(\left| \underline{u} \cdot \underline{g}^{i} \right| + \frac{2\,\mu\gamma M_{\infty}}{RePr} \frac{g^{ii}}{\rho \Delta x^{i}} - \frac{\Delta x^{i}}{\Delta t}, 0 \right) $$

$$ {}^{i}\lambda_{u+a} = \max\left[\left| \underline{u} \cdot \underline{g}^{i} \pm a \left(g^{ii}\right)^{1/2} \right| + \frac{2\mu\gamma M_{\infty}}{RePr} \frac{g^{ii}}{\rho \Delta x^{i}} - \frac{\Delta x^{i}}{\Delta t}, \; 0 \right] $$

where $g^{ii} = \underline{g}^{i} \cdot \underline{g}^{i}$. The eigenvalues of the diagonal matrix $|{}^{i}\underline{D}|$ for $i = 1, 2, 3$ can be expressed as follows:

for i=1 $ {}^{1}\lambda_{1} = {}^{1}\lambda_{3} = {}^{1}\lambda_{4} = {}^{1}\lambda_{u} $

$$ {}^{1}\lambda_{2} = {}^{1}\lambda_{u+a}, \text{ and } {}^{1}\lambda_{5} = {}^{1}\lambda_{u-a} $$

for i=2 $ {}^{2}\lambda_{1} = {}^{2}\lambda_{2} = {}^{2}\lambda_{4} $

$$ {}^{2}\lambda_{3} = {}^{2}\lambda_{u+a} \text{ and } {}^{2}\lambda_{5} = {}^{2}\lambda_{u-a} $$

for i=3 $ {}^{3}\lambda_{1} = {}^{3}\lambda_{2} = {}^{3}\lambda_{3} = {}^{3}\lambda_{u} $

$$ {}^{3}\lambda_{4} = {}^{3}\lambda_{u+a} \text{ and } {}^{3}\lambda_{5} = {}^{3}\lambda_{u-a} $$

Each transformation matrix of $\hat{M}_{i}$ for $i = (1, 2, 3)$ is split into three matrices which can be expressed as follows:

$$ \hat{M}_{i} = M_{ic} M_{it} M $$

where

$$M = \begin{bmatrix} 1 & 0 & 0 & 0 & 0 \\ -u\rho^{-1} & \rho^{-1} & 0 & 0 & 0 \\ -v\rho^{-1} & 0 & \rho^{-1} & 0 & 0 \\ -w\rho^{-1} & 0 & 0 & \rho^{-1} & 0 \\ \alpha\beta & -\beta u & -\beta v & -\beta w & \beta \end{bmatrix}$$

$$\alpha = 0.5(u^2+v^2+w^2) \text{ and } \beta = (\gamma-1)$$

for i = 1

$$M_{1C} = \begin{bmatrix} 1 & 0 & 0 & 0 & -a^{-2} \\ 0 & \rho a & 0 & 0 & 1 \\ 0 & 0 & 1 & 0 & 0 \\ 0 & 0 & 0 & 1 & 0 \\ 0 & -\rho a & 0 & 0 & 1 \end{bmatrix}$$

$$M_{1T} = \begin{bmatrix} 1 & 0 & 0 & 0 & 0 \\ 0 & e^1(i') & e^1(2') & e^1(3') & 0 \\ 0 & -e^1(2') & e^1(1') & 0 & 0 \\ 0 & -e^1(3') & 0 & e^1(1') & 0 \\ 0 & 0 & 0 & 0 & 1 \end{bmatrix}$$

for i = 2

$$M_{2C} = \begin{bmatrix} 1 & 0 & 0 & 0 & 0 \\ 0 & 1 & 0 & 0 & 0 \\ 0 & 0 & \rho a & 0 & 1 \\ 0 & 0 & 0 & 1 & 0 \\ 0 & 0 & -\rho a & 0 & 1 \end{bmatrix}$$

$$M_{2T} = \begin{bmatrix} 1 & 0 & 0 & 0 & 0 \\ 0 & e^2(2') & -e^2(1') & 0 & 0 \\ 0 & e^2(1') & e^2(2') & e^2(3') & 0 \\ 0 & 0 & -e^2(3') & e^2(2') & 0 \\ 0 & 0 & 0 & 0 & 1 \end{bmatrix}$$

for i = 3

$$M_{3C} = \begin{bmatrix} 1 & 0 & 0 & 0 & -a^2 \\ 0 & 1 & 0 & 0 & 0 \\ 0 & 0 & 1 & 0 & 0 \\ 0 & 0 & 0 & \rho a & 1 \\ 0 & 0 & 0 & -\rho a & 1 \end{bmatrix}$$

$$M_{3T} = \begin{bmatrix} 1 & 0 & 0 & 0 & 0 \\ 0 & e^3{}_{(3')} & 0 & -e^3{}_{(1')} & 0 \\ 0 & 0 & e^3{}_{(3')} & -e^3{}_{(2')} & 0 \\ 0 & e^3{}_{(1')} & e^3{}_{(2')} & e^3{}_{(3')} & 0 \\ 0 & 0 & 0 & 0 & 1 \end{bmatrix}$$

Here, $e^{\ell}_{(i')} = g^{\ell}{}_{(i')} / (g^{\ell\ell})^{1/2}$ is the component of the normal contravariant vector in the i' direction. The M matrices transform $\delta\hat{\underline{q}}$ from conservative to nonconservative variables; the matrices M_{it} account for the orientation of the cell faces, x^i = constant, and matrices M_{iC} then transform from nonconservative to characteristic forms. It is interesting to see that the matrices M and M_{iC} are the same in the Cartesian coordinate system and non-orthogonal curvilinear coordinate system; the matrices M_{iT} account for the generalized coordinate transformation. The characteristic variables for i = 1, 2, 3 are expressed as follows:

for i = 1

$$\delta\hat{\theta}_{1C} = \begin{bmatrix} \delta\rho - (1/a^2)\delta p \\ \delta\rho + \rho a \delta \underline{u} \cdot \underline{g}^1/(g^{11})^{1/2} \\ e^1(1')\delta v - e^1(2')\delta u \\ e^1(1')\delta w - e^1(3')\delta u \\ \delta\rho - \rho a \delta u \cdot g^1/g^{11})^{1/2} \end{bmatrix}$$

for i = 2

$$\delta\hat{\theta}_{2C} = \begin{bmatrix} \delta\rho - (1/a^2)\ \delta p \\ e^2{}_{(2')}\ \delta u - e^2{}_{(1')}\ \delta v \\ \delta\rho + \rho a \delta \underline{u} \cdot g^2/(g^{22})^{1/2} \\ e^2(2')\ \delta w - e^2(3')\ \delta v \\ \delta\rho - \rho a \delta \underline{u} \cdot \underline{g}^2/(g^{22})^{1/2} \end{bmatrix}$$

for i = 3

$$\delta\hat{\theta}_{3C} = \begin{bmatrix} \delta\rho - (1/a^2)\ \delta p \\ e^3(3')\ \delta u - e^3(1')\ \delta w \\ e^3(3')\ \delta v - e^3(2')\ \delta w \\ \delta p + \rho a \delta \underline{u} \cdot g^3/(g^{33})^{1/2} \\ \delta p - \rho a \delta \underline{u} \cdot g^3/(g^{33})^{1/2} \end{bmatrix}$$

Now it is clear that $\hat{M}_i$ transforms the inviscid portion of $^{j}\hat{F}_{,j}$ into characteristic form $\delta\hat{\theta}_{jC}$ only when $i = j$. This implies that, in contrast to the unsplit formulation, LOD time splitting makes

variables consistent with the characteristic variables by means of the similarity transformation employed in the implicit steps [Eqs. (4.14a) and (4.14b)].

Two points should be noted here. First, it is an insurmountable task to develop the similarity transformation for each entire viscous Jacobian $\hat{\underline{A}}^{i}$. To keep the right hand side of Eqs. (4.14a) and (4.14b) as simple and straightforward as possible, we follow here the suggestion given by MacCormack to consider only the Eulerian Jacobian of $\hat{\underline{A}}^{i}$ with the addition of a small number of dominant viscous terms to the Eulerian eigenvalues. Second, the implicit procedure is skipped whenever the explicit stability conditions are satisfied locally, and the algorithm requires virtually no more computation time than an explicit method.

Each split operator described above consists of an explicit-implicit predictor-corrector set, is second-order accurate in time and space, is unconditionally stable, and requires no block or scalar tridiagonal inversion. Because of the noncommutativity of split operators, the simple combined numerical scheme, $Lx^1\ Lx^2\ Lx^3$ is only first order accurate. To maintain, the second order accuracy of the method, a symmetric sequence of the LOD operators, developed by Strang [50] are employed. Here, the solution is advanced from time t to $t + 2\Delta t$ as follows

$$\hat{\underline{q}}^{n+2} = L_n(\Delta t)\ L_\zeta(\Delta t)\ L_\xi(2\Delta t)\ L_\zeta(\Delta t)\ L_n(\Delta t)\ \hat{\underline{q}}^{n} \qquad (4.15)$$

Each locally one-dimensional split operator is applied line by line in each sweep direction and, hence, only needs one level plus three single arrays of dependent variables. Without this splitting, the MacCormack scheme requires, in general, two time levels of variable plus a level of right-hand-side residuals for a total of three levels of variables stored.

4.4 Operation of Numerical Code

4.4.1 General Procedure

The computation of three-dimensional shock wave boundary layer interactions using the numerical code is accomplished in three phases as follows:

1. Mesh Generation and Initial Flow Condition

   Depending on the investigation of the flow past a specific configuration, the user generates the grid using a separate grid generation code. Once the coordinates of the mesh points are known, the volume and surface normal for each finite volume cell can be easily computed. The information concerning the storage architecture for the physical coordinates is provided with the numerical code. The initial condition, including the upstream (inflow) profiles, and the profiles at $J = J_{max}$ on the flat plate are provided by the user. Depending upon the particular geometry under consideration the upstream profile may be a uniform flow, or a boundary layer flow generated by solving the two-dimensional compressible boundary layer equations. The information con-

cerning the storage for the flow field and surface normals is provided in the numerical code.

2. Computation of the Three-Dimensional Flow Field Using the Numerical Code

   The numerical code is used to integrate the governing equation in time until a steady state solution is obtained. The user of the code must ensure that reasonable criteria for the achievement of steady flow have been met.

3. Graphic Display of Flow Field

   The user must develop his own graphics code to post process the output generated by the three-dimensional Navier-Stokes code. In this regard, the user may interface his graphics code with the graphics library on the host computer.

4.4.2 Requirements on Grid

The body-oriented generalized coordinate system must provide adequate resolution to unravel the basic physical aspects of the flow field. A complete set of mesh criteria for judging the acceptability of the grid system does not exist at present, except for the process of mesh refinement which is generally not feasible for three-dimensional Navier-Stokes simulations. The determination of the acceptability of a given grid system, therefore, must be based on experience and previous numerical computations.

There are, however, a number of necessary criteria which may be identified as follows:

1. Resolution of Boundary Layers in the Direction Normal to the Boundary.

The flow field in the direction normal to the boundary is generally characterized by the steep flow gradients. This is based on previous experience that a minimum of fifteen (15) grid points be placed in the boundary layer depending on the amount of resolution needed to resolve steep flow gradients. For a turbulent flow, the y^+ of the first mesh point should be located less than three wall units from the boundary for accurate resolution of the viscous sublayer. The distance of the first mesh point from the wall in the laminar case should be less than or equal to $\frac{2}{3}\frac{D}{\sqrt{Re_D}}$.

2. Resolution of Boundary Layers in the Cross flow Direction.

In the numerical simulation of the three-dimensional flow field, a typical maximum grid spacing in the cross flow direction is provided. This is kept between 0.2δ to 0.8δ, where δ is the boundary layer thickness to accurately resolve the spatial features of the flow field. This criteria, however, has not been extensively tested and more stringent requirements may need to be imposed depending upon the flow configuration.

3. Resolution of the Boundary Layers in the Streamwise Direction

The streamwise grid spacing depends strongly on the character of the flow field. In the vicinity of interaction region, the streamwise grid spacing is determined by the size of the interaction region. For nominally, two-dimensional shock-boundary layer interaction the size is a function of pressure rise, Reynolds number, and may be a fraction of the

boundary layer thickness. For a three-dimensional shock-boundary layer interaction, the size of the interaction region is larger than a corresponding two-dimensional interaction with the same pressure rise.

4. Resolution of the Inviscid Flow

The criteria for grid spacing in the inviscid region depends upon the particular flow configuration, and must be determined on a case-by-case basis. For example, the existence of a bow shock upstream of the blunt leading edge at high Mach numbers may impose a stringent local constraint on the inviscid grid spacing.

Chapter 5

PHYSICAL CONDITIONS OF INVESTIGATION

For understanding the flow past a wing/body junction, three specific simplified geometries were selected. These include: (1) blunt swept fin/flat plate junction, (2) sharp fin/flat plate junction, and (3) filleted fin/flat plate junction. The special cases of blunt and sharp fins are used to obtain specific results for which extensive measurements on velocity and pressure distribution, skin friction, and surface yaw angles are readily available in the literature. In a typical three-dimensional flow past a fin/flat plate junction the various parameters controlling the interaction are D (diameter of the fin), Λ (fin sweep angle), δ (incoming boundary layer thickness), M_∞ (Mach number), and Re_ℓ (unit Reynolds number). The parameters controlling the filleted fin-induced interactions are R (fillet radius) and δ (incoming boundary layer thickness). Since three dimensional computations are expensive, only limited parametric studies were carried out for selected values of sweep angle, fillet radius, Mach number, Reynolds number, and Mesh resolution. The range of values in each set of parameters is carefully selected to portray its dramatic influence in controlling the intersection flow fields. The flow field simulation of the selected cases can be easily attempted on existing super computers without requiring excessive computational resources.

5.1 Laminar Flow Past a Swept Fin/Flat Plate Junction-- Validation with Experiment and Parametric Study

5.1.1 Validation with Experiment

For the specific problem of flow past a blunt fin/flat plate junction, comparative results were obtained corresponding to the following experimental conditions [16]:

$$M_\infty = 2.95,\ p_{0\,\infty} = 22261\ N/m^2,\ T_{0\,\infty} = 298\ K,$$

$$\delta = 0.225\ cm,\ D = 1.875\ cm,\ H = 7.5\ cm,\ \Lambda = 0^\circ$$

Figure 5.1 shows a simplified blunt fin/flat plate junction and various locations along which the computed results are compared with the experimental measurements. The experimental investigation includes data on pressure distribution along the fin stagnation line and selected spanwise locations. To supplement the measurements, oil flow visualization technique is also used to reveal the global structure of the flow on the fin and flat plate surface.

5.1.2 Parametric Study

The parametric studies were conducted to investigate the effect of fin sweep and incoming boundary layer thickness. The conditions for which specific results were obtained are as follows:

Effect of Fin Sweep

$$M_\infty = 2.95,\ p_{0\,\infty} = 22261\ N/m^2,\ T_{0\,\infty} = 298\ K$$

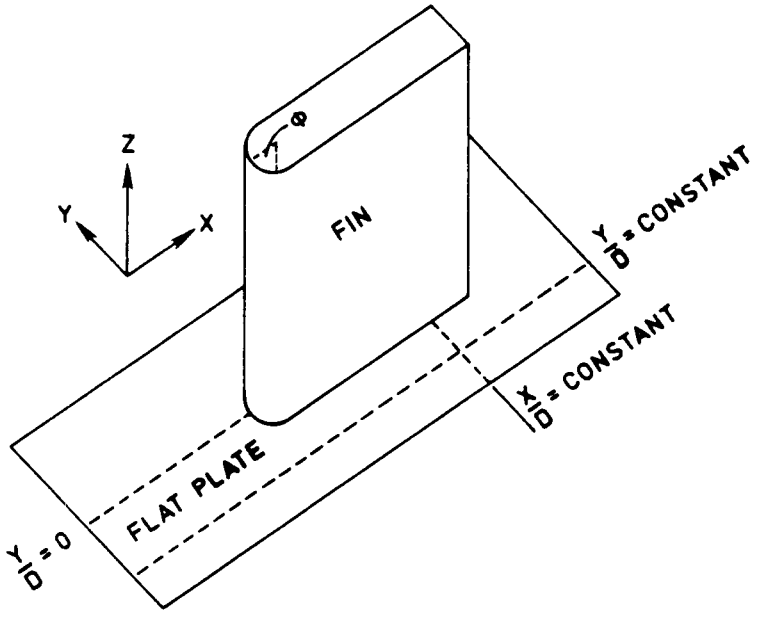

Fig 5.1 Geometry of blunt fin/flat plate junction showing typical surface locations of comparison with experiment

δ = 0.225 cm, D = 1.875 cm, H = 7.5 cm, Λ = 0° to 45°

Effect of Incoming Boundary Layer Thickness

M_∞ = 2.95, $p_{0\,\infty}$ = 2226 N/m^2, $T_{0\,\infty}$ = 298 K

δ = 0.675 cm, D = 1.875 cm, H = 7.5 cm, Λ = 0° and 45° only

5.2 Laminar Flow Past a Blunt Fin - Conditions for Additional Results and Parametric Studies

5.2.1 Conditions for Additional Results

The following specific conditions were selected to obtain additional results and for parametric studies:

M_∞ = 2.36, $p_{0\,\infty}$ = 24000 N/m^2, $T_{0\,\infty}$ = 294 K

δ = 0.186 cm, D = 0.635 cm, H = 5 cm

This specific case was selected to validate the code with the experimental measurements of velocity distribution in the separated region. The experimental measurements were obtained by oil flow visualization, Schlieren observations, and laser anemometry and the results are available in [52].

5.2.2 Parametric Studies

The parametric studies were conducted by using the conditions of Sec. 5.2.1 and changing the various parameters.

Effect of Grid Refinement

To investigate the effect of grid refinement, the conditions of Sec. 5.2.1 were used and results were obtained for the following three grids:

$$30 \times 50 \times 30, \quad 40 \times 100 \times 30, \quad 40 \times 100 \times 50$$

Effect of Mach Number

The freestream stagnation temperature was changed corresponding to each Mach number while keeping the other conditions constant as given in Sec. 5.2.1. The results were obtained for the following cases:

$$M_\infty = 1.2, \quad T_{0\infty} = 286 \text{ K}$$

$$M_\infty = 2.36, \quad T_{0\infty} = 294 \text{ K}$$

$$M_\infty = 3.5, \quad T_{0\infty} = 307 \text{ K}$$

Effect of Reynolds Number

The unit Reynolds number of the freestream is altered by changing the tunnel stagnation pressure while keeping the other freestream conditions constant as given under Sec. 5.2.1. The results were obtained for the following cases:

$$p_{0\infty} = 12{,}000 \text{ N/m}^2, \quad Re_\ell = 1.25 \times 10^6/\text{m}$$

$p_{0\infty}$ = 24,000 N/m^2, Re_ℓ = 2.5 x 10^6/m

$p_{0\infty}$ = 48,000 N/m^2, Re_ℓ = 5.0 x 10^6/m

5.3 Turbulent Flow Past a Sharp Fin/Plate Plate Junction

5.3.1 Flow Past a 16° Sharp Fin

For the case of a 16° sharp fin induced shock wave/boundary layer interaction, comparative results were obtained corresponding to the following experimental conditions [53]:

$$M_\infty = 4.0, \quad P_{0\infty} = 1180822 \text{ N/m}^2, \quad T_{0\infty} = 336 \text{ K}$$

$$\delta = 0.46 \text{ cm}, \; H = 3.7 \text{ cm}, \; \theta = 16°$$

The experimental study gathered data on wall pressure, surface yaw angle, and skin friction distribution at a specified spanwise location throughout the interaction region. The experimental study employed oil flow visualization to understand the flow structure, Preston tube for measuring skin friction, and cobra probes for flow field yaw angles.

5.3.2 Flow Past a 20° Sharp Fin

The strong interaction generated by a 20° sharp fin on a flat plate is investigated corresponding to the following conditions [54]:

$$M_\infty = 2.93,\ P_{0\infty} = 688320\ N/m^2,\ T_{0\infty} = 260\ K$$

$$\delta = 1.27\ cm,\ H = 10\ cm,\ \theta = 20^\circ$$

Figure 5.2 shows the axial location of experimental surveys where the computed pressure distribution is compared with experiment as a function of the Z- coordinate normal to the flat plate. The experiments were carried out using high Reynolds number supersonic tunnel to measure the pressure and yaw angle as a function of the coordinate normal to the flat plate.

5.4 Turbulent Flow Past a Swept Fin/Flat Plate Junction

For the case of swept fin induced shock wave/turbulent boundary layer interaction, comparative results were obtained corresponding to the following experimental conditions [17]:

$$M_\infty = 3.71,\quad p_{0\infty} = 203055\ N/m^2,\quad T_{0\infty} = 339\ K$$
$$\delta = 5\ cm,\ D = 5\ cm,\ H = 35\ cm,\ \Lambda = 0^\circ \text{ to } 60^\circ$$

5.5 Turbulent Flow Past a Filleted Fin

5.5.1 Flow Past an Unmodified Junction

For the case of low Reynolds number flow past a blunt fin/flat plate junction, results were obtained corresponding to the following experimental conditions [33]:

$$M_\infty = 2.5,\quad p_{0\infty} = 27000\ N/m^2,\quad T_{0\infty} = 312\ K$$

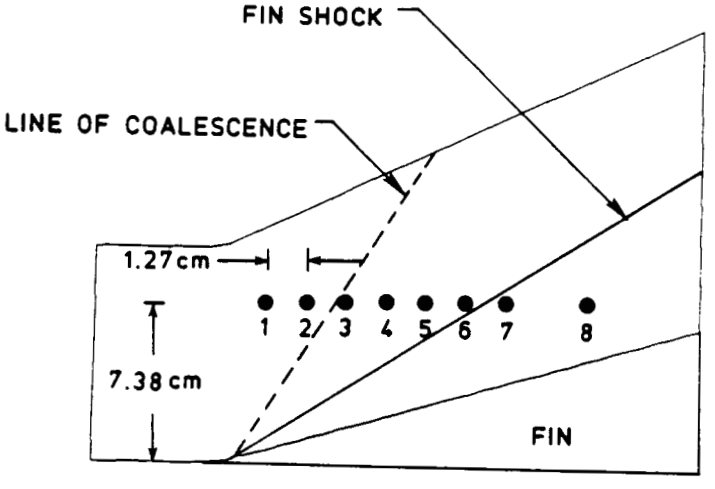

Fig 5.2 Location of experimental surveys for 20° sharp fin

δ = 5 cm, D = 2.5 cm, H = 20 cm

5.5.2 Flow Past a Modified Junction

For the modified junction, the effects of fillet radius and incoming boundary layer thickness were investigated.

Effect of Fillet Radius

Two circular fillets with a radius (R = 5 cm, 9 cm) and a continuous fillet were used to modify the junction. The incoming flow conditions were kept as in the blunt fin/flat plate junction case.

Effect of Incoming Boundary Layer Thickness

Keeping the fillet radius (R = 9 cm) constant, the incoming boundary layer thickness was decreased by an order of magnitude from 5 cm to 0.5 cm to investigate its effect in controlling the juncture vortex.

Chapter 6

RESULTS AND DISCUSSION

The entire results obtained for the physical conditions described in Chap. 5 are presented and discussed in this chapter. For the physical conditions where experimental results were available, the numerical results were obtained to validate the numerical scheme and the computer code developed in this study. Extensive results were obtained for other physical conditions to study the behavior of three-dimensional separation for various high speed juncture flows. The effect of different parameters in controlling the intersection flow field were also investigated.

6.1 Laminar Flow Past a Swept Fin

6.1.1 Computation of 0° Swept Fin Flow Field

The incoming flow conditions for this case are given in Sec. 5.1.1. The computations were carried out using a 40 x 40 x 40 mesh. Figure 6.1 shows the comparison of pressure distribution along the fin leading edge. The leading edge pressure is normalized by the pitot tube pressure behind the bow shock wave. The results show that the computed pressure distribution agrees well with the experimental values. The existence of a peak pressure on the fin leading edge is noticed around Z/D = 1.5. The minimum pressure is seen to occur around Z/D = 0.25. In the downward direction from this point, the pressure is seen to increase slowly towards the plate surface. The computed results, therefore, appear to demonstrate the physically realistic trend.

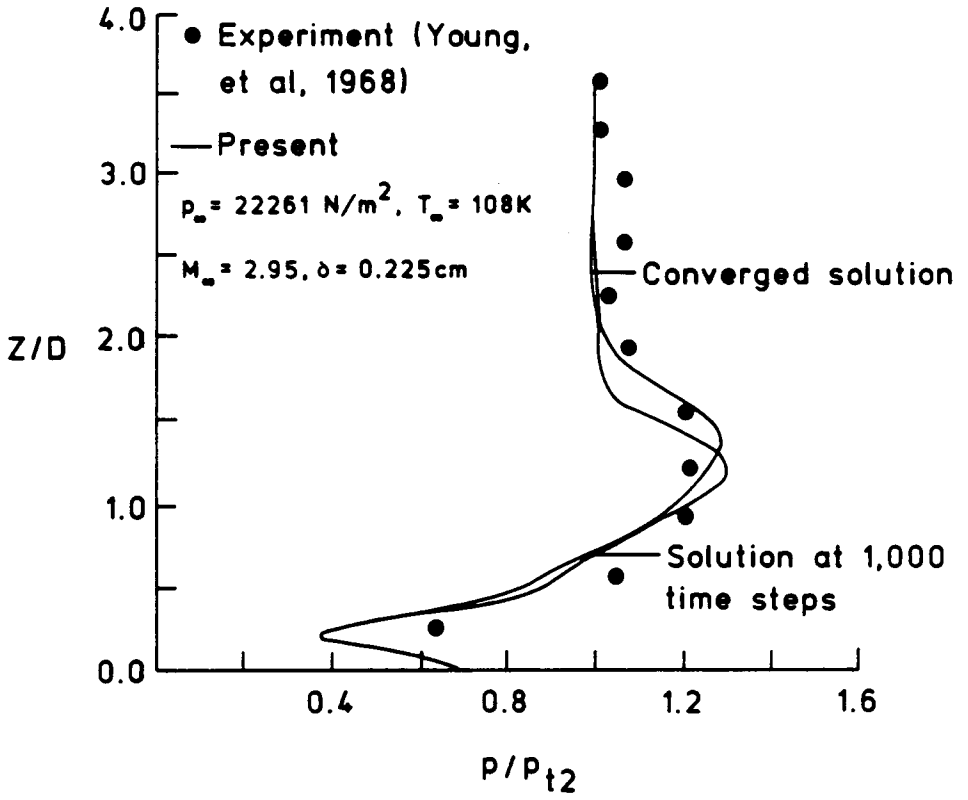

Fig 6.1 Pressure distribution on the blunt fin leading edge and comparison with experiment

As pointed out by Hung and Buning [31], the existence of peak pressure on the fin is due to multicompression of the separation shock. The decrease of pressure from the peak to the minimum is due to extreme expansion created by the horseshoe vortex leading to a reversed supersonic zone on the fin. The pressure increase in the direction towards the plate surface is due to recompression from supersonic to subsonic flow. This creates an adverse pressure gradient in the direction toward the plate, resulting in a supersonic zone on the fin.

The computed pressure distribution on the flat plate along the line of symmetry is compared with the experimental measurement for an unswept fin in Fig. 6.2. The results show good overall agreement except near the juncture point. The main features of the flow such as upstream influence, pressure plateau, and the pressure rises across the fin bow shock and plate separation shock are all well simulated by the numerical code. The existence of low pressure following the separation pressure rise is due to the reversed high speed flow leading to a reversed supersonic zone above the plate surface.

6.1.2 Parametric Effect of Fin Sweep and Boundary Layer Thickness

The pressure distribution on the fin leading edge is illustrated in Fig. 6.3 for various fin sweep angles corresponding to the conditions given in Sec. 5.1.2. The results are compared with the blunt fin case using an identical mesh. It is seen that as the fin sweep increases, the location and magnitude of the peak and minimum pressures decrease drastically. As pointed out by Edney [55], the magnitude of the heating rate and peak pressure on the fin leading

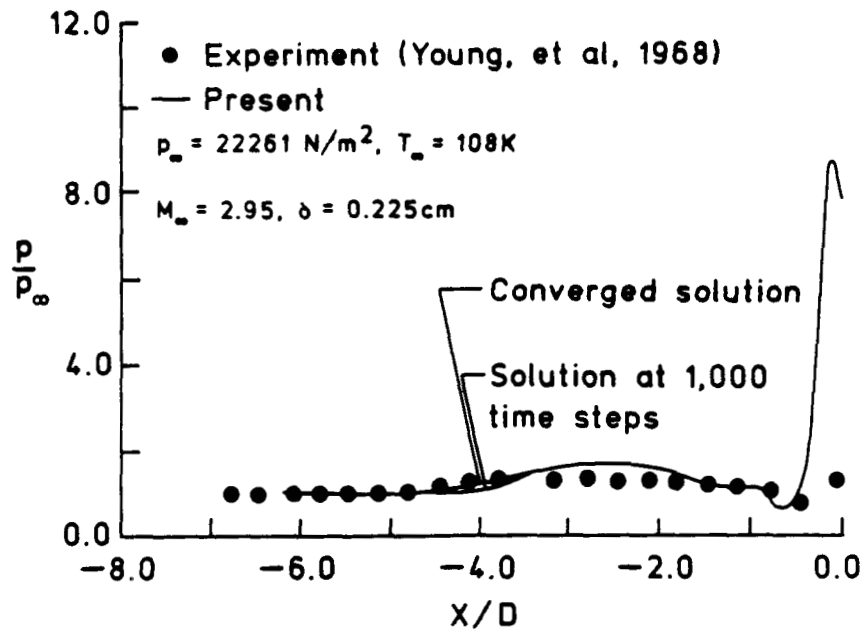

Fig. 6.2 Pressure distribution on the flat plate and comparison with experiment

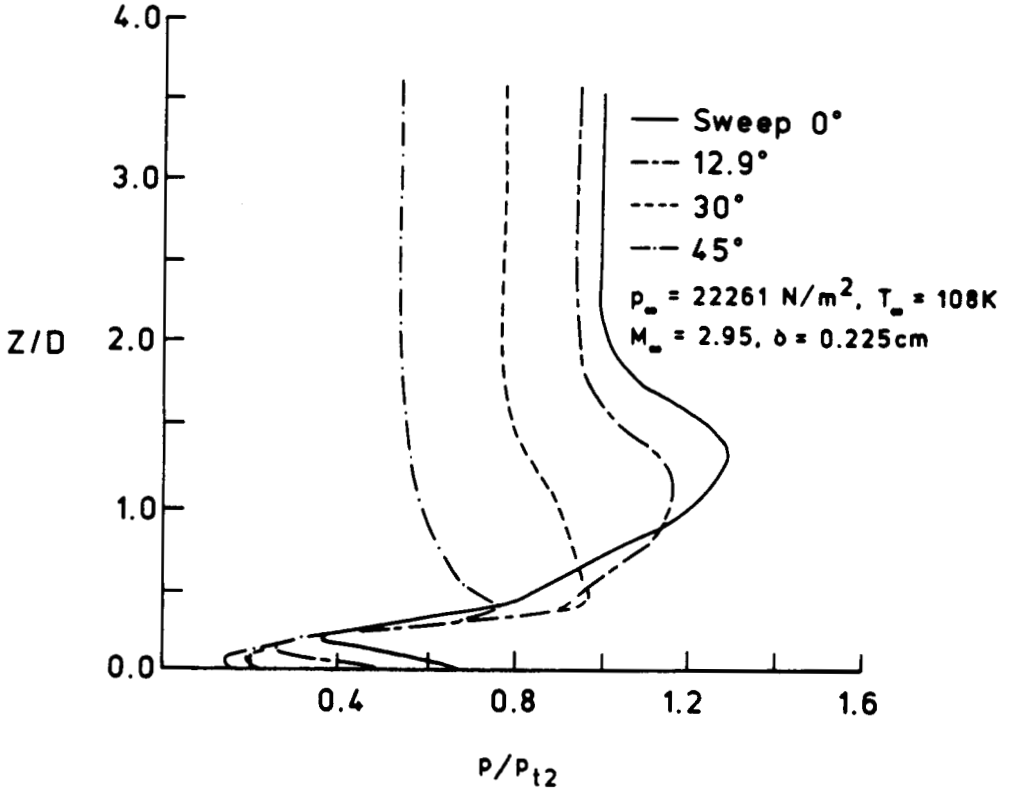

Fig 6.3 Pressure distribution on the fin leading edge for various fin sweeps

edge depend essentially on the geometrical parameters such as the fin sweep. As the fin sweep angle increases the supersonic jet becomes thinner and may strike the fin leading edge far downstream of the impingement point where, because of diffusion its effect on the heat transfer and peak pressure may be considerably lower than for the unswept case. Edney further observed that as the fin sweep increases above a certain critical value, the resulting shear layer may miss the fin leading edge entirely, and hence, high pressure and heat transfer do not occur.

Comparison of the pressure distribution on the flat plate is shown in Fig. 6.4 for various fin sweep angles. It is noted that as the fin sweep angle increases, the separation point on the plate surface moves downstream. Also, the peak pressure at the corner decreases drastically with increasing sweep angle. Although no comparison of pressure distribution has been made with experimental measurements for the swept fin case, the computed results agree qualitatively in trend with the Price and Stallings [17] data for a turbulent boundary layer.

To further demonstrate the effect of fin sweep on the interaction flow field, the code was run for a thick incoming laminar boundary layer for conditions given in Sec. 5.1.2. The boundary layer thickness, in the previous case, was very small. Hence, packing a fine grid in this region created some instability in the numerical simulation. To remedy this situation and also to observe the detailed effect of the fin sweep on the interaction flow field, the code was run for 0° and 45° fin sweeps. The computations were carried out using a 40 x 40 x 40 mesh.

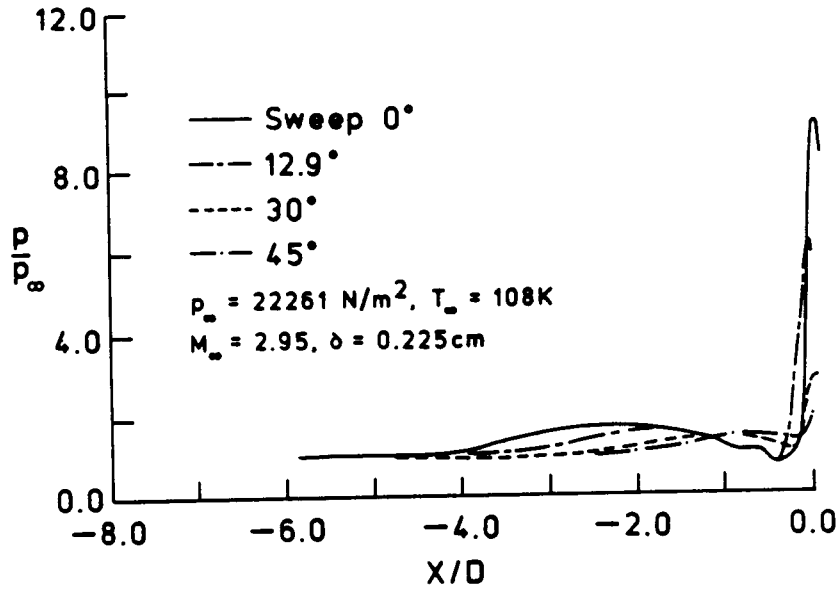

Fig. 6.4 Pressure distribution on the flat plate for various fin sweeps

Figure 6.5 shows the computed pressure distribution on the fin leading edge for 0° and 45° swept fins. The results clearly demonstrate the dramatic influence of the fin sweep on the pressure distribution. It is seen that as the fin sweep increases, the peak pressure and its location along the fin leading edge decreases dramatically. The location and magnitude of minimum pressure on the fin leading edge also shows a drastic variation in the 45° sweep case as compared to the 0° sweep case.

Figure 6.6 shows the comparison of pressure distribution on the flat plate ahead of the fin leading edge for 0° and 45° swept fins. It is seen that as the fin sweep angle increases the point of separation of the incoming flow moves closer to the fin leading edge. Also, as the sweep increases, no definite first peak in pressure is observed. The final pressure jump across the fin leading edge shock also shows a drastic reduction in the pressure for the 45° swept fin as compared to the 0° swept fin. This is because the flow goes through a severe adverse environment, since the fin bow shock is aligned normal to the incoming flow for the 0° sweep fin. In the case of the 45° swept fin, the incoming flow goes through the oblique bow shock formed ahead of the fin and suffers less severe change as compared to the 0° swept fin. This is the reason for reduction in the level of the peak pressure of the flow ahead of the 45° swept fin.

Figure 6.7a and 6.7b show the Mach number contours in the plane of symmetry for 0° and 45° swept fins. The separation shock, fin bow shock, and the two reversed supersonic zones (in the case of 0° sweep) have been clearly identified. As the sweep angle increases, the Mach number contours show clearly the decrease in the extent of the

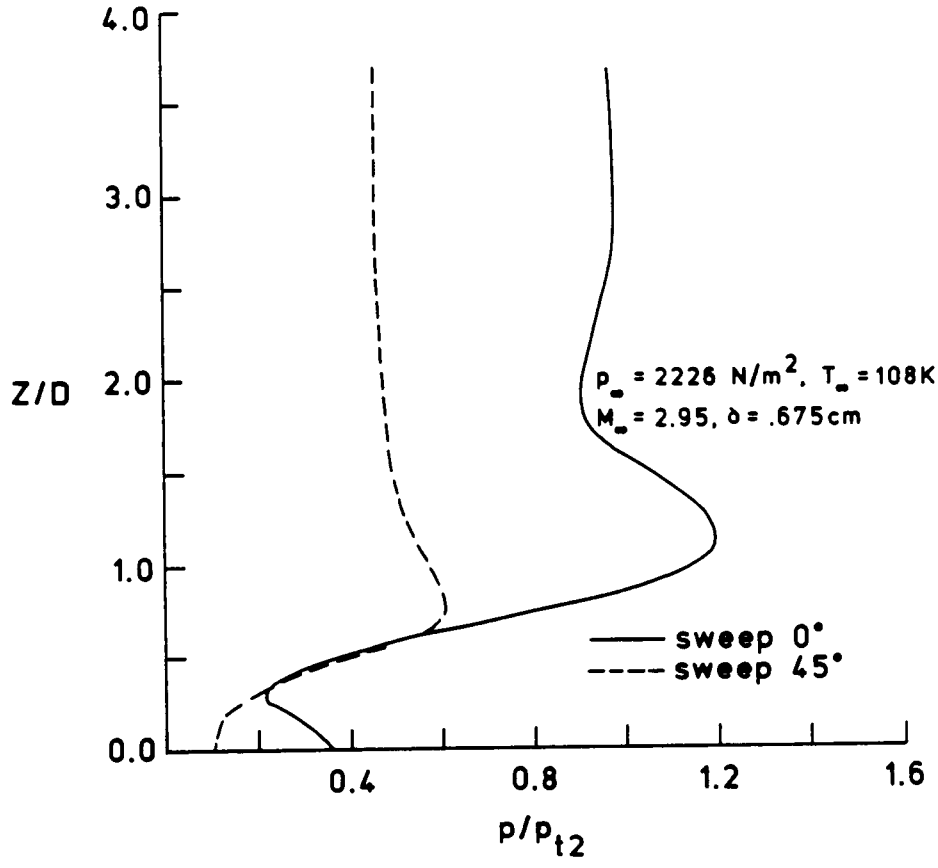

Fig. 6.5 Pressure distribution on the fin leading edge for various fin sweeps in a thick laminar boundary layer

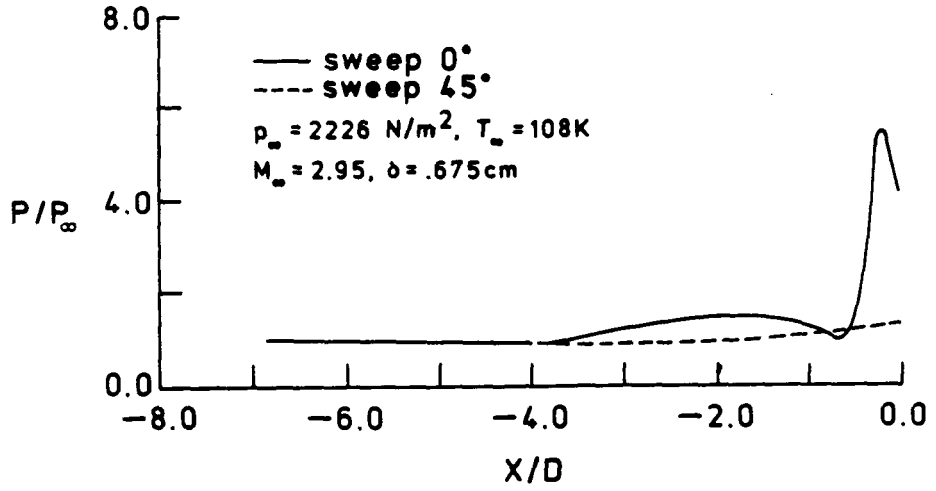

Fig. 6.6 Pressure distribution on the flat plate for various fin sweeps in a thick laminar boundary layer

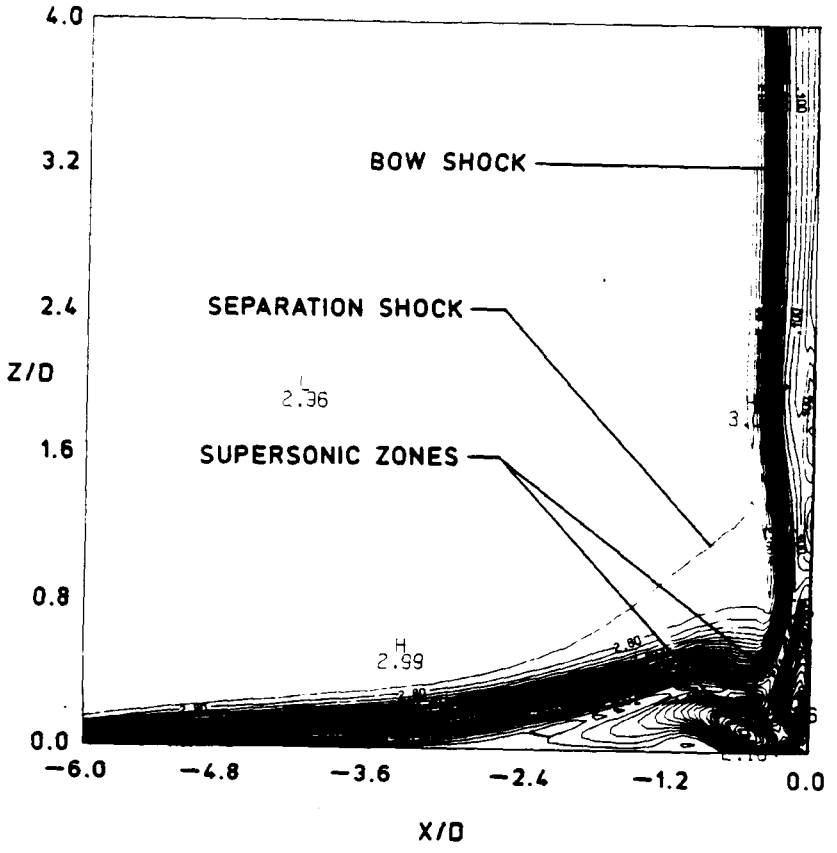

Fig. 6.7 Mach number contours in the plane of symmetry for various fin sweeps: (a) sweep angle = 0°

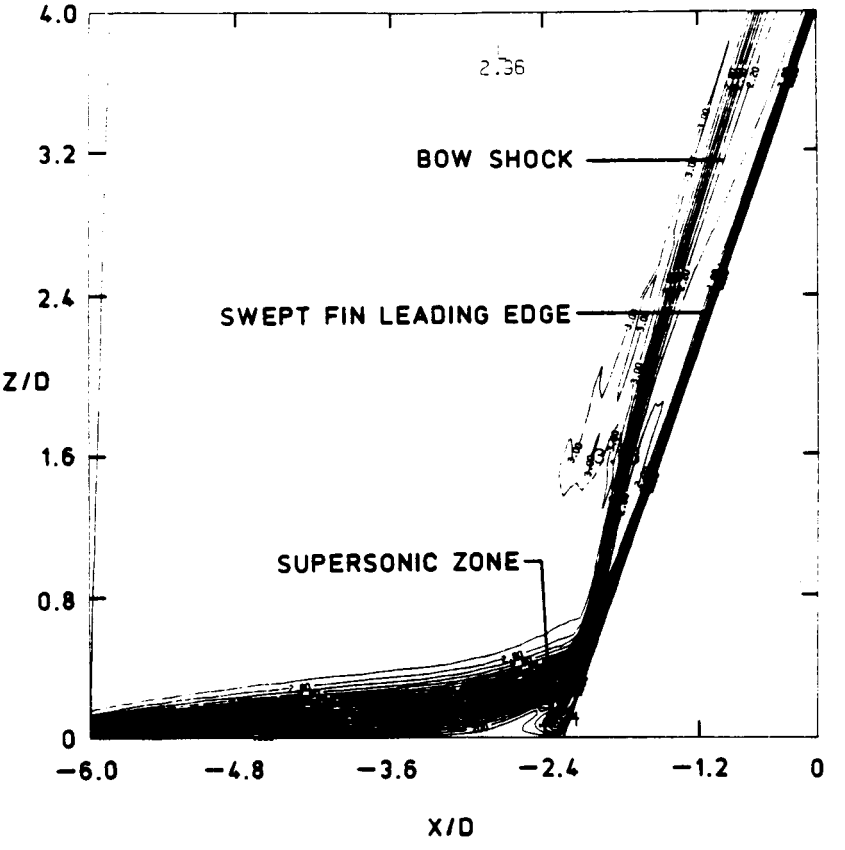

Fig. 6.7(continued) (b) sweep angle = 45°

separated region. It is noted that the two reversed supersonic zones (one on the fin and one on the plate) are eliminated in the 45° swept fin case. A large variation in the Mach number is noted behind the fin bow shock for the 0° sweep fin as compared to the 45° swept fin.

The normalized static pressure contours in the plane of symmetry are shown in Figs. 6.8a and 6.8b for 0° and 45° swept fins. The regions of high pressure at the fin leading edge and low pressure at the corner are clearly seen in the contour plots. As compared to the unswept fin case, the pressure behind the shock for the 45° swept fin does not show large differences in the peak pressure. These two arguments demonstrate clearly the ameliorating effect of the fin sweep because the leading edge becomes more and more like a slender ellipse in the freestream direction with the increase in the sweep angle. This means with a swept blunt fin on a flat plate, there is a reduction in the upstream influence of the bow shock, and the effect of bluntness associated with the fin is compressed into a small interaction region. In fact, the sweep clearly reduces the magnitudes of the interaction and hence the pressure levels throughout the whole flow field. The corresponding density contours in the plane of symmetry are shown in Figs. 6.9a and 6.9b.

6.2 Laminar Flow Past a Blunt Fin

In this section, numerical results are compared with available experimental data. Also, the results of grid refinement and other parametric studies are presented and discussed.

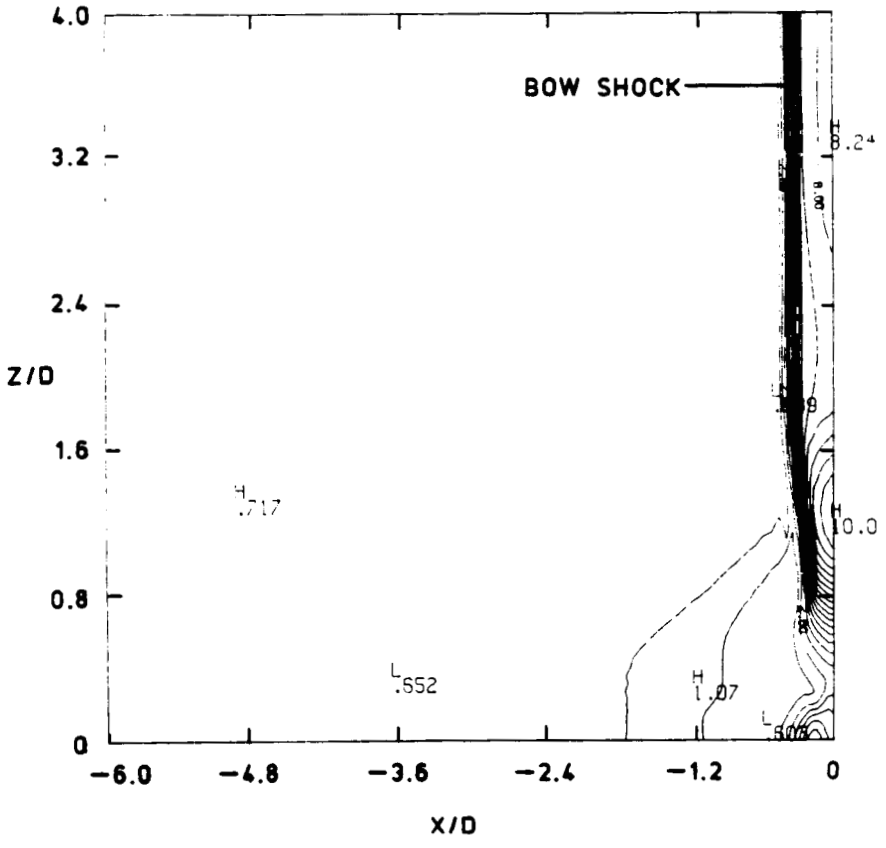

Fig. 6.8 Pressure contours in the plane of symmetry for various fin sweeps: (a) sweep angle = 0°

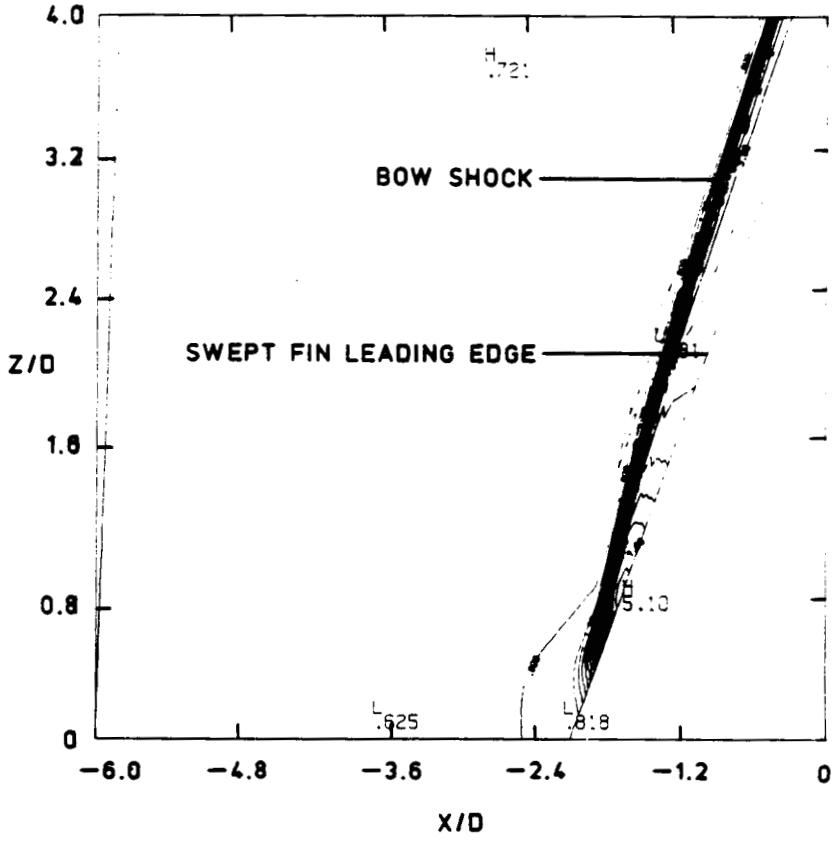

Fig. 6.8(continued) (b) sweep angle = 45°

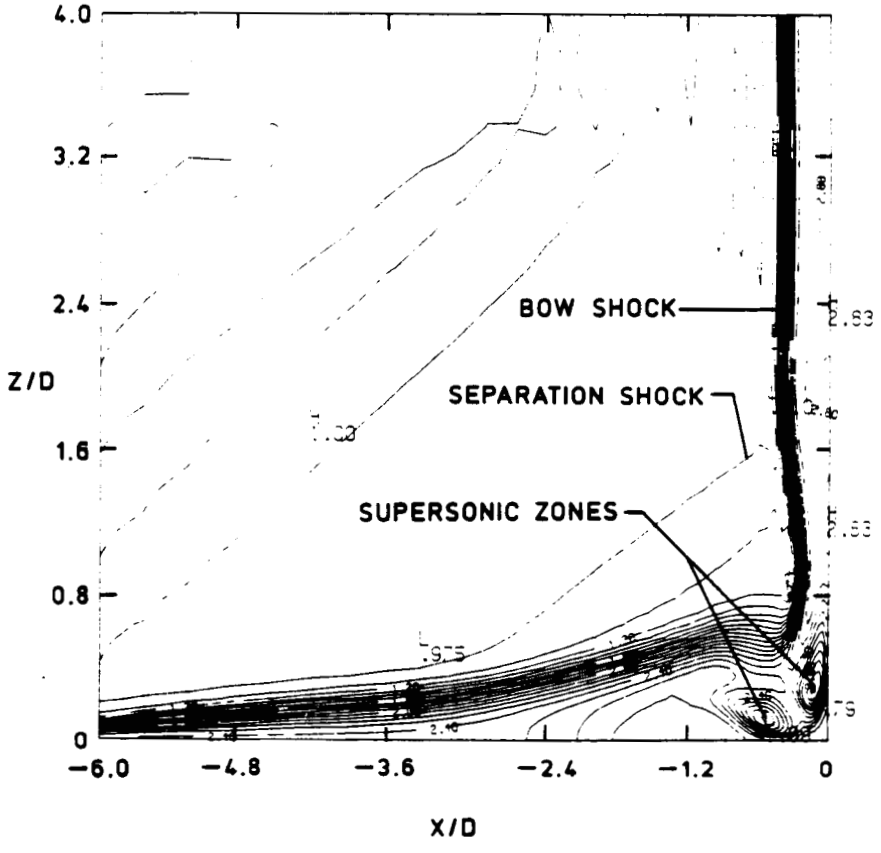

Fig. 6.9 Density contours in the plane of symmetry for various fin sweeps: (a) sweep angle = 0°

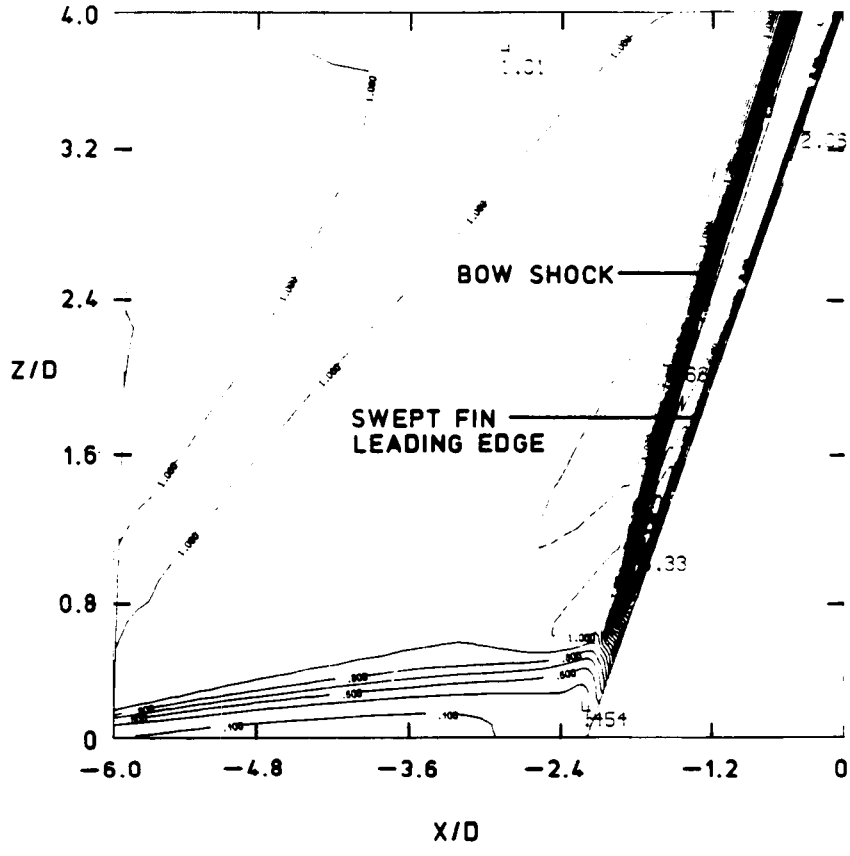

Fig. 6.9(continued) (b) sweep angle = 45°

6.2.1 Comparison of Computations with Experimental Data

The base computations for this case have been carried out using a 30 x 50 x 30 mesh. The tunnel flow conditions are given in Sec. 5.2.1. The computed pressure distribution along the axis of symmetry and comparison with the experiment are shown in Fig. 6.10. It is apparent that in the experiment the pressure begins to rise at about ten diameters upstream of the fin leading edge. The separation occurs, in the experiment, further downstream (X/D = - 6.8) between the regions of initial pressure rise and pressure plateau. The pressure reaches a valley downstream of the plateau region and then increases across the detached bow shock. The secondary separation in the reversed flow occurs between the pressure valley and the pressure plateau. The computed results using the base grid (30 x 50 x 30) are in reasonable agreement with the experiment in the region upstream of the pressure plateau. As observed in the experiment, the location of separation and initial pressure rise are closely predicted by the computations. However, the agreement between the computed and experimental results is not very good downstream of the plateau. Further, the computed results fail to predict the length of the plateau region accurately.

The computed pressure distribution along the fin stagnation line ($\phi = 0°$), and along various ϕ = constant and X/D = constant lines on the fin surface, are shown in Figs. 6.11a and 6.11b. For $\phi = 0°$ and 45°, the fin leading edge pressure is referenced to the total pressure, p_{t2}, behind the normal shock. Otherwise, it is referenced to the freestream static pressure p_∞. It is clear from the computed results that the peak pressure on the fin surface decreases

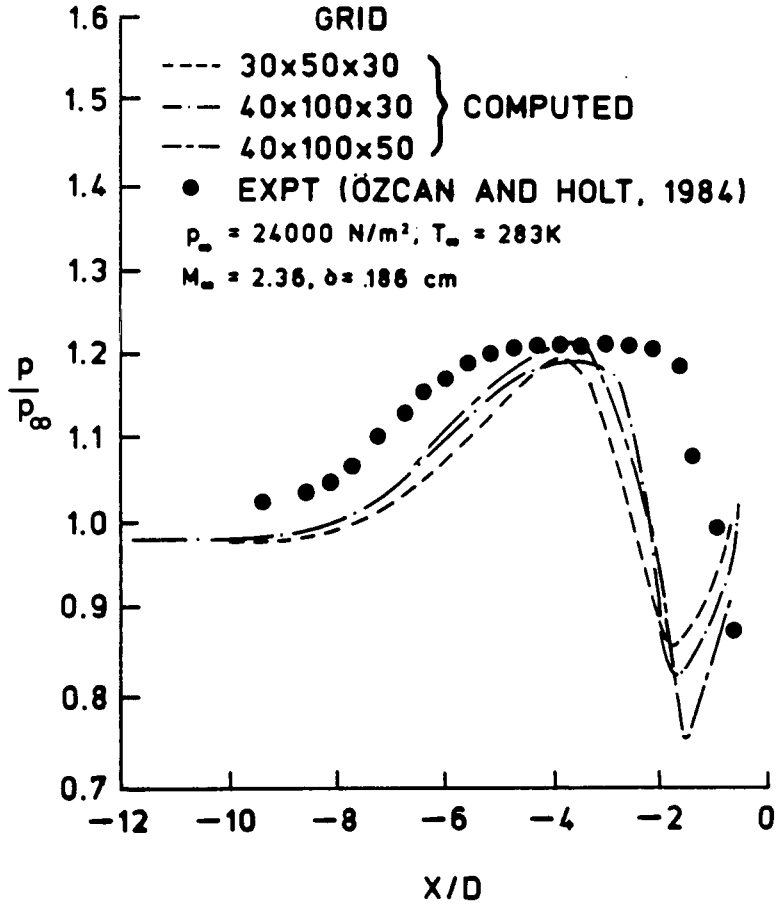

Fig. 6.10 Comparison of pressure distribution along the line of symmetry

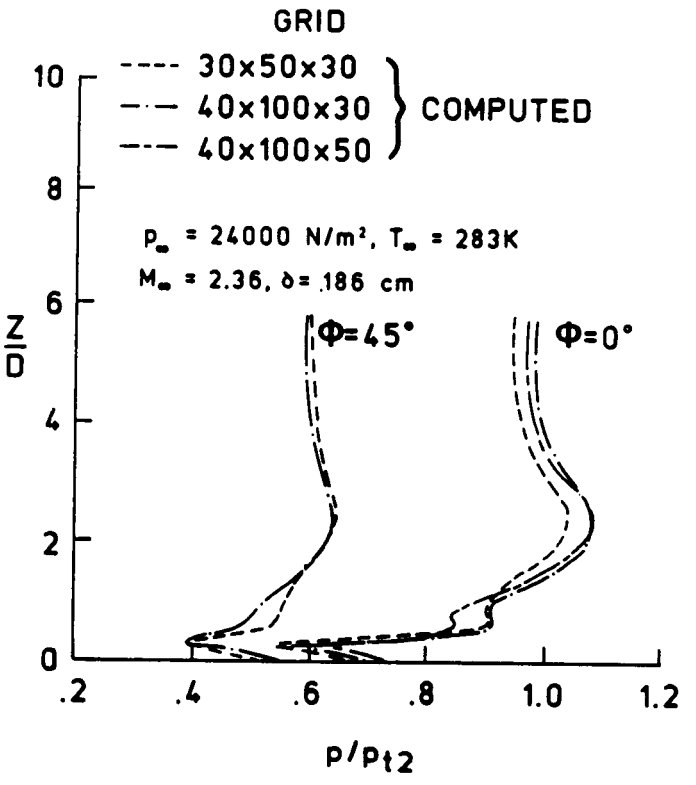

Fig. 6.11 Pressure distribution on the blunt fin: (a) along ϕ = 0° and 45°

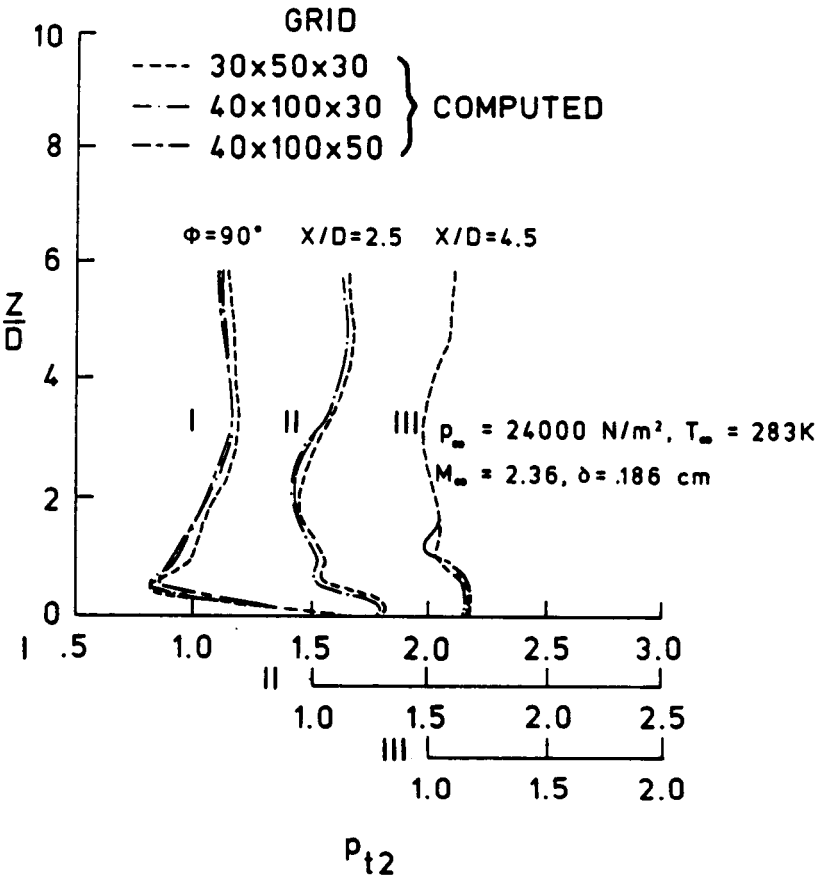

Fig. 6.11(continued) (b) along ϕ = 90° and X/D = 2.5 and 4.5

substantially as the flow expands around the blunt fin. The peak pressure on the fin surface at $\phi = 0°$ is about 1.1 and at $\phi = 45°$ it is approximately 0.6. The magnitude of the minimum pressure also drops at $\phi = 45°$ but not as much as the peak pressure. The pressure drops below the value of the total pressure p_{t2} behind the normal shock. The computed results along the fin side face (Fig. 6.11b) show that the pressure drops below the value of freestream static pressure. As the flow continues to move downstream the extremely low pressure on the fin surface vanishes downstream of the shoulder.

The computed and the experimentally measured streamwise velocity profiles along the line of symmetry are shown in Fig. 6.12. The streamwise velocity component is nondimensionalized with reference to the freestream velocity U_e; U_e is nominally 560 m/sec. The dashed lines along the vertical axis show the displaced origin to avoid overcrowding of the figures. The streamwise velocity profiles along X/D = -8.0 and -7.2 (Fig. 6.12a) indicate preseparation behavior. The velocity profile at X/D = -6.4 indicates that the separation occurs in close vicinity of X/D = -6.4. In the experiment, the separation occurs around X/D = -6.8. However, it was difficult to make repeatable measurements at that location due to the inherent unsteadiness of the flow. Also, due to the small scale of the reversed flow region at X/D = -6.4, it was found difficult to detect the reversed flow region in the vicinity of the primary separation line. The velocity profile at X/D = -5.6 clearly shows the reversed flow region. The velocity profiles at X/D = -4.8, -4.0, and -3.2 are shown in Fig. 6.12b. These results show that the magnitude and height of the reversed flow region increases with increasing X/D. The streamwise velocity profiles

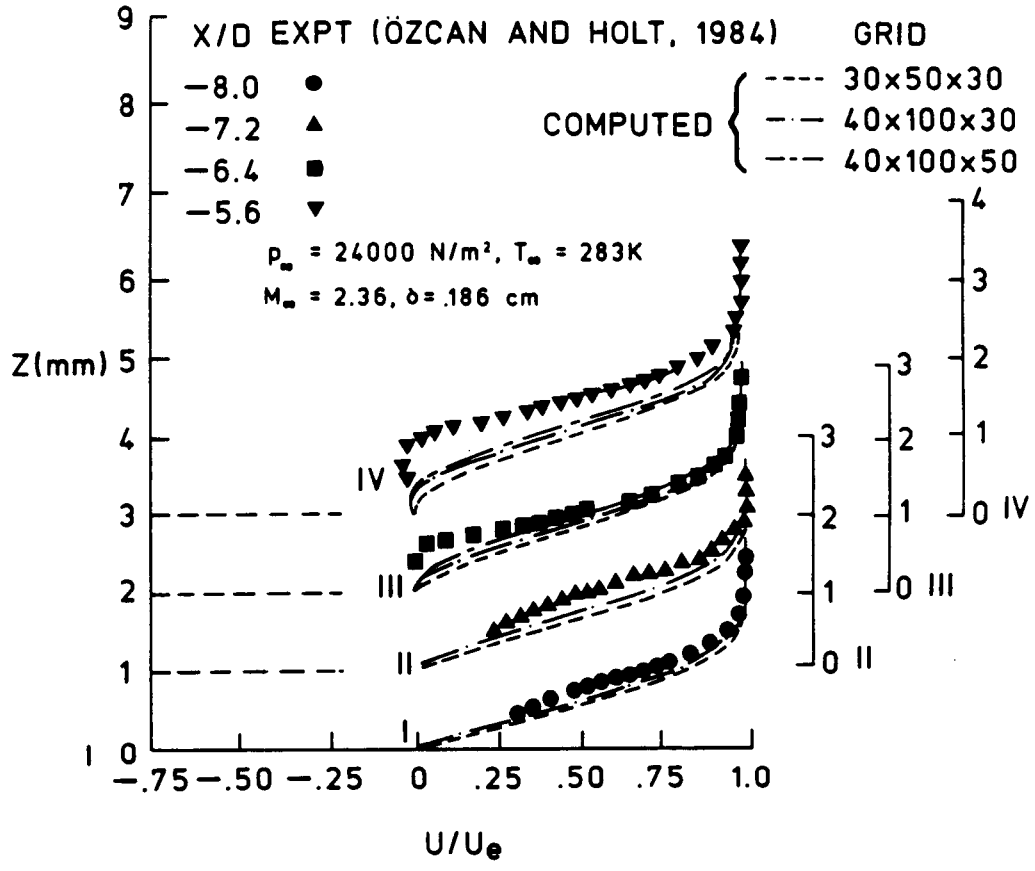

Fig. 6.12 Comparison of streamwise velocity profile: (a) along X/D = -8.0, -7.2, -6.4 and -5.6

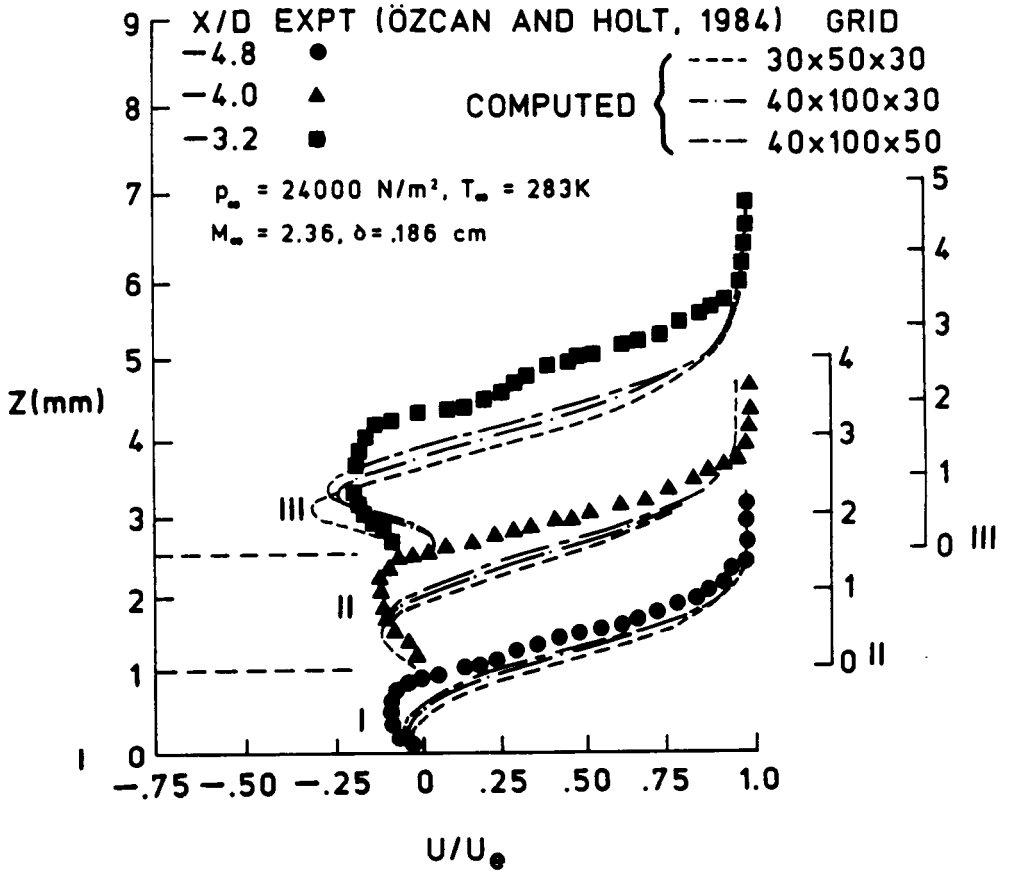

Fig. 6.12(continued) (b) along X/D = -4.8, -4.0 and -3.2

at X/D = -2.4 and -1.6 are given in Fig. 6.12c. The experimental measurements show that the maximum magnitude of the reverse velocities at these two locations are approximately equal. At these locations, computed results deviate significantly from measurement. The height of the reversed flow region decreases with increasing X/D. The measured streamwise velocity profiles at X/D = -3.2, -2.4, and -1.6 display significant kinks between the outer edge of the reversed flow region and the edge of the boundary layer. This phenomena is attributed to the inherent unsteadiness present in the flow. The computed velocity profiles do not display such behavior because the flow is assumed to be steady.

The vertical velocity profiles at X/D = -4.8, -4.0, -3.2, -2.4, and -1.6 are shown in Figs. 6.13a and 6.13b. The maximum velocity occurs around the outer edge of the boundary layer. The magnitude of the velocity then starts decreasing in the z-direction towards the freestream. The maximum velocity toward the plate and the height of the reversed flow region Fig. 6.12a,b,c increases with increasing X/D.

The postulated mean streamline pattern shown in Fig. 2.2 requires positive streamwise velocities close to the flat plate slightly upstream of secondary and tertiary separation lines. The flow structure observed in the junction demonstrates that across the boundary layer, in the vicinity of secondary and tertiary separation lines, the vertical velocities remain positive. Moreover, the vortical pattern also requires that the vertical velocity profile change its sign more than once during a streamwise traverse along various z = constant lines. However, the present vertical velocity profiles do not show such

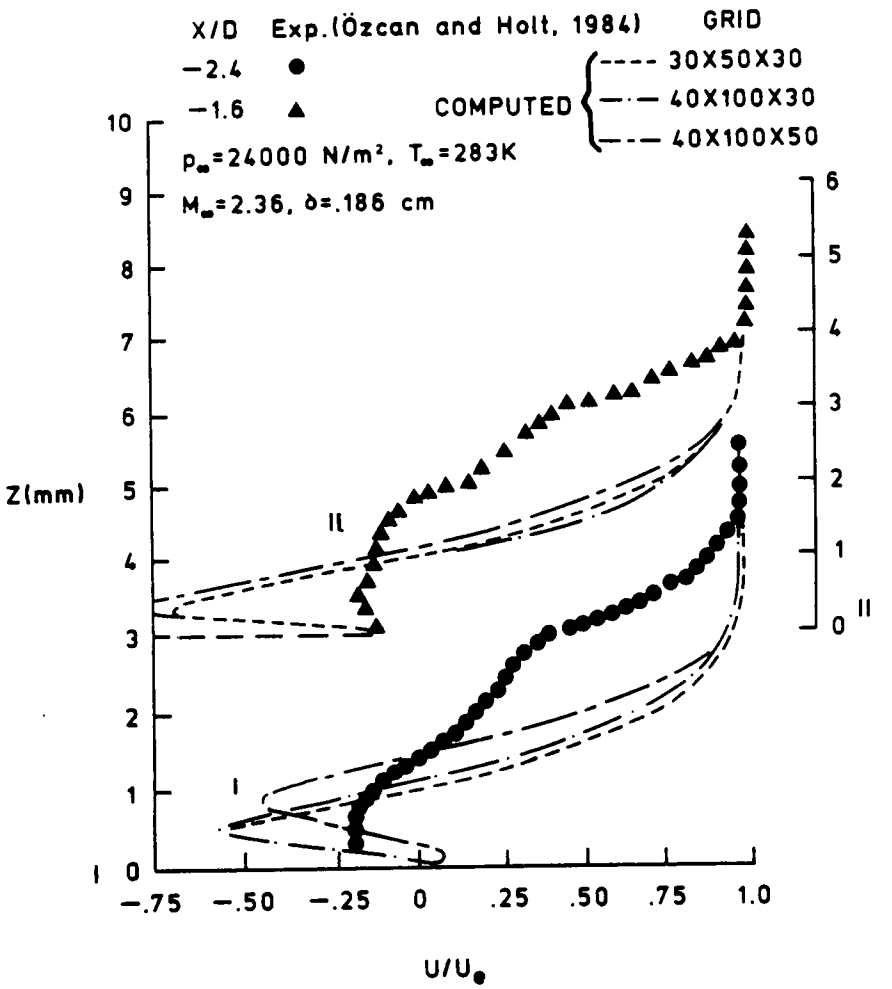

Fig. 6.12(continued) (c) along X/D = -2.4 and -1.6

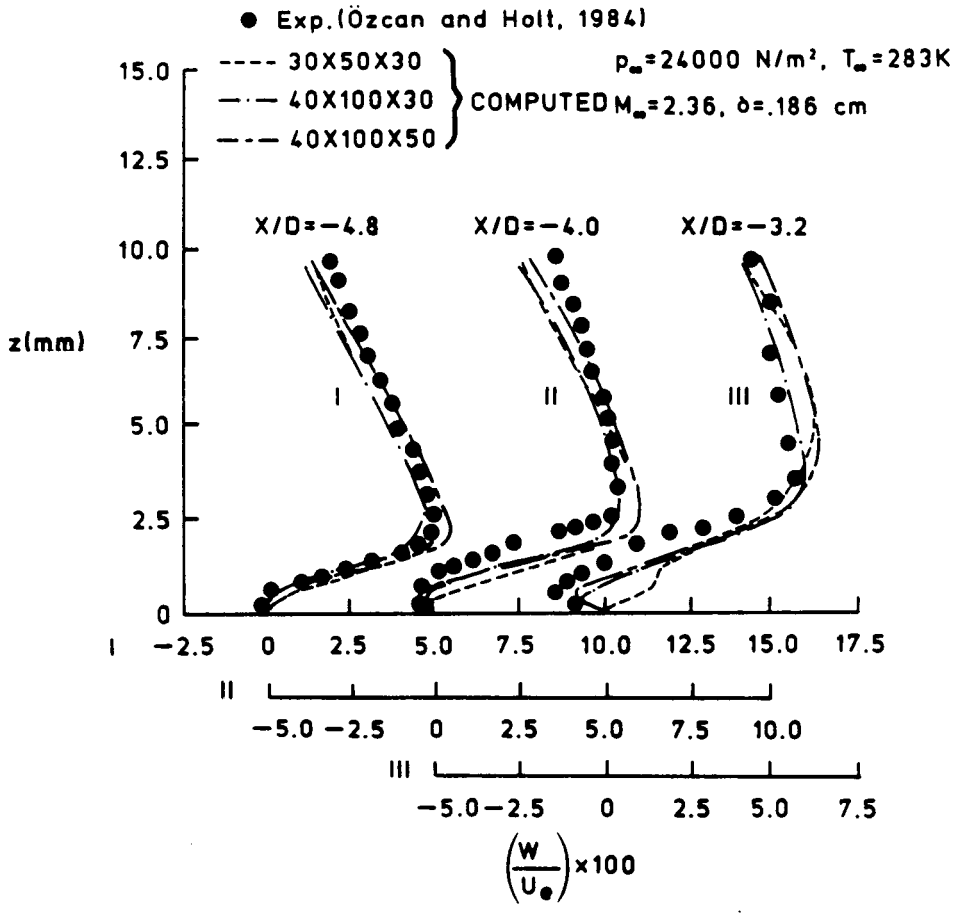

Fig. 6.13 Comparison of vertical velocity profile: (a) along X/D = -4.8, -4.0 and -3.2

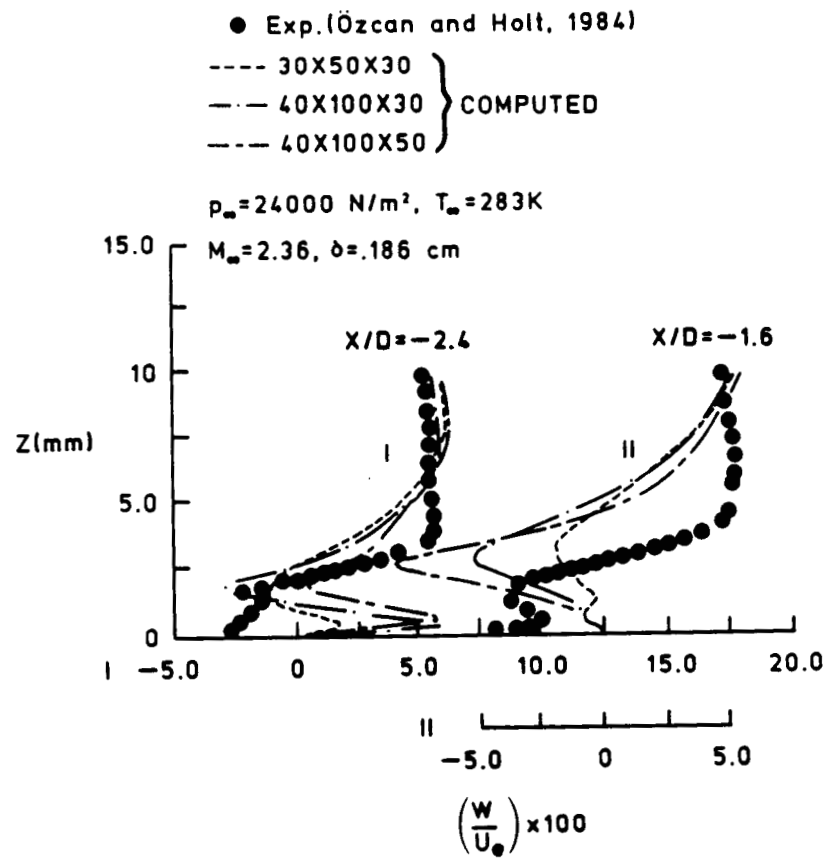

Fig. 6.13(continued) (b) along X/D = -2.4 and -1.6

behavior. It can be hypothesized that the locations of vortex centers are time dependent, but the time averaged surface locations where the vortices are shed remain approximately constant. Thus, the streamline pattern given in the plane of symmetry can be considered as one of the possible streamlines which succeed each other in time. Tobak and Peake [56] have shown such a postulated sequence of the cyclic vortical structures in low speed laminar flow past a circular cylinder. The unsteady nature of high speed laminar flow can be similar to low speed laminar flow. However, further study is required to understand the unsteady nature of this type of flow field. The limiting streamline patterns on the plate surface shown in Fig. 6.14 depicts the separation and reattachment lines on the flat plate. The primary separation, corresponding to the most upstream separation location of the plate boundary layer, occurs roughly at about X/D = -6.2. The reattachment line of the flow is located very close to the fin.

6.2.2 Effect of Grid and Flow Parameters

In this subsection, the results of the parametric study of grid resolution and variation in Mach and unit Reynolds numbers are presented. For various cases, the flow field is investigated for the freestream conditions given in Sec. 5.2.2.

The effects of grid refinement on the wall pressure distribution along the line of symmetry are shown in Fig. 6.10. These results demonstrate that computations using three different grids yield identical results except for the variation in the magnitude of the pressure valley. The computed pressure distribution along $\phi = 0°$ and $45°$ are shown in Fig. 6.11a. Further plots of pressure distribution along

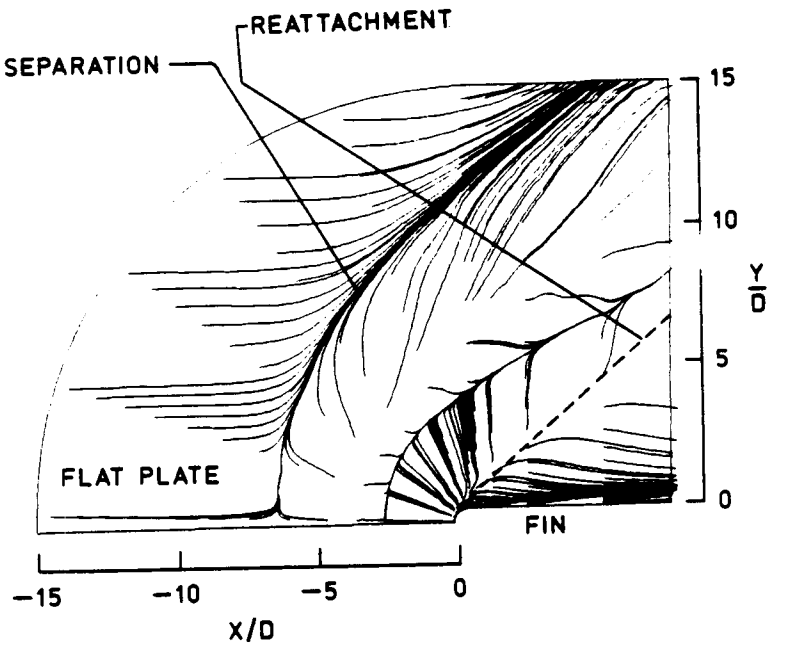

Fig. 6.14 Limiting streamlines on the flat plate for laminar flow past a blunt fin

ϕ = 90° and downstream of the fin shoulder (X/D = 2.4 and 4.5) are shown in Fig. 6.11b. The pressure distribution along ϕ = 0° is most sensitive to the grid refinement.

The sensitivity of the grid on streamwise velocity profiles at various locations upstream of the fin leading edge are shown in Fig. 6.12. The most upstream separation location of the flat plate boundary layer is insensitive to the grid refinement. The computed results generally appear to move towards the experimental data with refined mesh. However, at X/D = -2.4 and -1.6 (Fig. 6.12c), the numerical prediction using fine mesh (40 x 100 x 50) still display large discrepancies with the experiment. The vertical velocity profiles and comparison with the experimental data for various streamwise locations are shown in Fig. 6.13. The coarse grid (30 x 50 x 30) solution at X/D = -4.0 and -3.2 show some discrepancy with the experiment for z-locations less than 2.5 mm. Computations using the fine grid are able to improve the prediction with the experiment at these locations.

The numerically simulated particle paths in the plane of symmetry for various grids studied are shown in Fig. 6.15. The solutions show the presence of two clockwise rotating primary vortices and a third counter clockwise rotating vortex at the corner. These results demonstrate that the structure of the flow is relatively insensitive to the grid employed.

The grid refinement study discussed in the previous paragraphs established that a 40 x 100 x 30 mesh is sufficient to predict the experimental measurements. The effect of Mach number on the pressure distribution in the plane of symmetry is shown in Fig. 6.16 using a 40

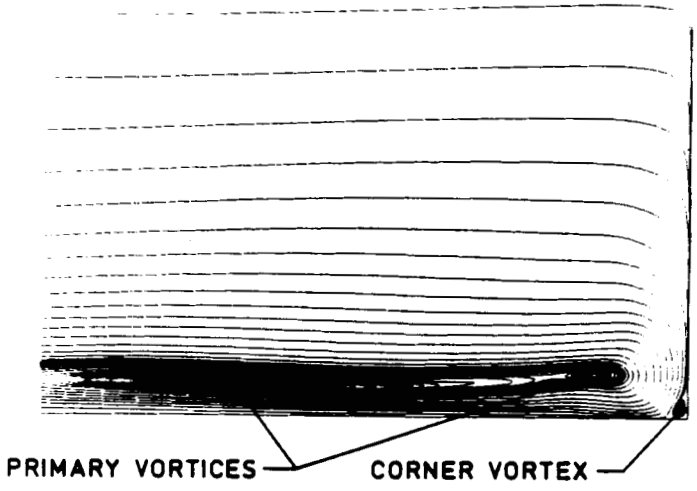

Fig. 6.15 Particle paths in the plane of symmetry for various grid refinements: (a) 30x50x30 grid

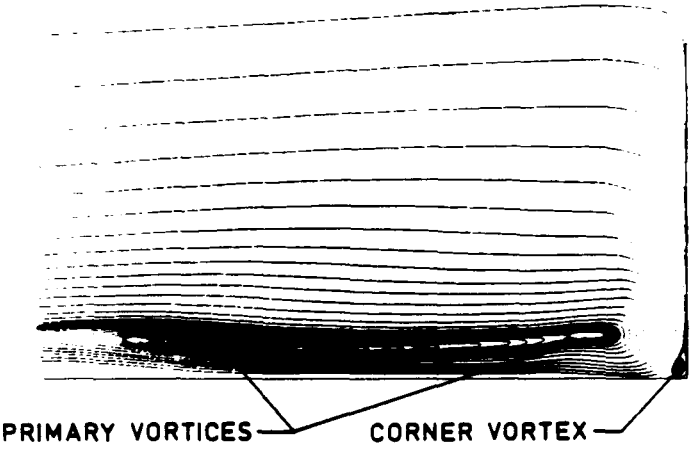

Fig. 6.15(continued) (b) 40x100x30 grid

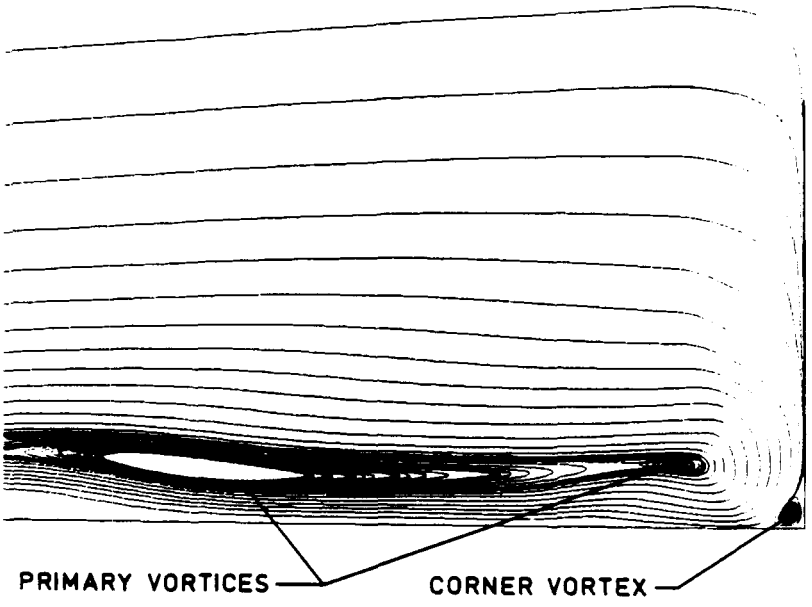

Fig. 6.15(continued) (c) 40x100x50 grid

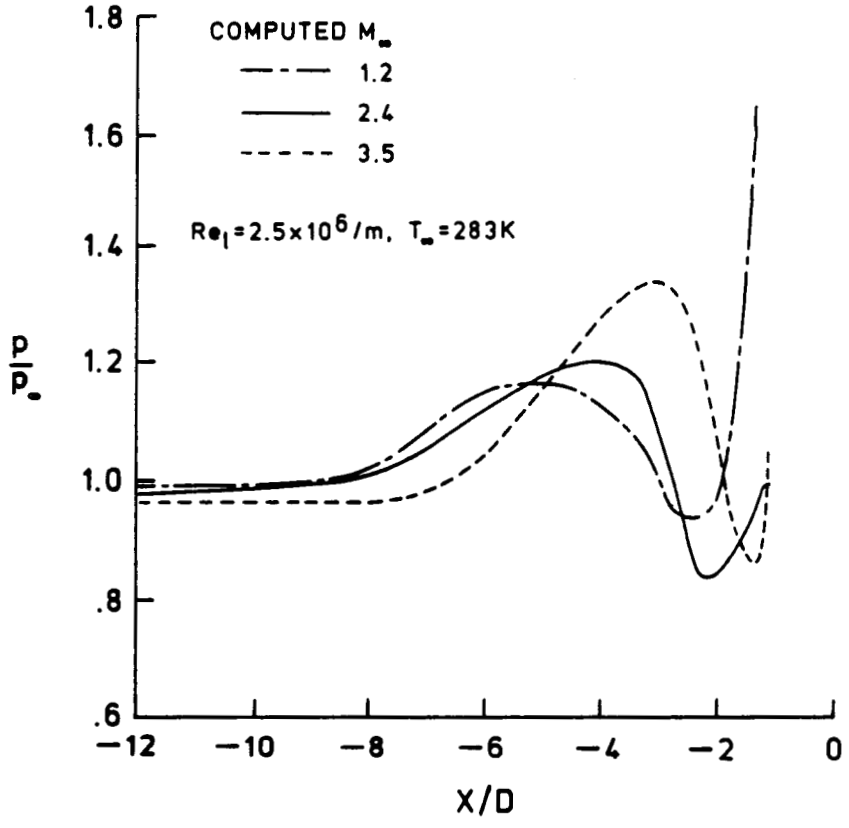

Fig. 6.16 Pressure distribution along the line of symmetry for various Mach numbers

x 100 x 30 mesh. The effect of increasing the Mach number is to decrease the length of the most upstream separation distance. Also the magnitude of the pressure plateau following separation increases with an increase in the Mach number. The pressure distribution along the fin stagnation line shown in Fig. 6.17 indicate that as the Mach number increases the z-location corresponding to the peak pressure decreases. However, the level of peak pressure remains constant for M_∞ = 2.36 and 3.5. The minimum pressure on the fin also shows a drastic reduction with increase in the Mach number. Also, the variation in pressure from a peak to a minimum increases with increasing Mach number.

The streamwise velocity profiles for various Mach numbers are shown in Figs. 6.18a and 6.18b at selected X/D locations. The effect of increasing the Mach number is to increase the maximum reverse velocity towards the flat plate. The simulated particle paths (in the plane of symmetry) at various Mach numbers are shown in Fig. 6.19. The results of Figs. 6.19b and 6.19c demonstrate that the flow at higher Mach numbers (M_∞ = 2.36 and 3.5) display no abrupt change in the vortical structure. However, at M_∞ = 1.2 (Fig. 6.19a), only a single vortex rotating in the clockwise direction can be seen as opposed to multi-vortex patterns observed at higher Mach numbers. Similar trends in flow patterns were observed by Baker [3] in low speed laminar flow where the number of vortices in the junction increases with freestream velocity.

The effect of unit Reynolds number on the pressure distribution along the line of symmetry is shown in Fig. 6.20. The effect of increasing the Reynolds number is to move the location of the first

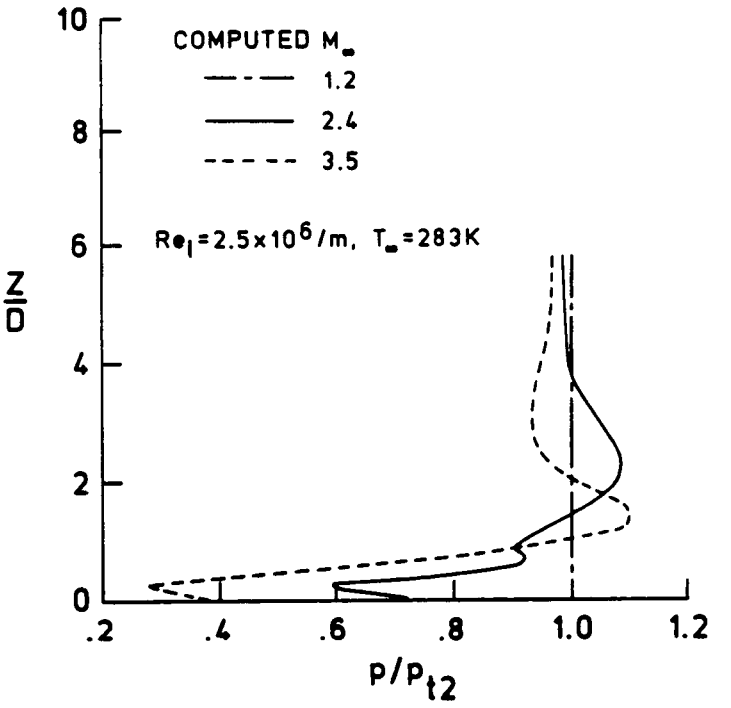

Fig. 6.17 Pressure distribution along the fin stagnation line for various Mach numbers

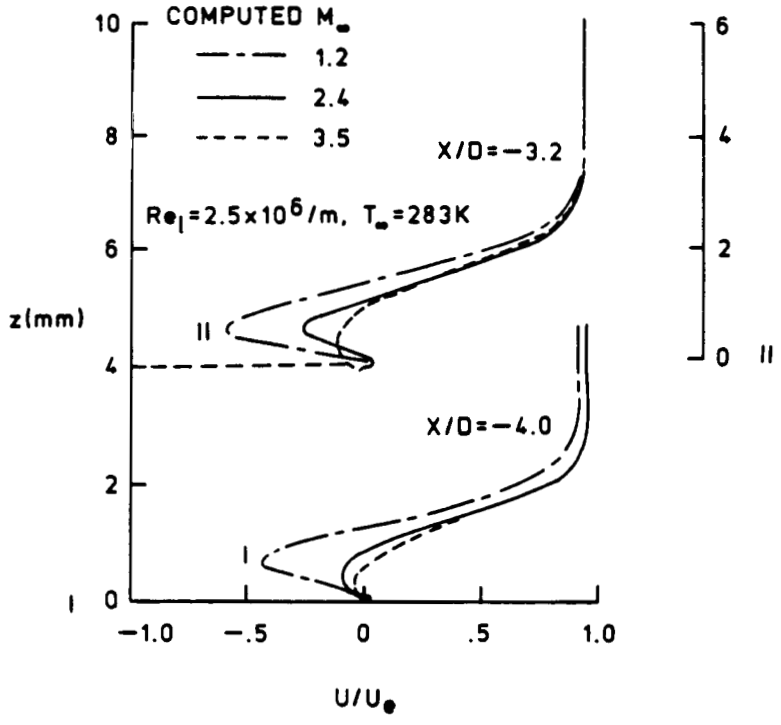

Fig. 6.18 Streamwise velocity profiles for various Mach numbers: (a) along X/D = -4.0 and -3.2

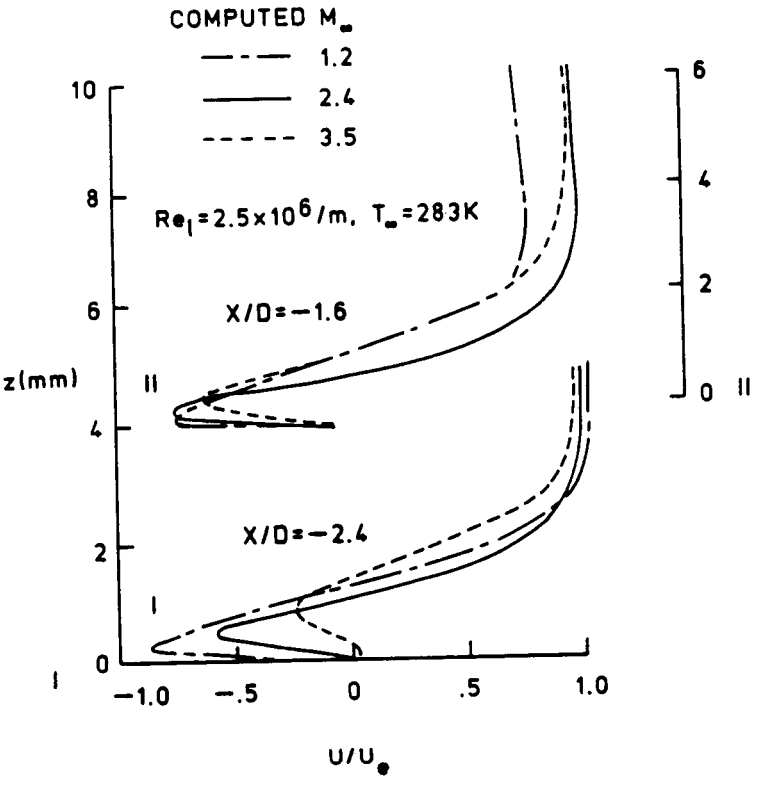

Fig. 6.18(continued) (b) along X/D = -2.4 and -1.6

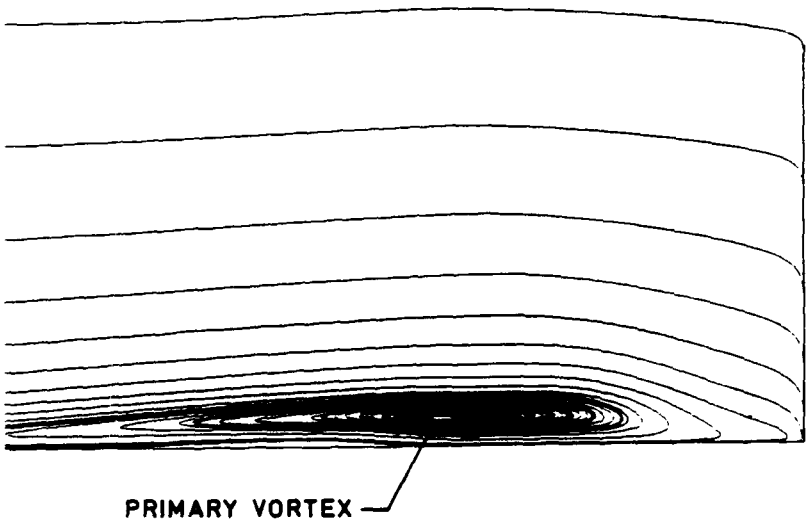

Fig. 6.19 Particle paths in the plane of symmetry for various Mach numbers: (a) $M_\infty = 1.2$

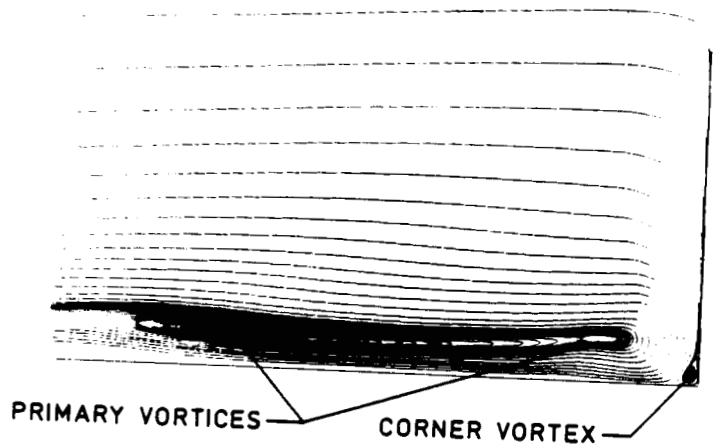

Fig. 6.19(continued) (b) $M_\infty = 2.36$

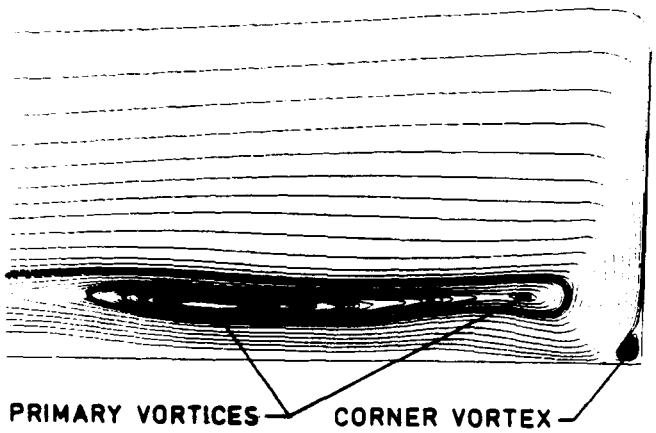

Fig. 6.19(continued) (c) $M_\infty = 3.5$

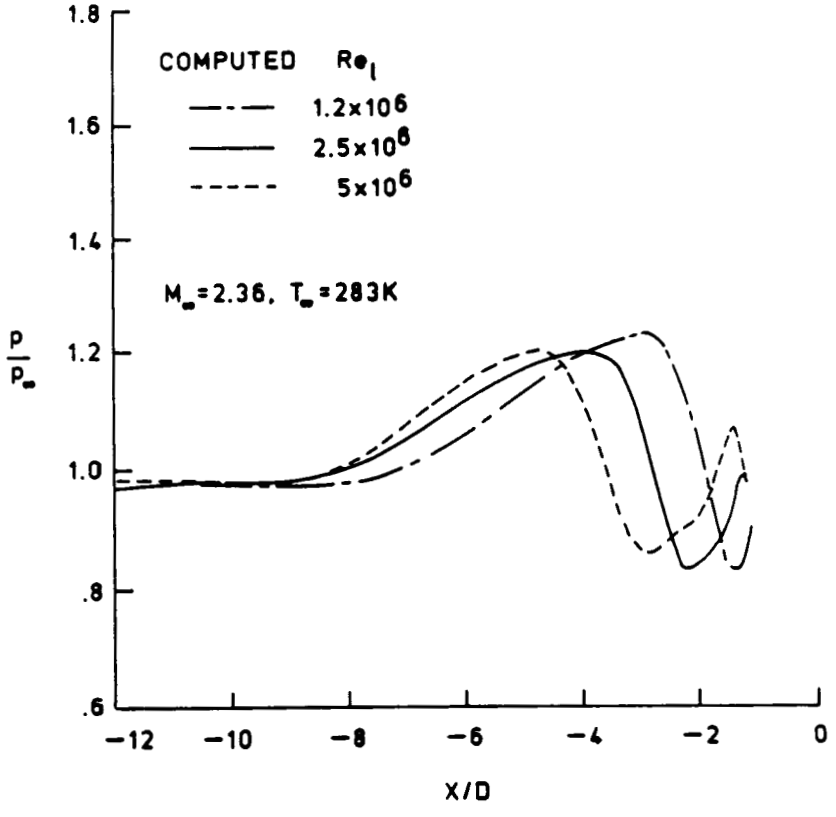

Fig. 6.20 Pressure distribution along the line of symmetry for various unit Reynolds number

peak in pressure slightly inboard toward the fin leading edge. The magnitude of the pressure plateau remains approximately constant. The pressure distribution along the fin stagnation line (Fig. 6.21) show that as the Reynolds number is increased, the z-location corresponding to peak pressure moves slightly upward. The minimum pressure around Z/D = 0.5 also shows a substantial variation to the increase in the unit Reynolds number.

The streamwise velocity profile at various X/D locations shown in Fig. 6.22 demonstrates that the maximum reverse velocity toward the plate increases with an increase in the Reynolds number. Also, the height of the reversed flow region above the flat plate decreases with an increase in the Reynolds number. The computed particle paths, in the plane of symmetry (Fig. 6.23), show the effect of Reynolds number on the flow structure. The flow structures at two higher Reynolds numbers (Fig. 6.23b and 6.23c) show the presence of three vortices, in contrast to the situation at the lowest Reynolds number (Fig. 6.23a) which depicts only two vortices.

6.3 Computation of Three-Dimensional Sharp Fin Flow Field

6.3.1 Flow Past a 16° Sharp Fin

The flow past a 16° sharp fin is simulated using the conditions given in Sec. 5.3.1. The computations were performed using a 40 x 45 x 45 mesh. The y^+ location of the first mesh point ahead of the interaction region is set at a distance of less than 5 wall units from the fin and flat plate surface. The present computations are compared with the previous numerical work of Horstman [56] and the experimental measurements of Peake [53] for identical flow conditions.

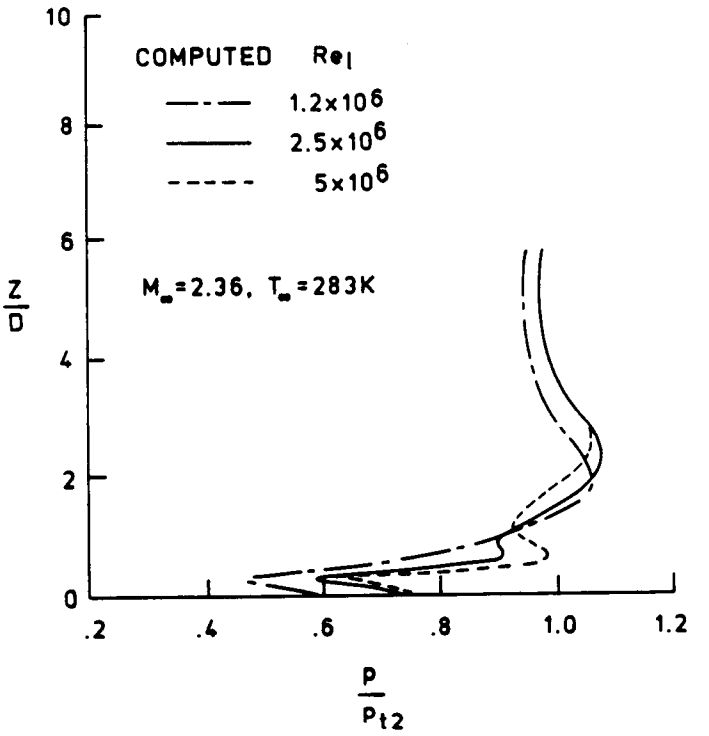

Fig. 6.21 Pressure distribution along the fin stagnation line for various unit Reynolds number

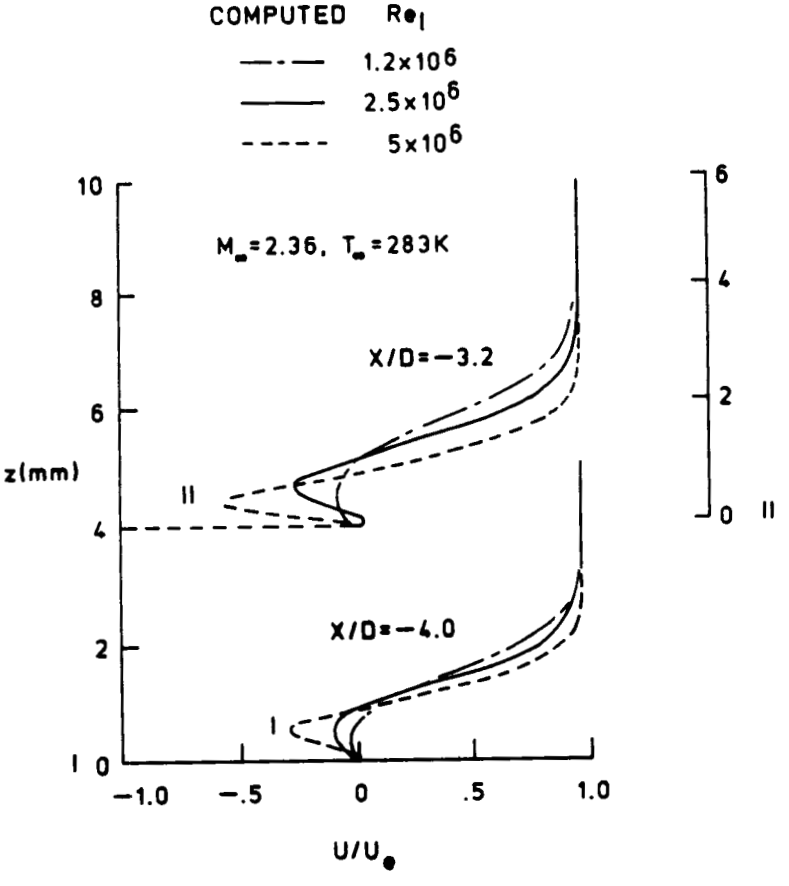

Fig. 6.22 Streamwise velocity profiles for various unit Reynolds number: (a) along X/D = -4.0 and -3.2

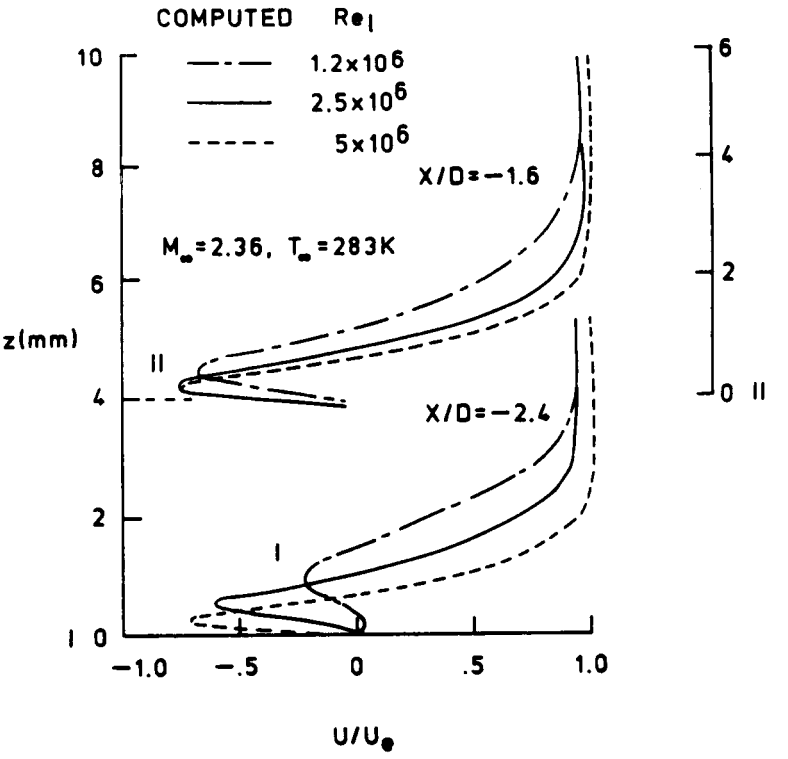

Fig. 6.22(continued) (b) along X/D = -2.4 and -1.6

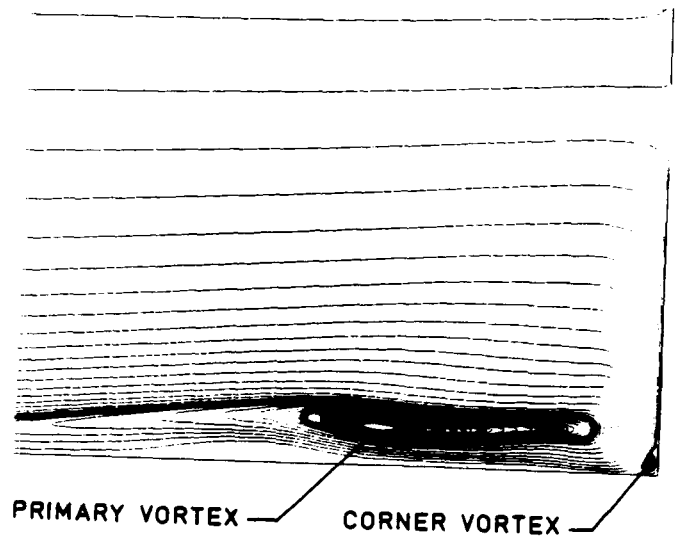

Fig. 6.23 Particle paths in the plane of symmetry for various unit Reynolds number: (a) $Re_{\ell} = 1.2 \times 10^{6} m^{-1}$

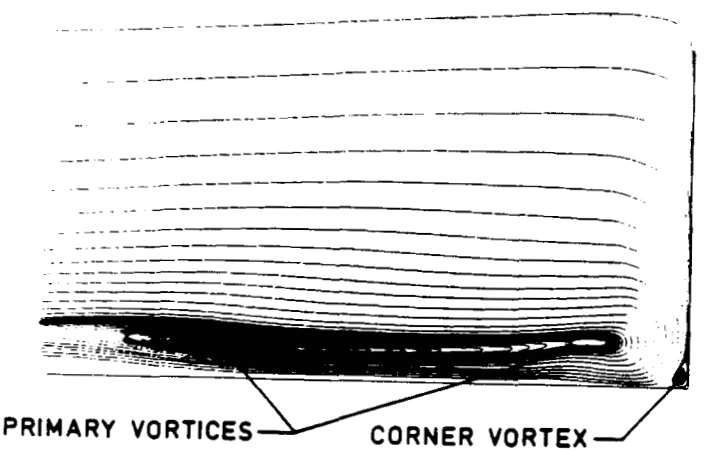

Fig. 6.23(continued) (b) $Re_{\ell} = 2.5 \times 10^{6} m^{-1}$

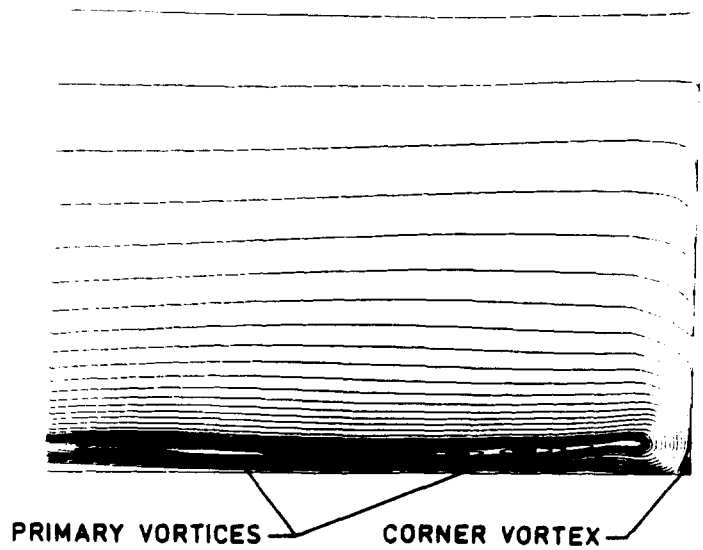

Fig. 6.23(continued) (c) $Re_{\ell} = 5x10^{6}m^{-1}$

The comparison of present results with previous numerical and experimental investigations are given in Figs. 6.24-6.26. Figure 6.24 shows the wall pressure distribution on the flat plate. The wall pressure is nondimensionalized with respect to the freestream static pressure. The abscissa $(x-x_{shock})$ is normalized with respect to the incoming boundary layer thickness δ_0 upstream of the interaction and x_{shock} is the axial location of the inviscid shock wave at a specified spanwise station.

The pressure distribution curve predicts a gradual pressure rise due to separation of the incoming boundary layer. The pressure then reaches a plateau followed by a final compression as the flow goes past the fin leading edge oblique shock wave. All of the features observed in the experiment are closely predicted by the present numerical simulation. It is interesting to see that the present calculation agrees very closely with the experiment as compared to the previous numerical simulation. A typical inviscid solution is also shown in Fig. 6.24. It is clear that the present calculations do not give a crisp representation of the shock structure due to the nature of the scheme employed in the present study.

A comparison of the computed surface yaw angles, $\tan^{-1}(v/u)$, with the experimental data is shown in Fig. 6.25. The maximum computed surface angle (from the present computation) is about 67.5° whereas previous computations have predicted an angle of about 88°. The maximum measured angle from the experiment is about 48°. Peake [53] observed some nonuniformities in the experiment due to upstream nozzle effects. A vortex generator was used upstream of the test section to improve the tunnel flow. Because of these conditions, the

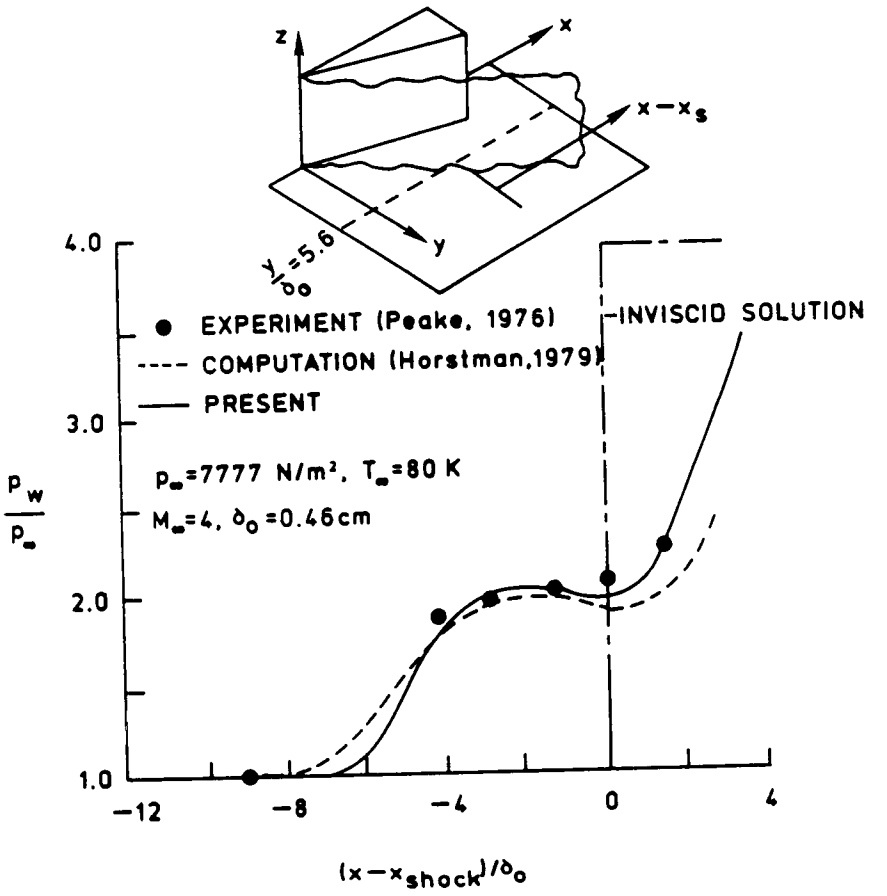

Fig. 6.24 Pressure distribution on the flat plate along Y/δ_o = 5.56 for 16° sharp fin

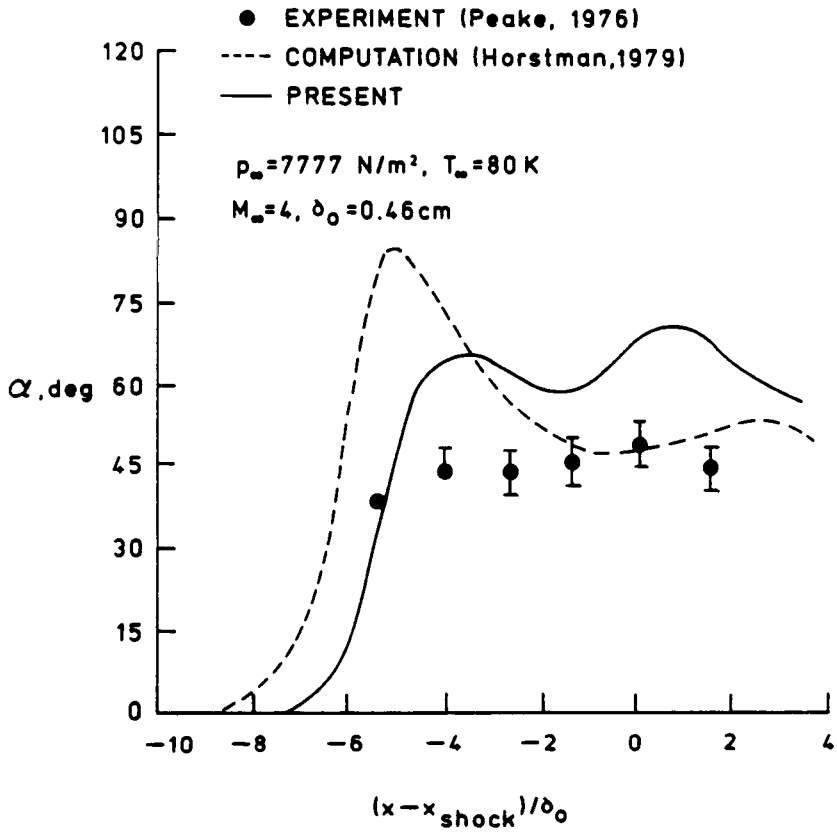

Fig. 6.25 Yaw angle distribution on the flat plate along Y/δ_o = 5.56 for 16° sharp fin

quality of the $M_\infty = 4$ experimental data may not be satisfactory. The symbols with arrows represent the uncertainty in the experimental data. The maximum difference between the computed results and the mean experimental data is about 40%. The computed skin friction results from the present and previous numerical simulations are compared with the experimental data (Fig. 6.26). The experimental results are seen to fall between the two sets of computed results.

6.3.2 Flow Past a 20° Sharp Fin

For the case of 20° sharp fin induced shock wave/boundary layer interaction, comparative results were obtained corresponding to the conditions given in Sec. 5.3.2. The computations employed a 30 x 50 x 50 mesh. The y location of the first mesh point is set at a distance of less than 5 wall units from the fin and plate surface. The present computational results are compared with the previous computational study of Knight et al. [57] and the experimental work of Shapey [54] for identical flow conditions.

The computed pitot pressure profile at station 1 and 2 (Fig. 5.2) located upstream of the interaction region are given in Figs. 6.27a and 6.27b. The computed and experimental pitot profiles at stations 3 through 8 (Fig. 5.2) are displayed in Figs. 6.27c-6.27h. The abscissa in all figures is the pitot pressure p_p normalized by the upstream freestream pitot pressure $p_{p\infty}$. The ordinate represents the distance measured from the flat plate surface normalized by the upstream boundary layer thickness δ_0. It should be noted that in general δ_0 is not the appropriate vertical scaling factor for this complex interaction flow field. As suggested by the experimental data

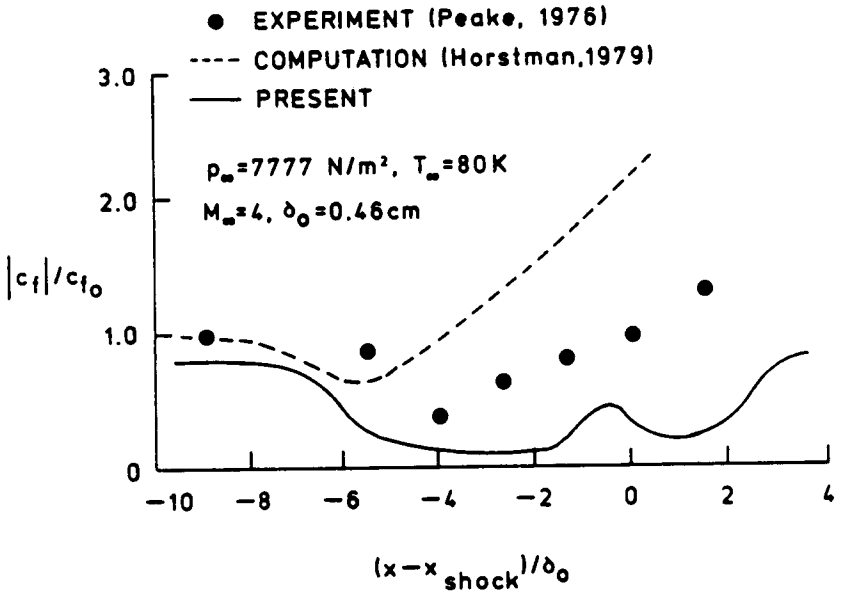

Fig. 6.26 Skin friction distribution on the flat plate along Y/δ_o = 5.56 for 16° sharp fin

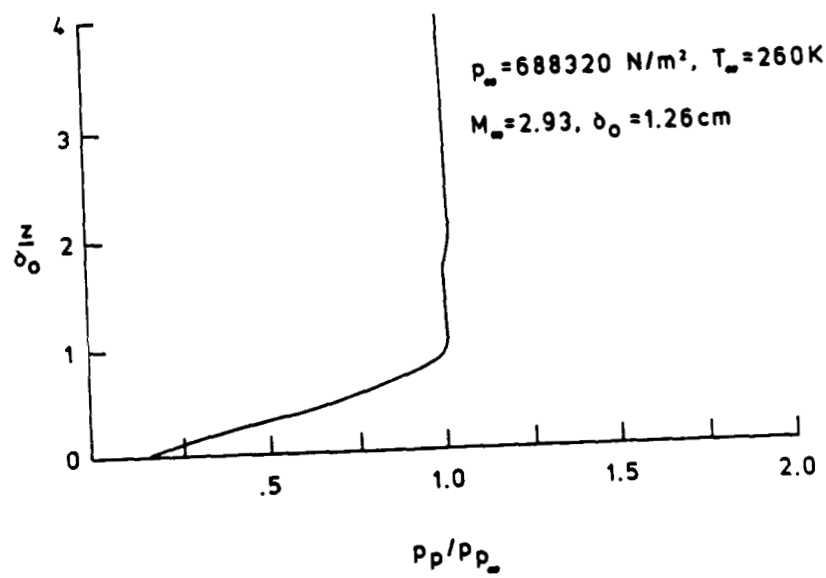

Fig. 6.27 Pitot pressure distribution at different axial locations for 20° sharp fin: (a) station 1

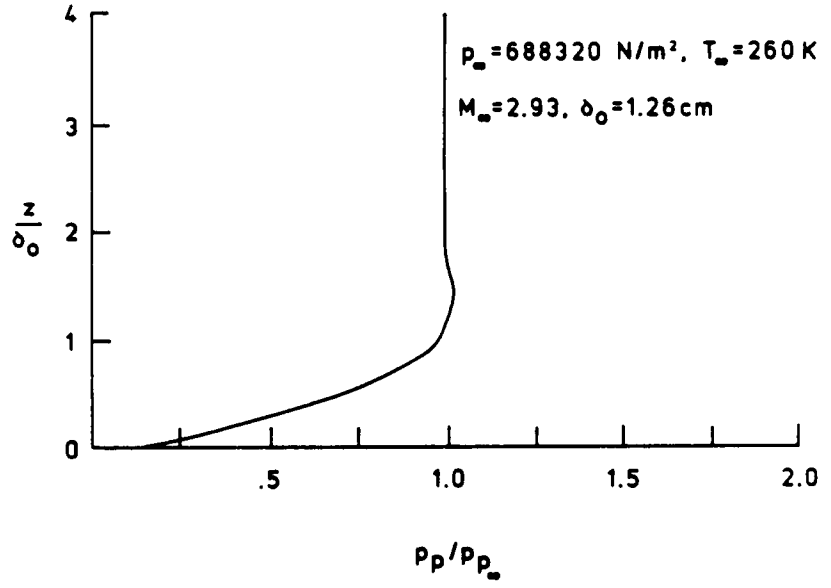

Fig. 6.27(continued) (b) station 2

of McClure and Dolling [58] the appropriate vertical scaling factor is given by $Z\ Re_{\delta_0}^{1/3}/\delta_0$ where δ_0 is the experimentally measured boundary layer thickness immediately upstream of the shock (without the fin effects) at the specified spanwise location. The selection of δ_0 as the appropriate scaling factor was motivated by the desire to clearly demonstrate the vertical extent of the interaction relative to the height of the incoming boundary layer at the location upstream of the fin interaction. Similarly, the profiles are shown at selected streamwise locations x_s/δ_0, where $x_s = x - x_{shock}$ and x_{shock} is the location of the theoretical inviscid shock at a specified spanwise location. It should be noted that the experiments by Settles and Bogdonoff [59], Dolling and Bodgonoff [60], and Lu and Settles [61] indicate that the appropriate scaling is given by $X_s' = X_s\ Re_{\delta_0}^{1/3}/\delta_0$.

Figure 6.27c shows the comparison of computed pitot pressure distribution with the experiment at station 3 which is coincident with the line of coalescence. The results from the previous numerical study are also included. In general the agreement between the present results and the previous experimental and numerical results are quite good. Figure 6.27d shows the comparison of the results at station 4, located approximately one-third of the distance between the line of coalescence and the fin oblique shock wave at the specified spanwise location. The computed and experimental profiles display a modest "overshoot" outside the boundary layer, associated with the compression system ahead of the shock wave. The comparison of computed pressure profiles with experiment along station 5, located at approximately two-thirds of the distance between the line of coalescence and

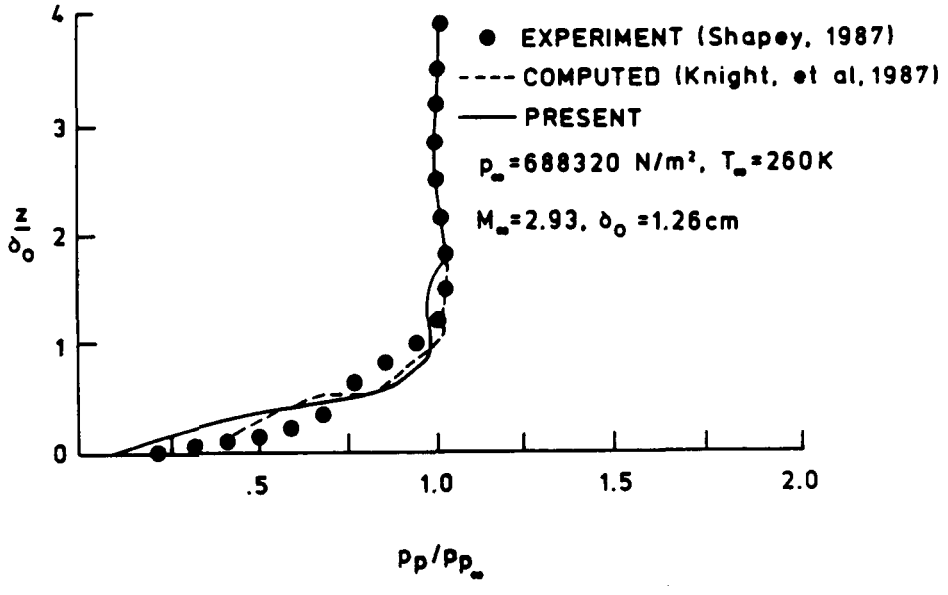

Fig. 6.27(continued) (c) station 3

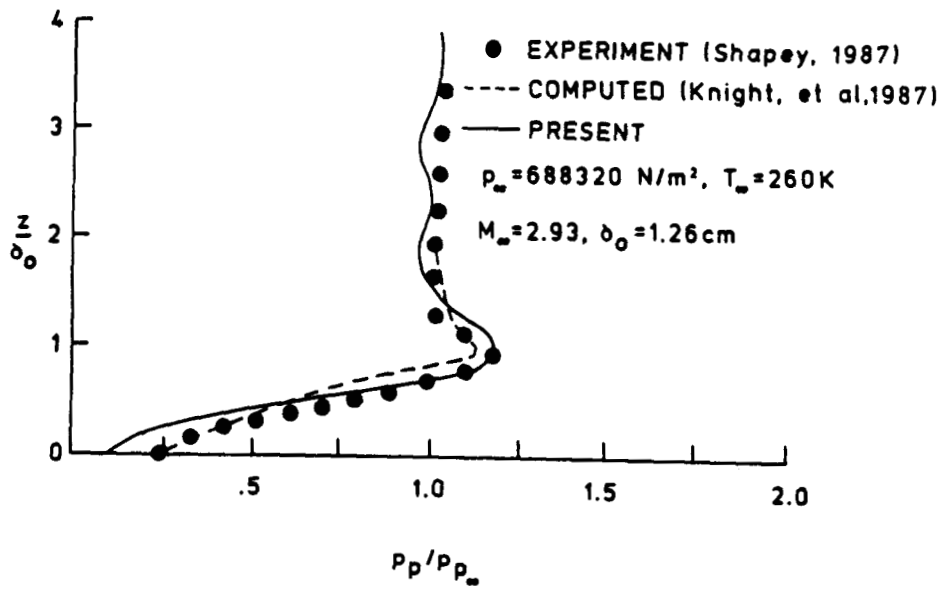

Fig. 6.27(continued) (d) station 4

the inviscid shock wave at the specified spanwise position is given in Fig. 6.27e. The experimental profiles display a slightly S-shaped behavior near the wall, which is less apparent in the computed profiles at this location. The overshoot in the pitot pressure is more pronounced at this location. In both locations, the computed profiles of pitot pressure p_p are in reasonable agreement with the experimental data, and accurately predict the observed overshoot in p_p. However, the pressure profiles are smeared near the location of $Z/\delta = 1.5$ due to the shock capturing nature of the algorithm.

The calculated and experimental pitot pressure profiles at station 6 are shown in Fig. 6.27f. Due to the close proximity of this station to the fin leading edge shock wave, uncertainties in pitot pressure measurements were noticed in the experimental data outside the boundary layer edge. Further improvements in the experimental procedure are needed to resolve this issue. But within the boundary layer, reasonable agreement is obtained between the experimental and the numerical results. The S-shaped nature of the profile is again apparent, with reasonable agreement between the experimental and numerical results. The computed pitot pressure profiles at stations 7 and 8 are compared with experimental data in Figs. 6.27g and 6.27h. The computed results are in reasonable agreement with the experimental data with the discrepancy appearing in the inviscid portion due to the shock capturing nature of the algorithm and the proximity of station 7 to the shock ($X_s = 0.6\ \delta_0$).

On the basis of the success of validation of the present numerical results with the available data, further results were obtained to study the details of the instantaneous and limiting

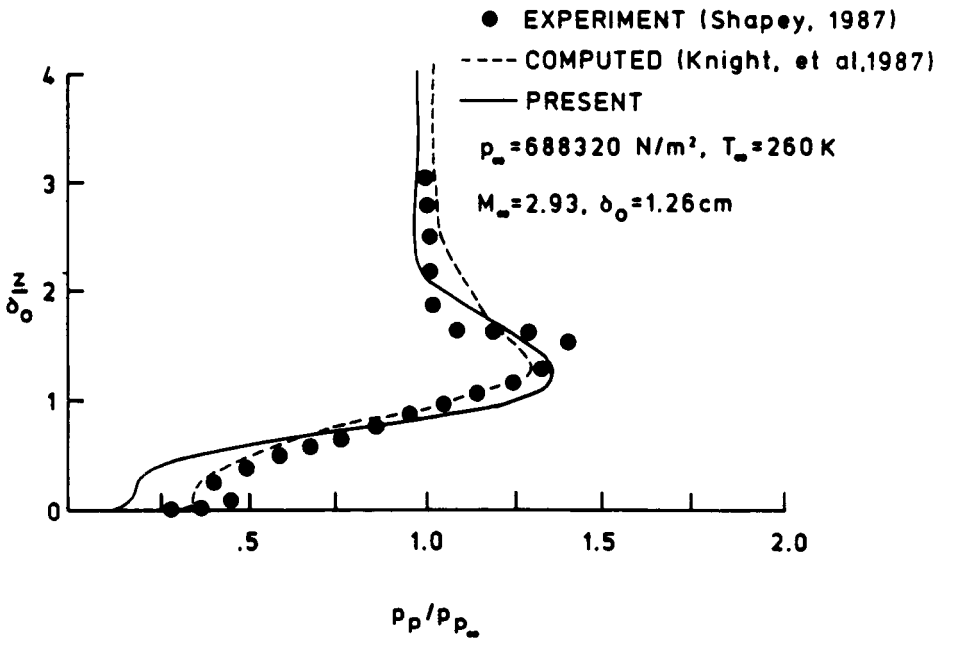

Fig. 6.27(continued) (e) station 5

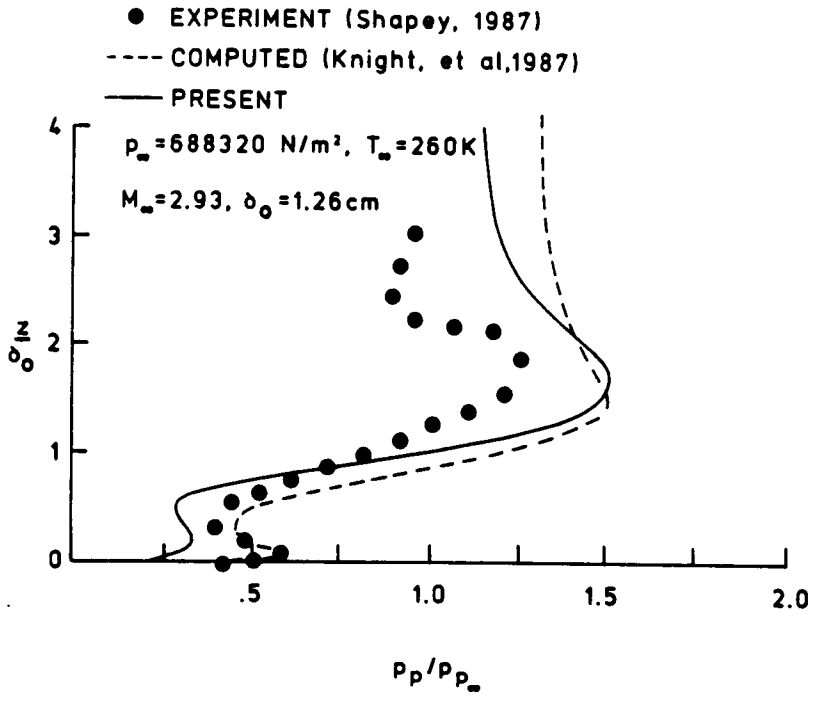

Fig. 6.27(continued) (f) station 6

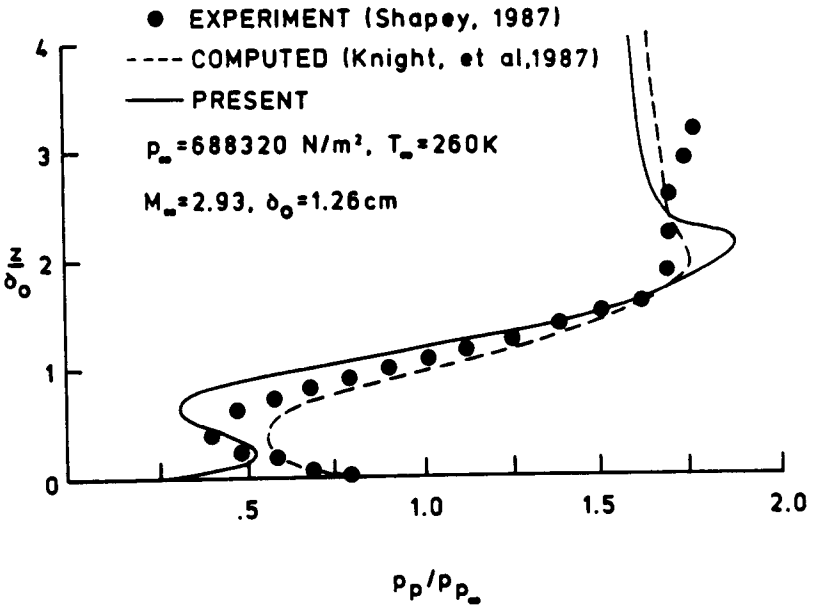

Fig. 6.27(continued) (g) station 7

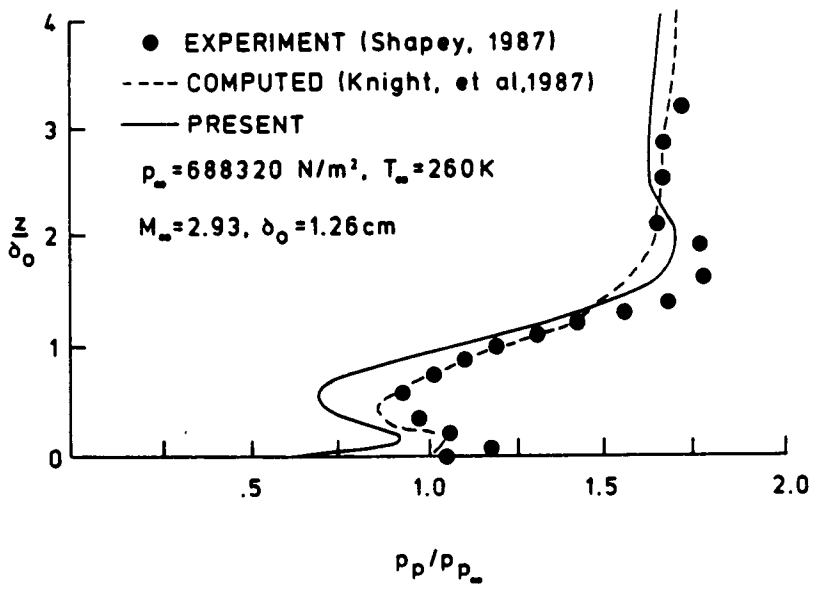

Fig. 6.27(continued) (h) station 8

streamline patterns. The instantaneous and limiting streamlines clearly depict the complex nature of the interaction flow. Figure 6.28 shows the computed limiting streamline patterns obtained using the Baldwin-Lomax turbulence model. The line of coalescence and line of divergence are clearly observed. These specific numerically simulated flow structures are in general agreement with the experimental results using a kerosene lampblack visualization technique. In particular, the experimental line of coalescence at $Y/\delta_0 = 10$ (the approximate spanwise extent of the experimental kerosene lampblack visualization) is $x_s = -5.7\ \delta_0$, whereas the computed lines of coalescence using the Baldwin-Lomax model occur at $X_s = -6.45\ \delta_0$. The computations performed by Knight et al. [57] using the Baldwin-Lomax and Jones-Launder models predict the lines of coalescence at $X_s = -4.5\ \delta_0$ and $-3.5\ \delta_0$, respectively.

A series of calculated mean streamlines are displayed in Fig. 6.29. The vertical scale of the figure has been enlarged for clarity. In Fig. 6.29a, the particle traces of 18 streamlines are shown. Six streamlines originate from the surface, upstream of the interaction, at equal spanwise increments and serve to define the line of coalescence. Six additional streamlines are released immediately above the previous six at a height of $0.0048\ \delta_0$. These latter streamlines clearly cross the line of separation and continue to roll downstream in the clockwise direction (as viewed from the fin leading edge). Another set of streamlines is released at a height of $0.52\ \delta_0$ from the plate surface. These particles clearly display a counter clockwise rotational motion of the fluid particles. The streamlines clearly display a vortical structure. It is interesting to see that the

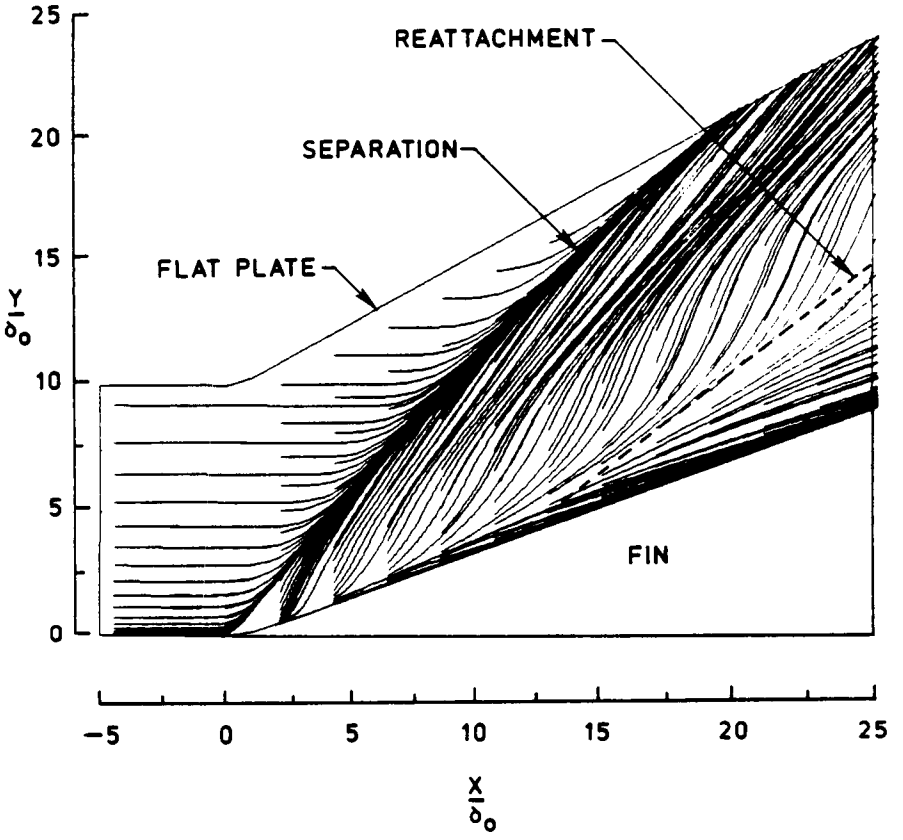

Fig. 6.28 Limiting streamline patterns on the plate surface for 20° sharp fin

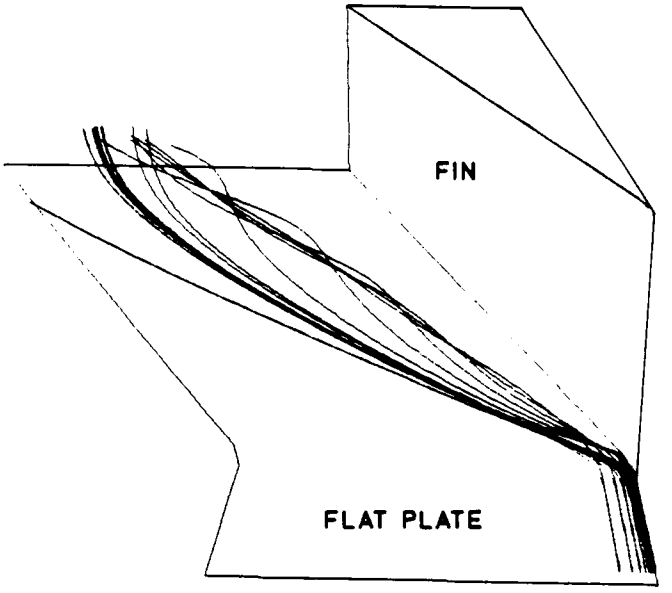

Fig. 6.29 Mean streamlines for 20° sharp fin: (a) originating at Z/δ_o = 0, 0.0048 and 0.52

particles originating from the higher z-locations are swept beneath the particles originating near the surface. Another set of additional streamlines originating upstream at a height of $Z/\delta = 1.1$ are shown in Fig. 6.29b. Unlike the particles originating at lower values of z, these particles move approximately parallel to the surface. Also, the streamlines in this case exhibit considerable rotation within the boundary layer as compared to the case of the 16° sharp fin, due to the strong nature of the interaction. Figure 6.30 shows the computed limiting streamlines on the fin surface. This again depicts the existence of separation on the fin surface. Figure 6.31 shows the computed velocity magnitude contours on the flat plate. The simulated flow features such as separation shock, fin shock, and reattachment shock are clearly evident.

6.4 Turbulent Flow Past a Swept Blunt Fin

For the case of the swept fin induced shock wave/boundary layer interaction, comparative results were obtained for the specific conditions of Sec. 5.4. The computations were carried out using a 40 x 45 x 45 mesh. The pressure distribution along the fin stagnation line are compared in Fig. 6.32 for various fin sweep angles. The pressure is nondimensionalized by the total pitot pressure behind the bow shock, p_{t2}. The agreement between the numerical results and the experimental data is seen to be good except for the zero sweep blunt fin where the level of pressure is underpredicted in the boundary layer and overpredicted in the inviscid region. The experimental measurements [17] indicated that

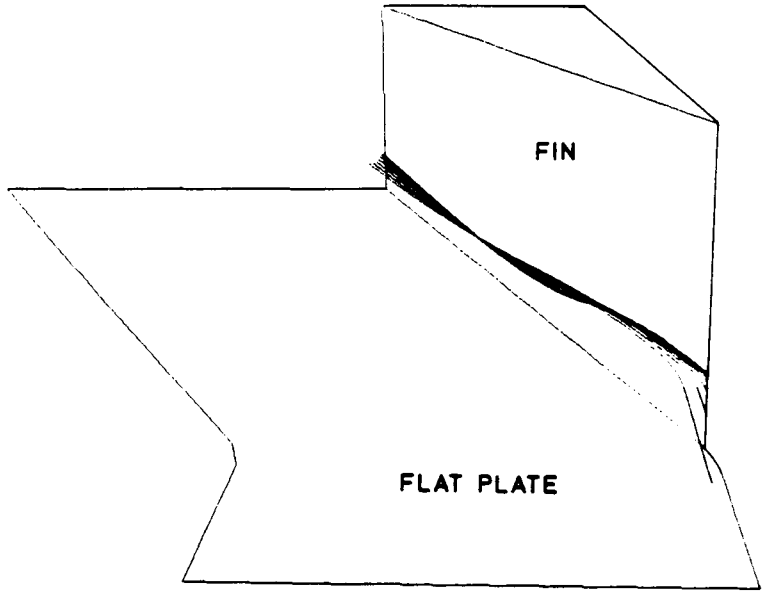

Fig. 6.29(continued) (b) originating at $Z/\delta_o = 1.1$

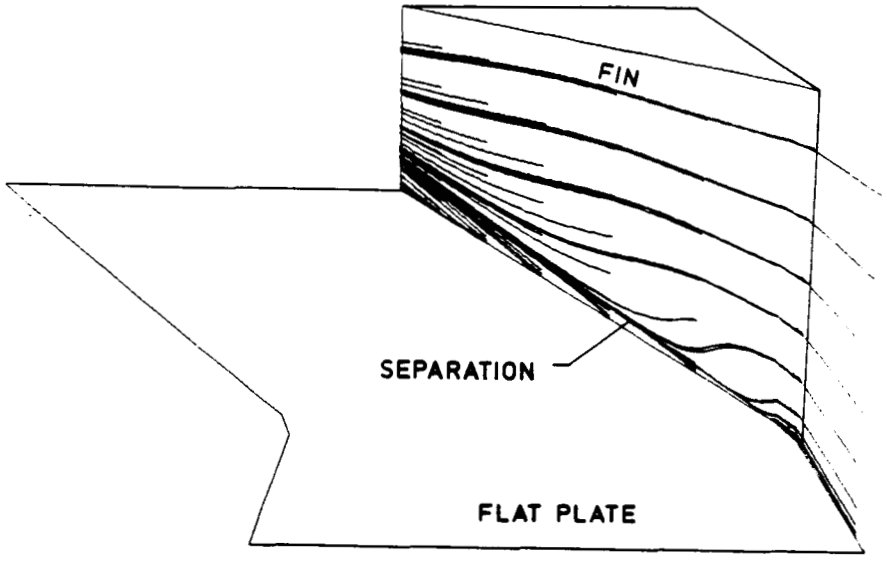

Fig. 6.30 Limiting streamline patterns on the fin surface for 20° sharp fin

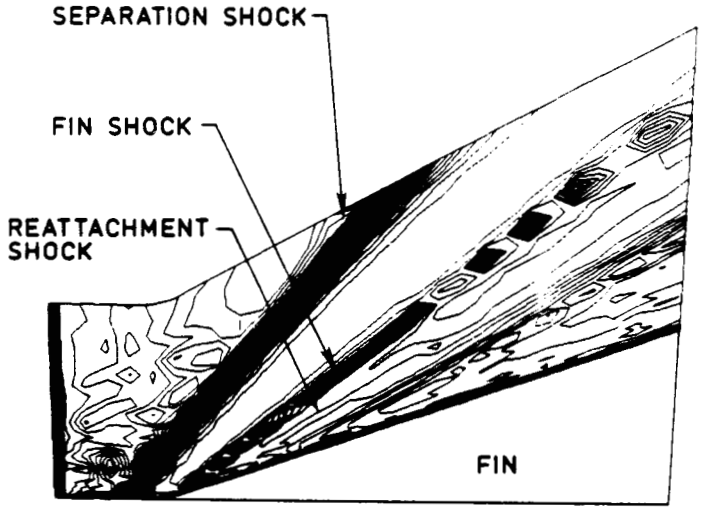

Fig. 6.31 Velocity magnitude contours on the plate surface for 20° sharp fin

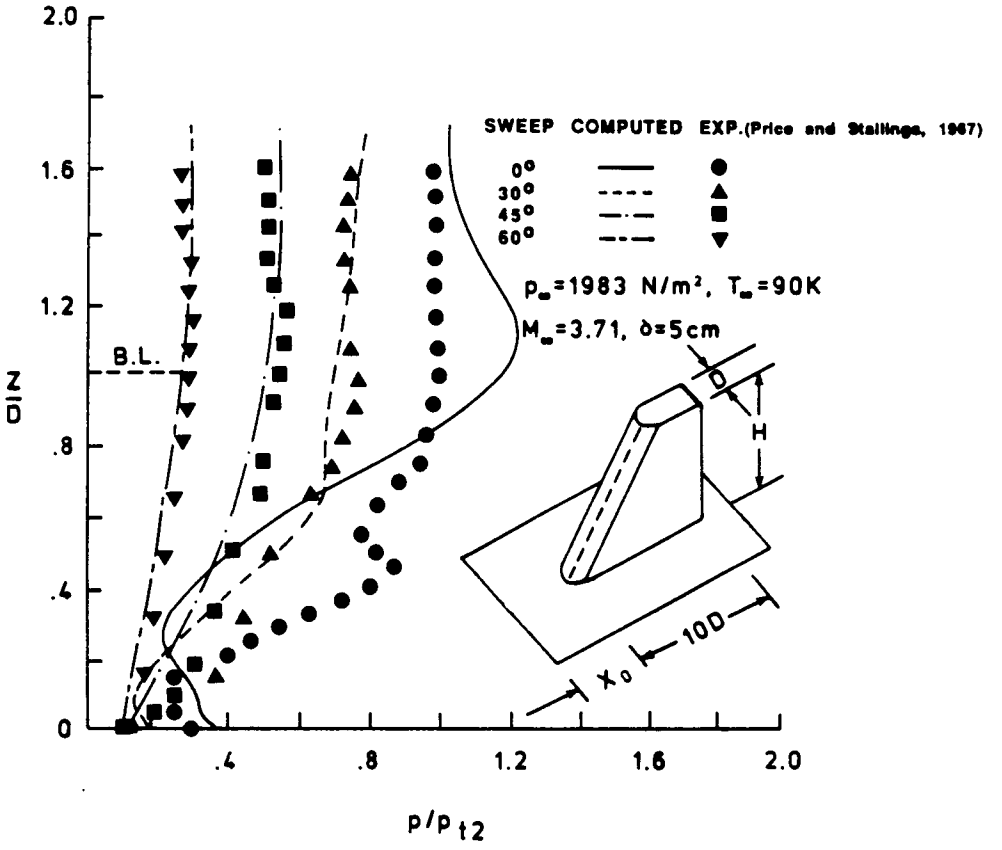

Fig. 6.32 Comparison of pressure distribution along the fin stagnation line for various fin sweeps

> "an irregular pressure distribution does in fact occur and the location of peak pressure within the boundary layer is a function of sweep as well as Mach number. Lack of data in the region near the wall prevents identifying a peak for any of the other models with this diameter. A more complete experimental investigation would have to be performed to define, for a certainty, the flow model responsible for this irregular pressure distribution."

A close examination of the figure reveals that as the fin sweep from the angle increases, the magnitude of the peak pressure decreases considerably from 1.2 to 0.2. The variation in pressure from the position of peak to minimum is substantially reduced by increasing fin sweeps. The increase in pressure in the direction toward the plate surface from the position of minimum is not seen for fin sweep angles greater than 30°. The computed temperature distribution along the fin stagnation line (Fig. 6.33) also shows some improvements due to the sweep.

The comparison of pressure distribution on the flat plate along the line of symmetry (Y/D = 0) and off the line of symmetry (Y/D = 1.5 to 4.5) are illustrated in Fig. 6.34. Again the agreement is seen to be very good. The code is able to simulate all the pertinent flow features such as upstream influence, pressure rise due to flow separation from the flat plate, pressure plateau and double peaks in pressure off the line of symmetry. Further examination of the results reveal a low pressure region between the pressure plateau and the

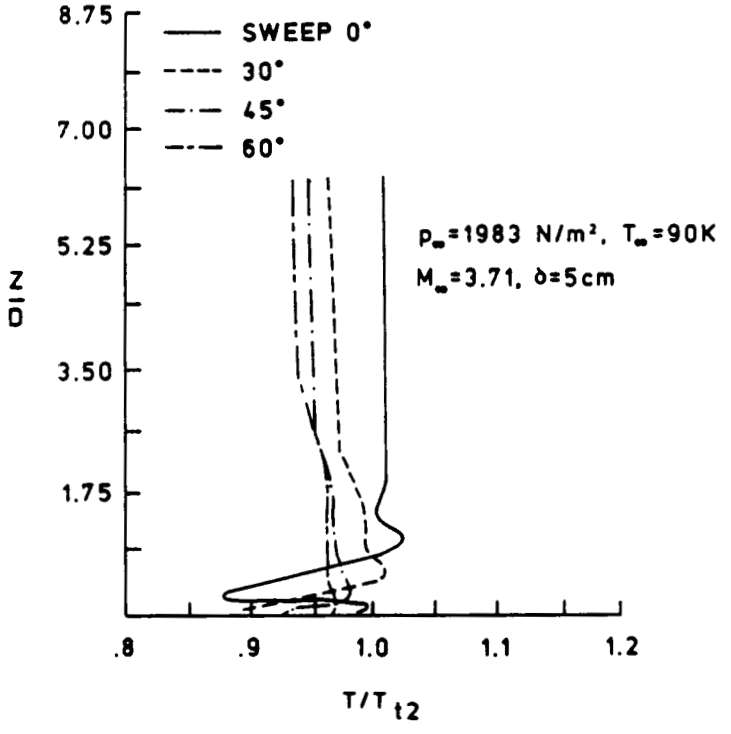

Fig. 6.33 Temperature distribution along the fin stagnation line for various fin sweeps

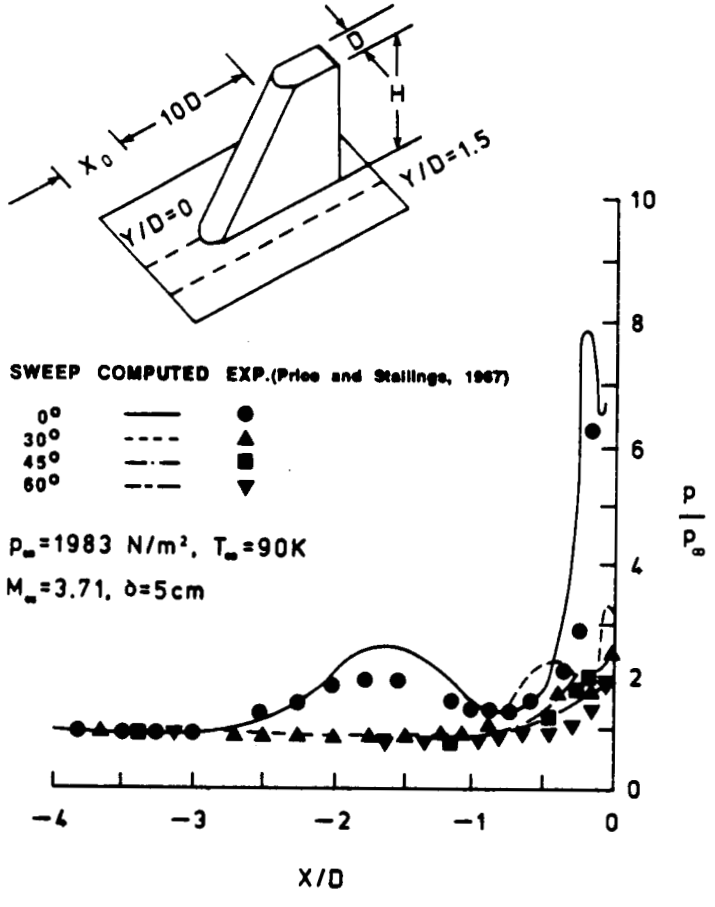

Fig. 6.34 Comparison of pressure distribution on the flat plate for various fin sweeps: (a) along Y/D = 0

final compression along the line of symmetry (Fig. 6.34a). The low pressure observed is due to the existence of the reversed high speed flow region. However, for sweep angles greater than 30° the low pressure region is not seen. The disappearance of the low pressure trough region for high fin sweep angles demonstrates the weakening of the main horseshoe vortex with the sweep. Further examination of the results illustrates that the sweep considerably decreases the upstream influence. The appearance of double peaks in pressure (Figs. 6.34b-6.34e) on the flat plate is due to the primary horseshoe vortex moving downstream in a helical fashion. The low pressure region between the two pressure peaks is caused by a high velocity under the core of the vortex [31]. It is seen that the sweep decreases the spanwise extent of the interaction considerably. This is due to diminishing of the double pressure peaks for higher sweeps. Some of the trends exhibited in Fig. 6.34 will become apparent after discussions of the flow structure. The computed surface temperature distribution along the line of symmetry is shown in Fig. 6.35. The improvement in the surface temperature is clearly apparent.

The computed particle paths in the plane of symmetry are shown in Fig. 6.36 for blunt and 60° swept fins. The results clearly show the flow separation on the flat plate ahead of the fin, leading to the formation of the primary horseshoe vortex (Fig. 6.36a). A small secondary vortex is also seen near the juncture formed by the fin and flat plate (Figs. 6.36a and 6.36b). The secondary vortex rotates in a counterclockwise direction as compared with the primary horseshoe vortex. The primary vortex elongates to a length of two diameters ahead of the blunt fin with its core located about 0.2 diameters above

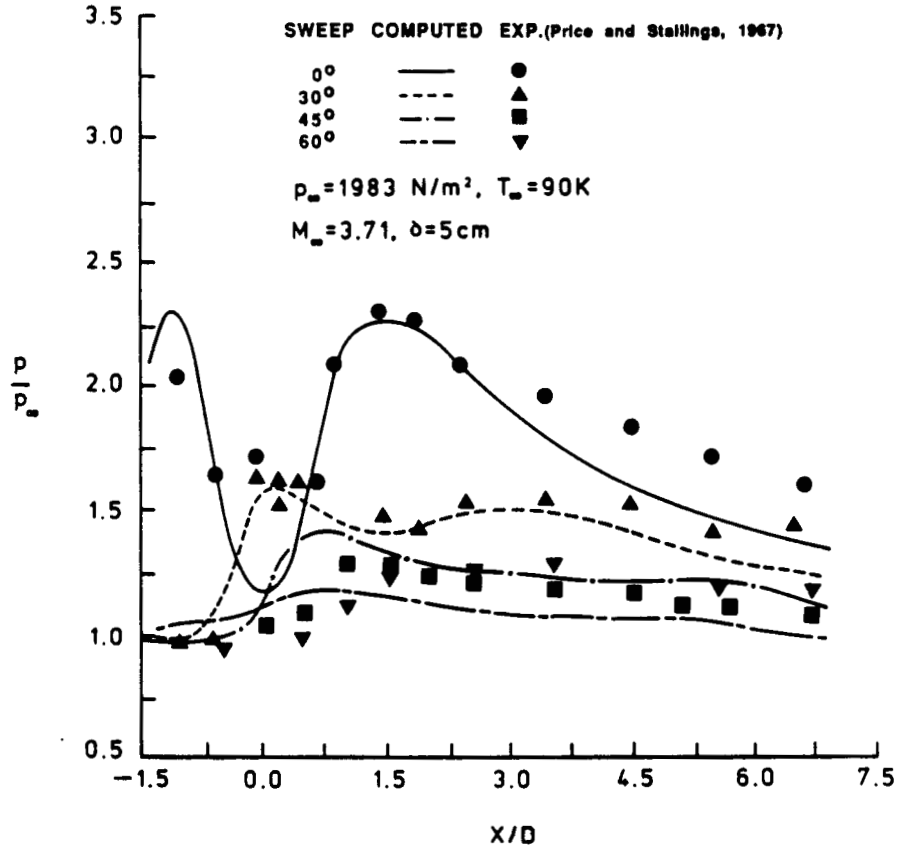

Fig. 6.34(continued) (b) along Y/D = 1.5

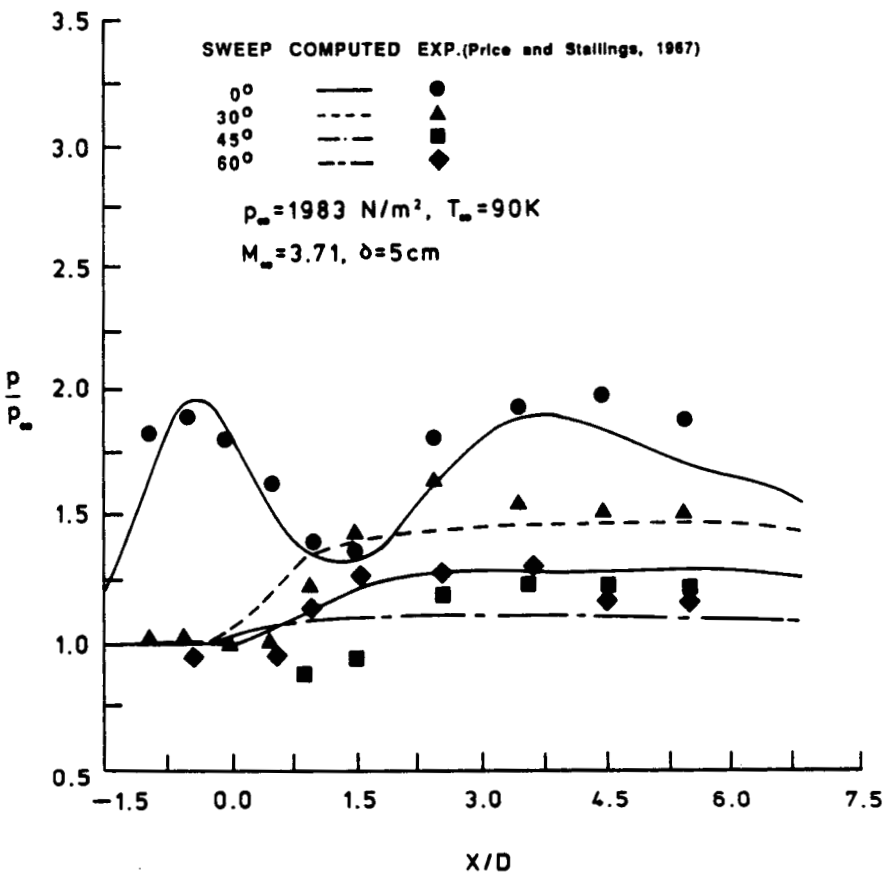

Fig. 6.34(continued) (c) along Y/D = 2.5

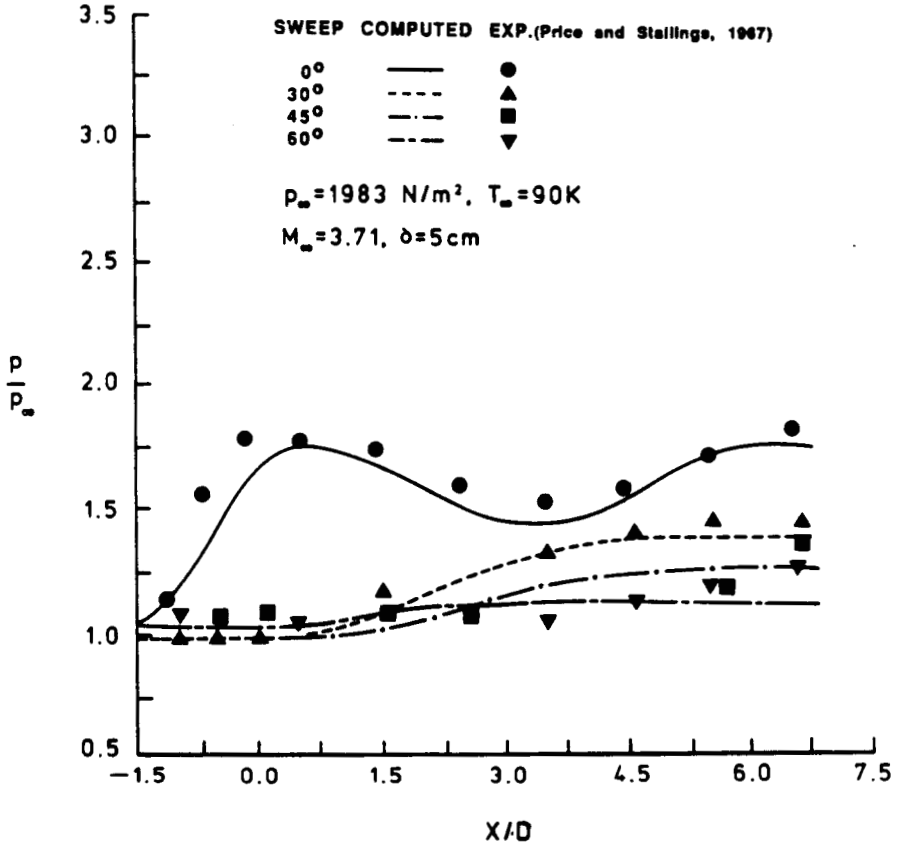

Fig. 6.34(continued) (d) along Y/D = 3.5

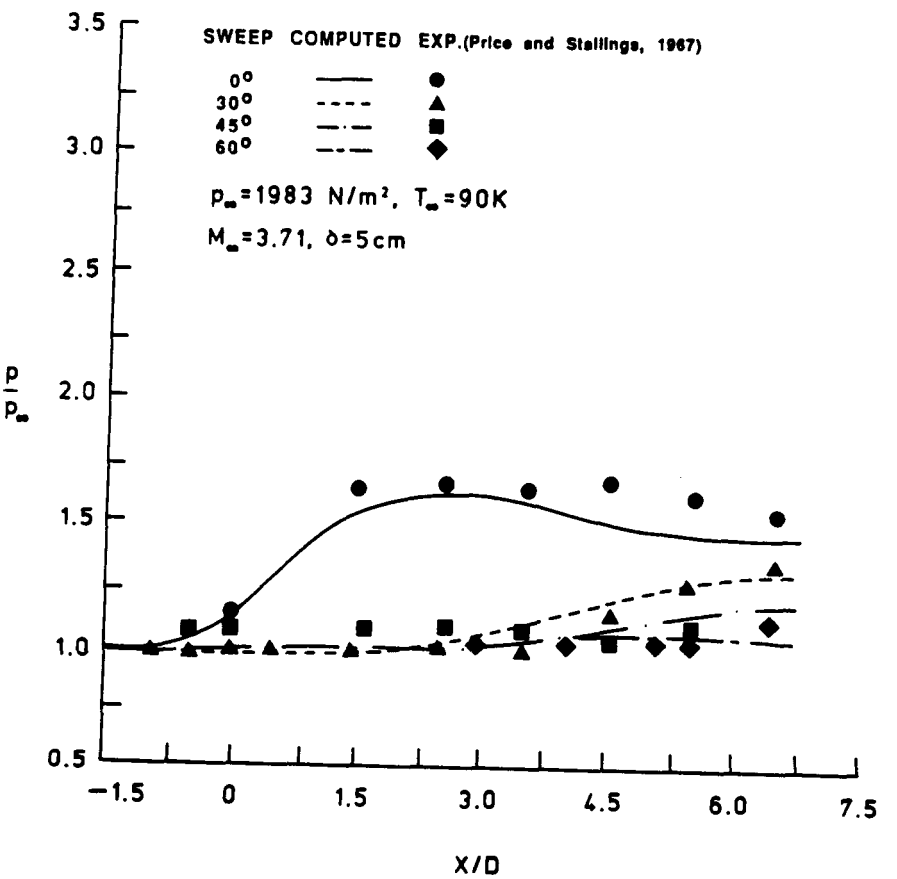

Fig. 6.34(continued) (e) along Y/D = 4.5

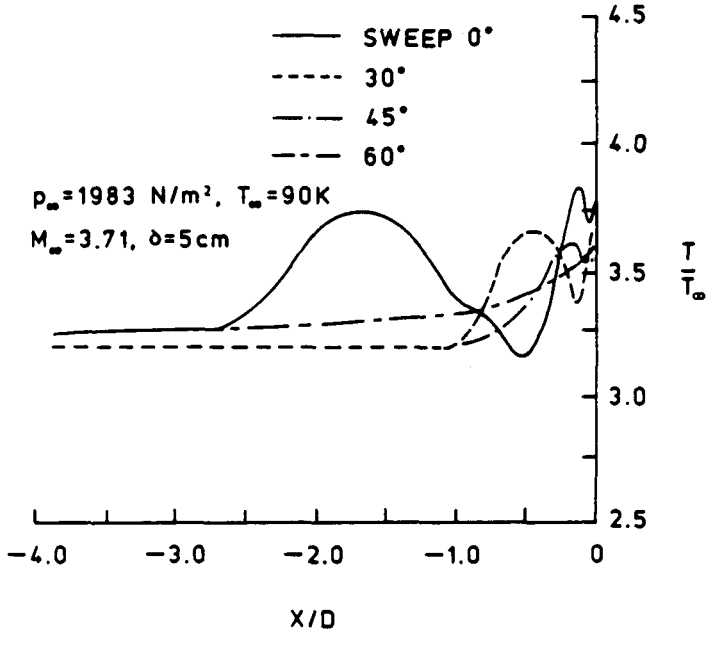

Fig. 6.35 Temperature distribution along the line of symmetry for various fin sweeps

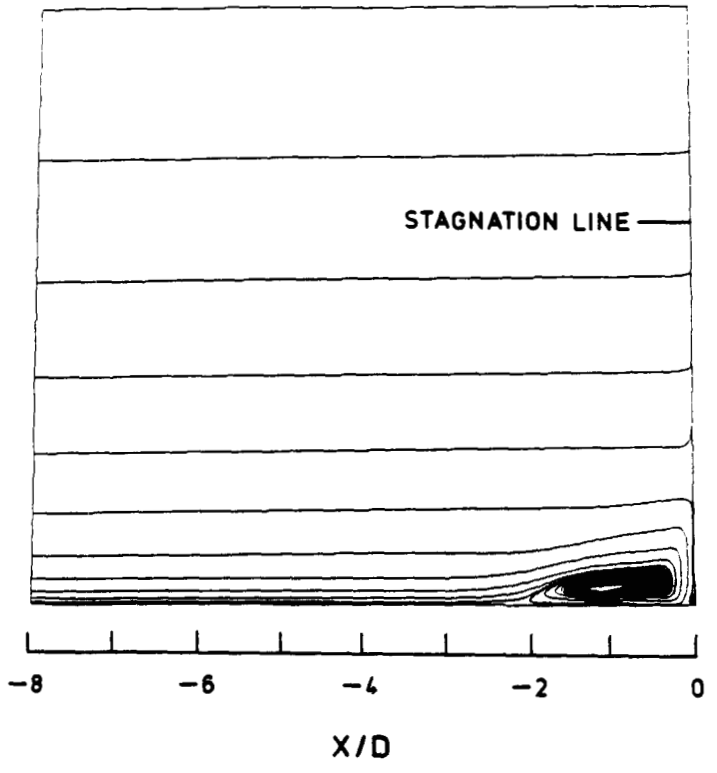

Fig. 6.36 Particle paths in the plane of symmetry for various fin sweeps: (a) sweep = 0°

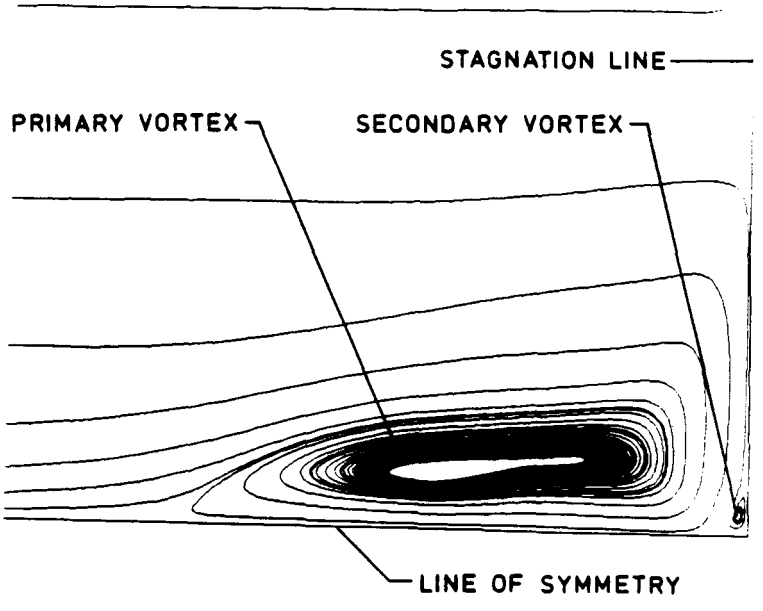

Fig. 6.36(continued) (b) enlarged view of the flow at the junction for sweep = 0°

the flat plate. As the fin sweep is increased to 60°, the extent of the separation on the flat plate is reduced considerably (Fig. 6.36c and Fig. 6.37). This leads to the weakening of the horseshoe vortex (Fig. 6.36c).

The computed skin friction distribution along the line of symmetry is illustrated in Fig. 6.37 for various fin sweeps. It is seen that with an increase in the fin sweep, the upstream separation point (where C_f value changes sign) moves closer to the fin leading edge. Also, for fin sweep angles greater than 0°, no definite reattachment point (where the C_f value starts increasing from a negative value) is observed.

The horseshoe vortex transports fresh high momentum fluid continuously into the separated flow region (Fig. 6.36a). As this high momentum fluid accelerates and moves away from the plane of symmetry, it leads to the formation of two reversed supersonic zones [31, 62, 63], one on the fin and the other on the flat plate. The decrease in pressure from the peak to a minimum observed in Fig. 6.32 is not only due to a lower stagnation pressure in the incoming boundary layer profile, but also due to the extreme expansion caused by the horseshoe vortex. This expansion leads to the formation of a reversed supersonic zone on the fin. From the computed particle paths in the plane of symmetry for the blunt fin (Fig. 6.36a), it is seen that the streamlines of low momentum fluid never impinge directly on the fin surface. They spiral into the horseshoe vortex and continue to roll up downstream in the form of a necklace vortex. The increase in pressure in the direction toward the plate surface observed in Fig. 6.32 is due to recompression of the flow from supersonic to subsonic speed.

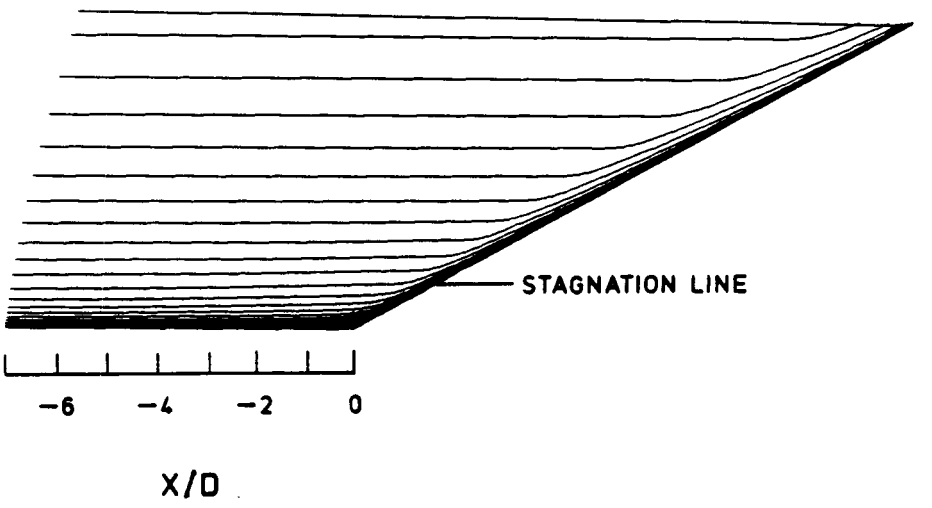

Fig. 6.36(continued) (c) sweep = 60°

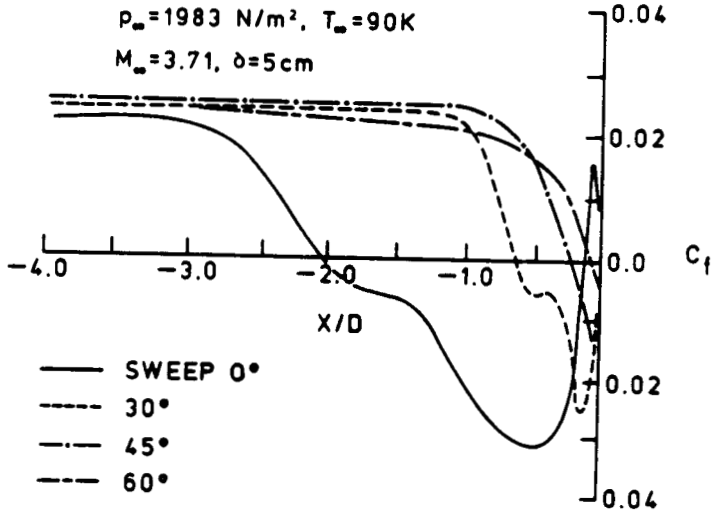

Fig. 6.37 Skin friction distribution along the line of symmetry for various sweeps

It is this adverse pressure gradient that leads to the formation of the secondary vortex at the corner (Fig. 6.36b). As the fin sweep angle increases, the variation in pressure is reduced substantially. This weakens the horseshoe vortex which leads to the disappearance of the supersonic zones [62, 63].

The computed limiting streamline patterns are shown in Fig. 6.38 for blunt, 30° and 60° swept fins. The separation and reattachment lines are also marked in the figure. The foot trace left by the horseshoe vortex as the flow goes around the fin is clearly observed in the area bounded by the separation and reattachment line. It is apparent that the spanwise influence exerted by the horseshoe vortex on the juncture flow is reduced considerably for high sweep angles. In particular at a sweep angle of $\Lambda = 60°$, the flow beyond the spanwise location, Y/D = 3.0 (Fig. 6.38c) is unaffected by the juncture effect. However, in the case of the blunt fin ($\Lambda = 0°$), the extent of the disturbed flow persists up to Y/D = 6.0 (Fig. 6.38a).

6.5 Turbulent Flow Past a Filleted Fin

For the case of the filleted fin induced shock wave/boundary layer interaction, comparative results were obtained for the specific conditions given in Sec. 5.5. The computations were carried out using a 40 x 45 x 45 mesh. The pressure distribution along the fin stagnation line is compared in Fig. 6.39 for unmodified (blunt fin) and modified (filleted) junctions. The fin surface pressure is again nondimensionalized by the total pitot pressure behind the bow shock ($p_\infty = 0.12\ p_{t2}$). The location of the peak pressure corresponds to the point of impingement of the stagnation streamline on the fin leading

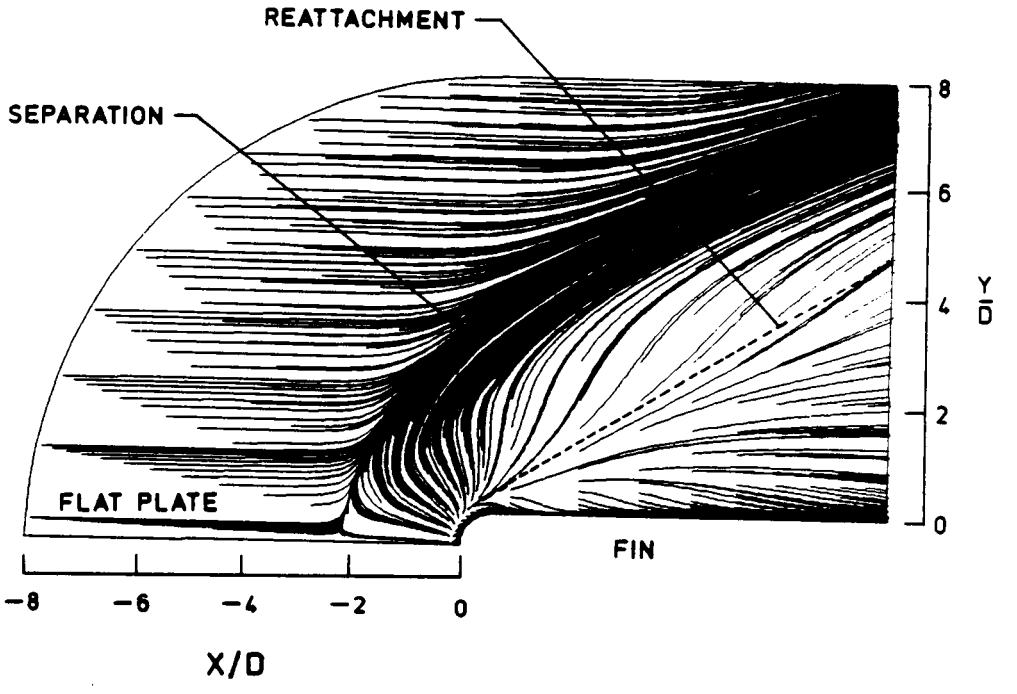

Fig. 6.38 Limiting streamline patterns on the flat plate for various fin sweeps: (a) sweep = 0°

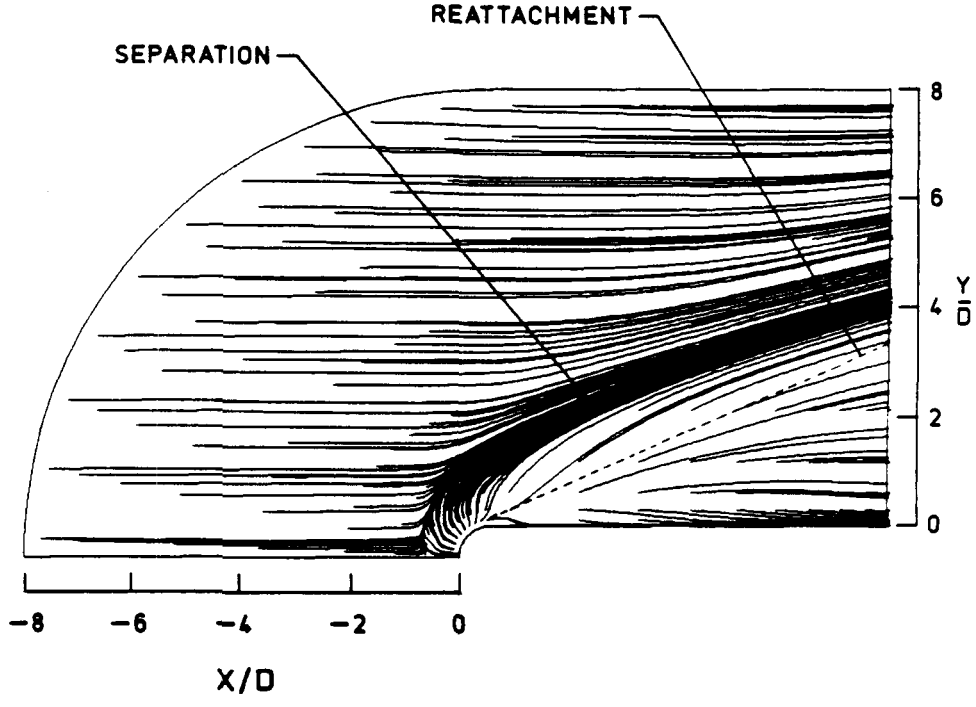

Fig. 6.38(continued) (b) sweep = 30°

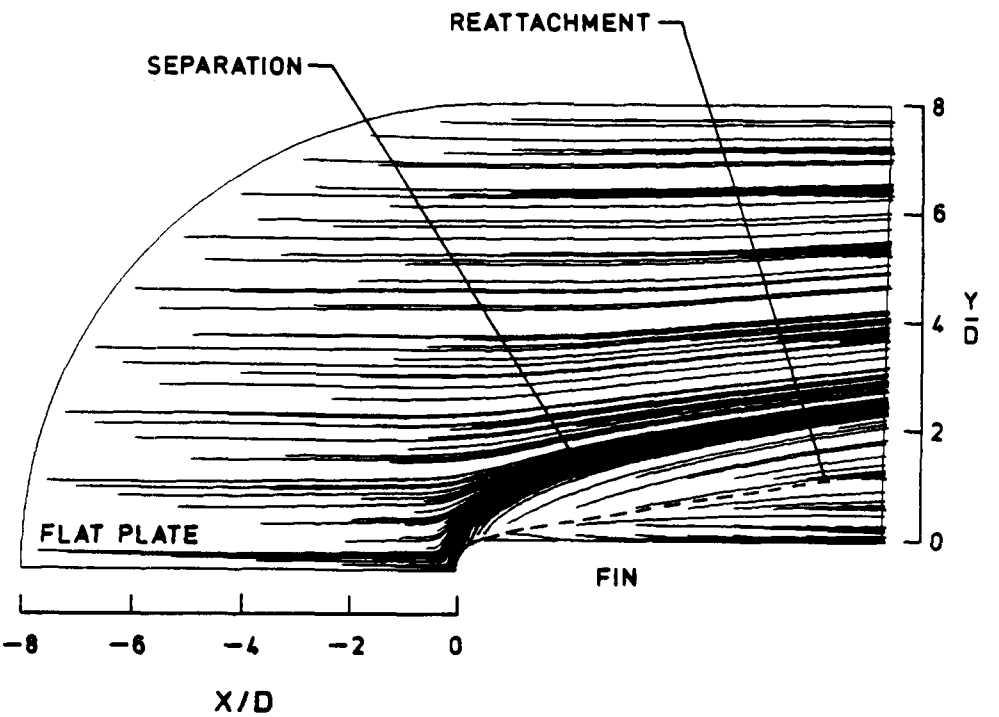

Fig. 6.38(continued) (c) sweep = 60°

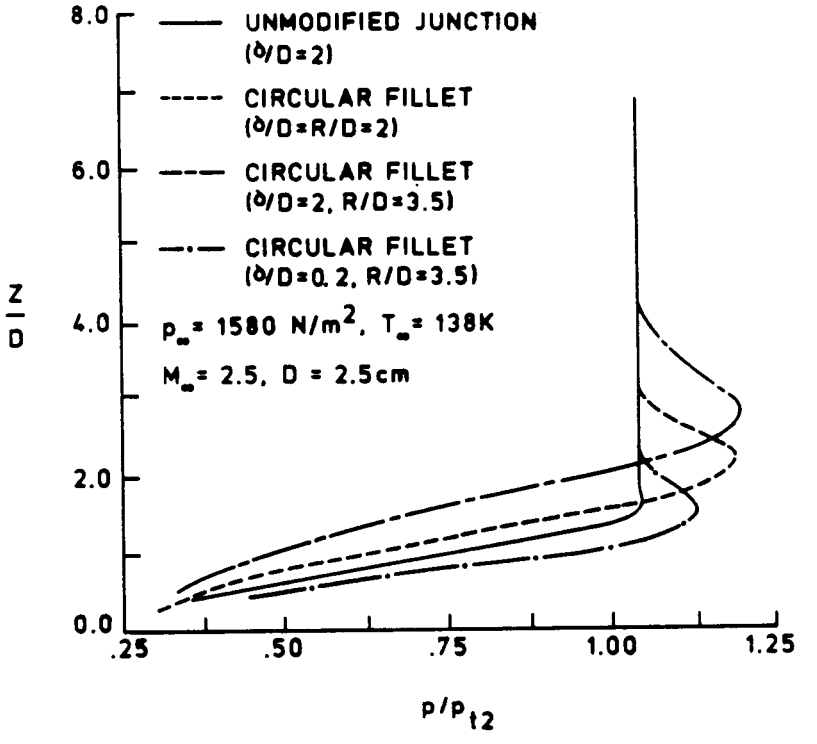

Fig. 6.39 Pressure distribution on the fin leading edge for various junctions

edge. It is seen that the location of the peak pressure on the fin leading edge moves upward for the filleted junction. This is because the flow approaching the junction is deflected upward instead of being rolled into the horsehose vortex. For the case of the small boundary-layer thickness ($\delta/D = 0.2$), the results illustrate a considerable increase in fin leading edge pressure distribution as compared to the unmodified junction. Similar trend in results were observed in blunt fin/flat plate studies [31] in which decreasing the incoming boundary layer thickness by a factor of five showed a considerable increase in the pressure distribution on the fin leading edge.

The pressure distribution along the line of symmetry are compared in Fig. 6.40 for various types of junctions. It is seen that the pressure drop, following the pressure plateau, decreases as the fillet size increases. This indicates a reduction in speed of the reversed flow region and overall acceleration of the juncture flow.

The computed particle paths in the plane of symmetry are shown in Fig. 6.41 for unmodified and modified junctions. The influence of filleting on the flow structure is dramatic as compared to unmodified junction. The particle paths demonstrate that the horseshoe vortex deforms and the flow streamlines within the boundary layer lose much of their vortical character with proper filleting. In another study [32], in which the leading edge shape was changed from a blunt to a square fin, the results showed a considerable increase in the separation length. This resulted in a bifurcation of the main horseshoe vortex into two vortices rotating in the same direction. For the present case, the main horseshoe vortex does not bifurcate even though the bluntness of the leading edge is changed by filleting. The

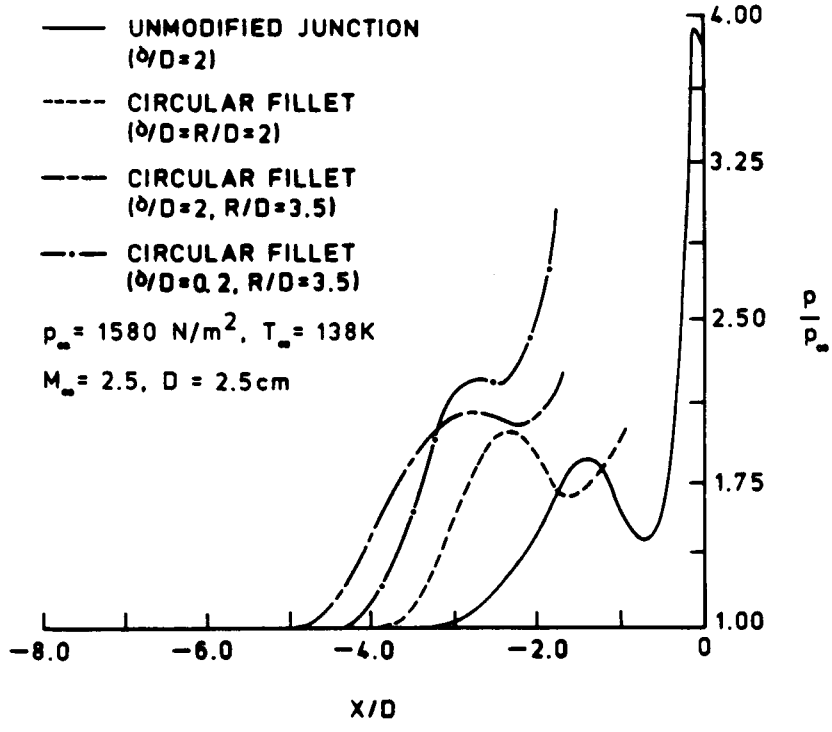

Fig. 6.40 Pressure distribution on the flat plate for various junctions

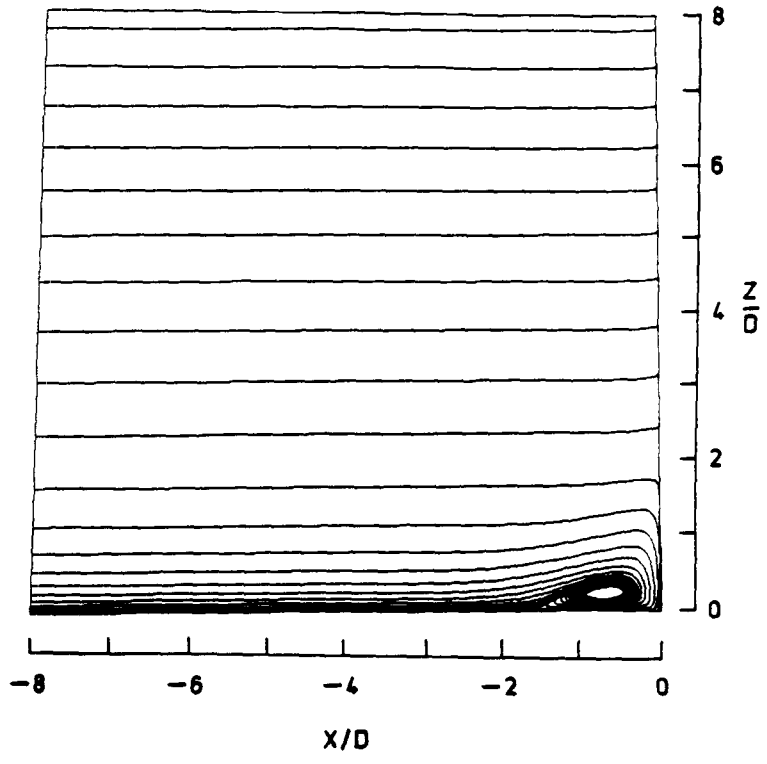

Fig. 6.41 Particle paths in the plane of symmetry for various junctions: (a) unmodified junction ($\delta/D = 2$)

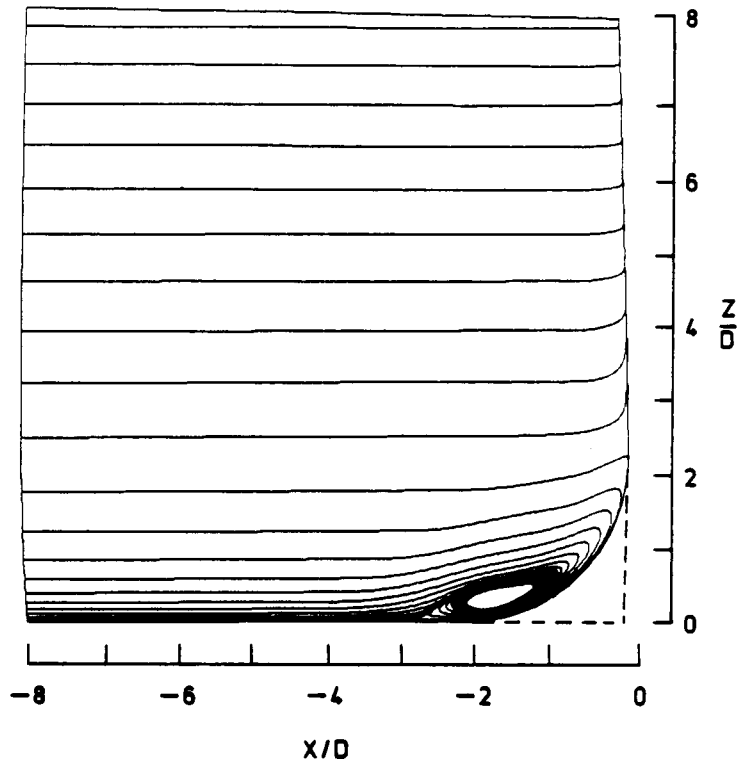

Fig. 6.41(continued) (b) circular fillet ($\delta/D = 2$, $R/D = 2$)

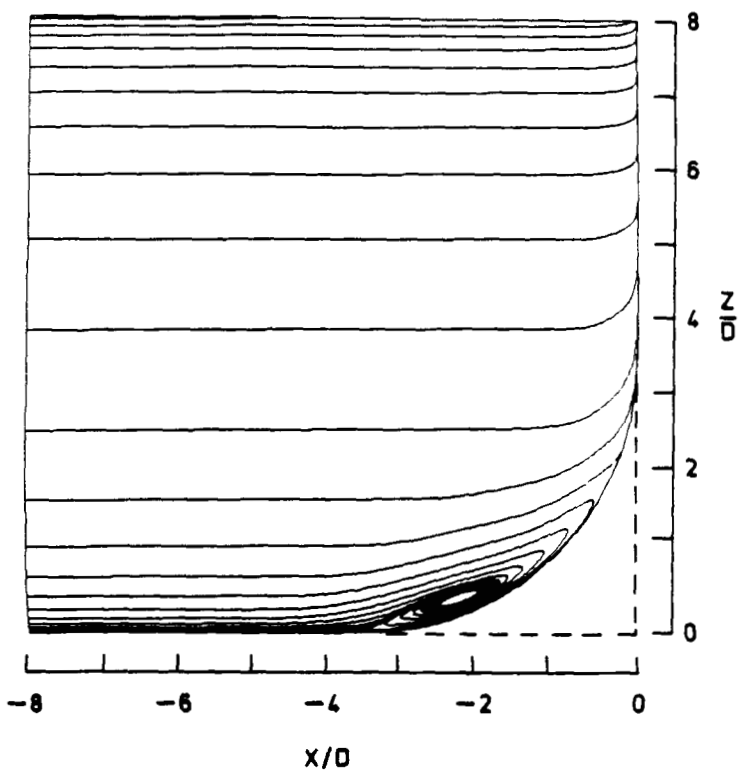

Fig. 6.41(continued) (c) circular fillet ($\delta/D = 2$, $R/D = 3.5$)

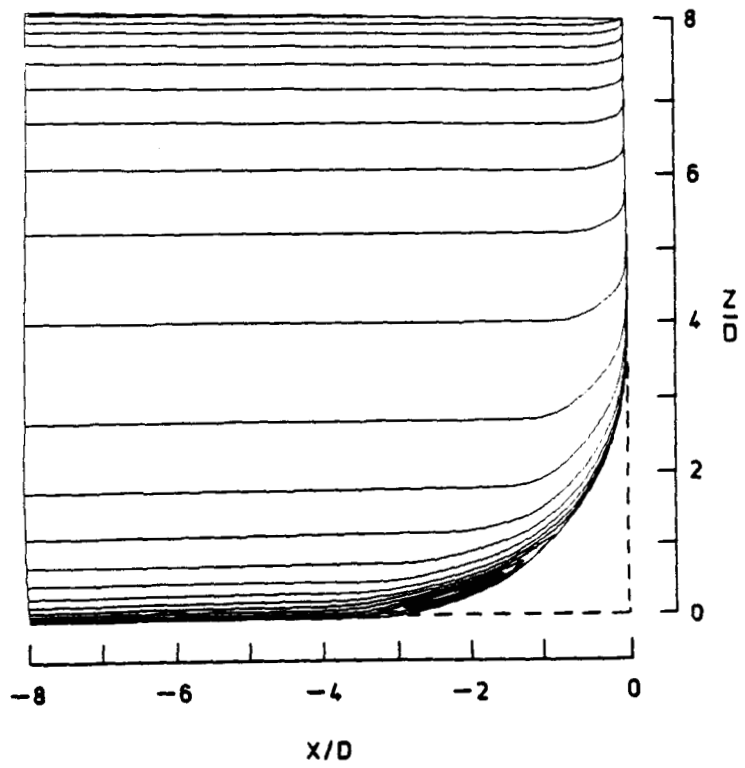

Fig. 6.41(continued) (d) circular fillet (δ/D = 0.2, R/D = 3.5)

surface limiting streamlines are shown in Fig. 6.42 for unmodified and modified junctions. It is apparent that the separation on the fin surface is prevented completely in the case of the modified junction as compared to the unmodified junction. The computed instantaneous streamlines are shown in Fig. 6.43 for unmodified and modified junctions employing circular and continuous fillets. These results show the influence of fillets on the helical vortex structure. The computed velocity magnitude contours (Fig. 6.44) clearly show that with filleting the supersonic zones observed in the case of the blunt fin/flat plate junction weaken as the fillet size is increased at the juncture. The vorticity contours (Fig. 6.45) demonstrate that the magnitude of vorticity in the vortex is reduced by a factor of three in the case of the modified junction as compared to the unmodified junction.

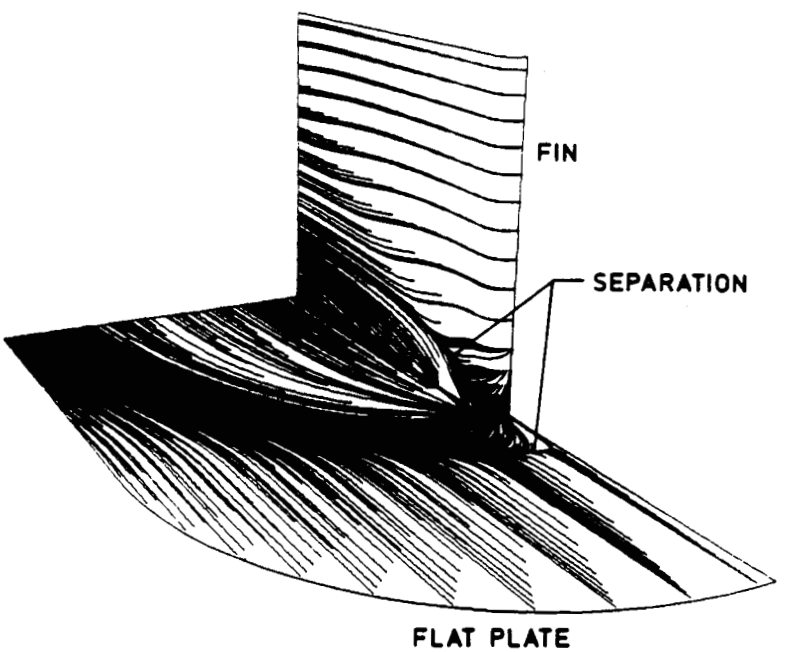

Fig. 6.42 Surface limiting streamlines for various junctions: (a) unmodified junction ($\delta/D = 2$)

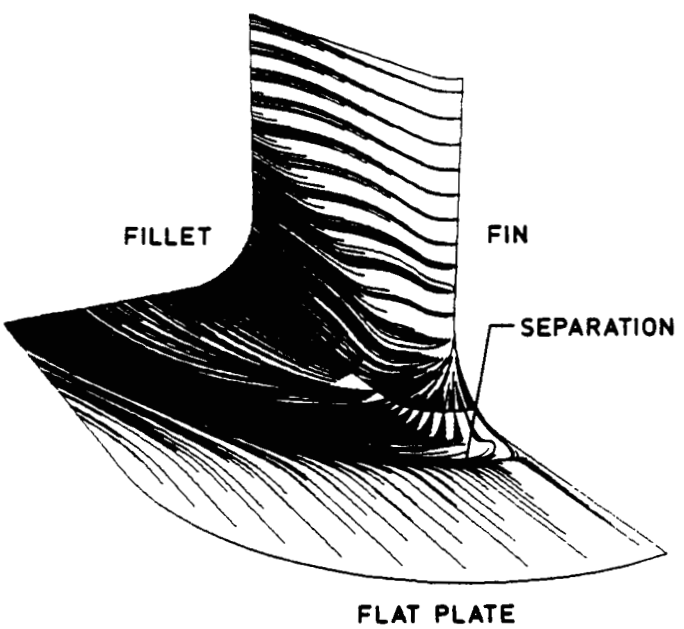

Fig. 6.42(continued) (b) circular fillet ($\delta/D = 2$, $R/D = 2$)

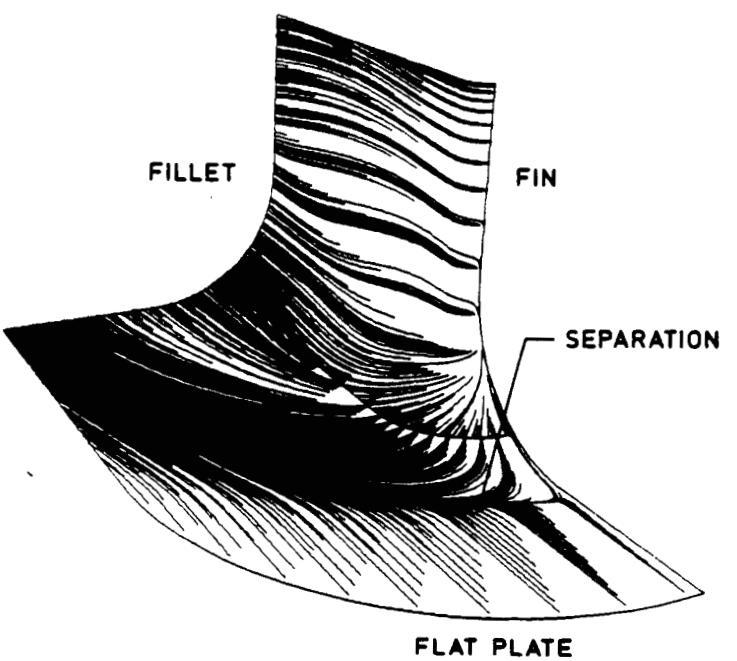

Fig. 6.42(continued) (c) circular fillet ($\delta/D = 2$, $R/D = 3.5$)

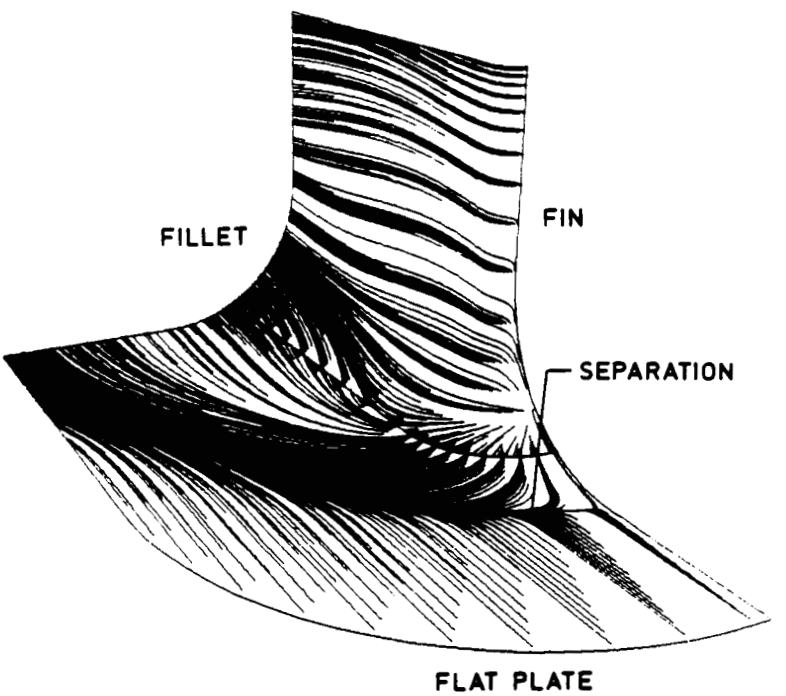

Fig. 6.42(continued) (d) circular fillet ($\delta/D = 0.2$, $R/D = 3.5$)

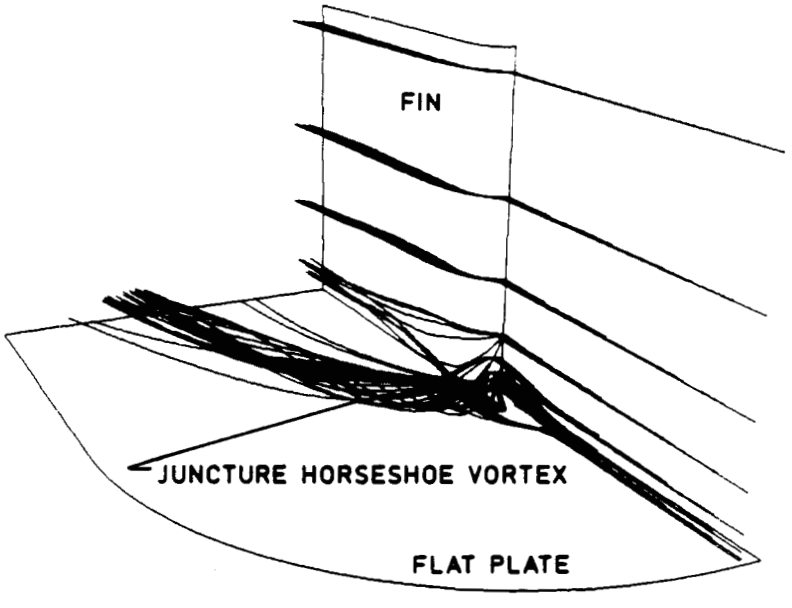

Fig. 6.43 Instantaneous streamlines for various junctions: (a) unmodified junction ($\delta/D = 2$)

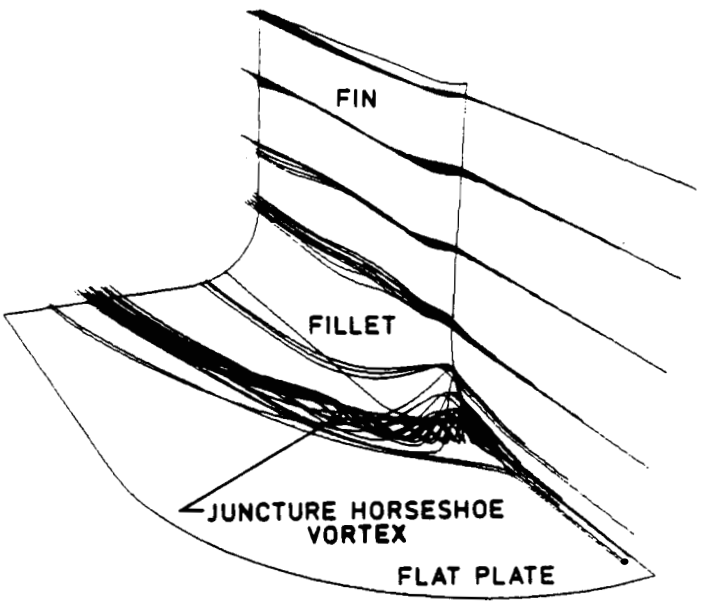

Fig. 6.43(continued) (b) circular fillet ($\delta/D = 2$, $R/D = 2$)

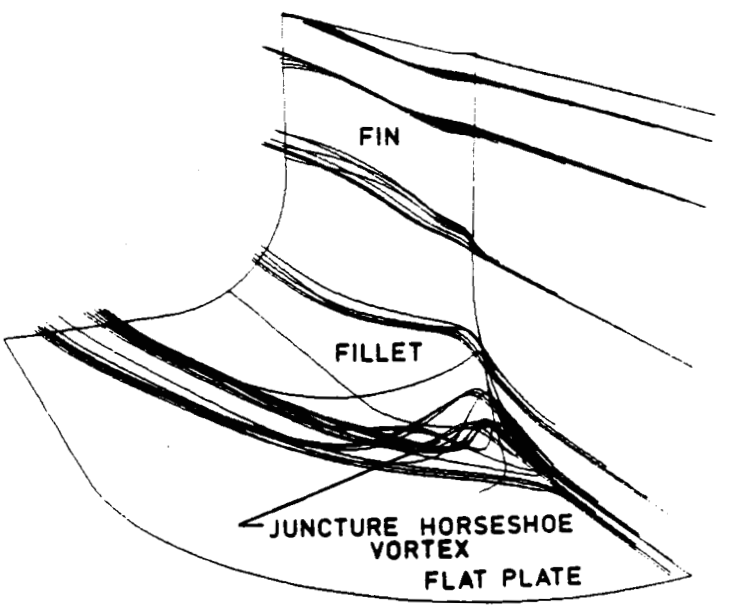

Fig. 6.43(continued) (c) circular fillet ($\delta/D = 2$, $R/D = 3.5$)

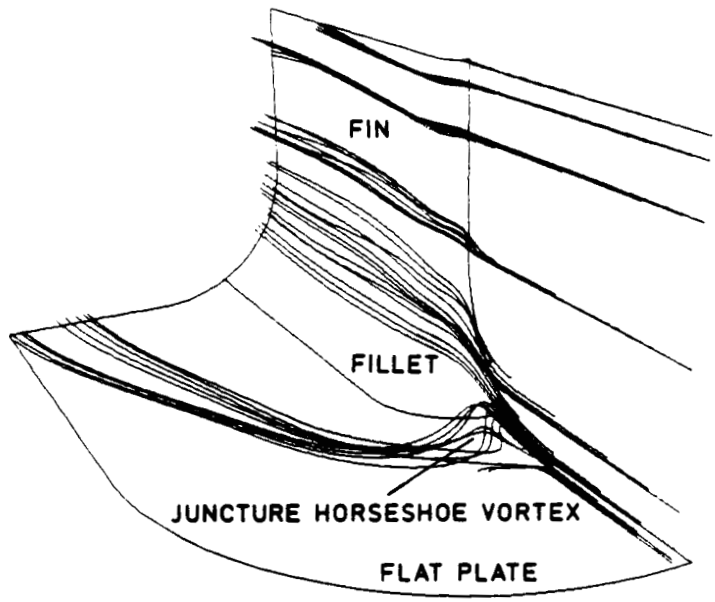

Fig. 6.43(continued) (d) circular fillet ($\delta/D = 0.2$, $R/D = 3.5$)

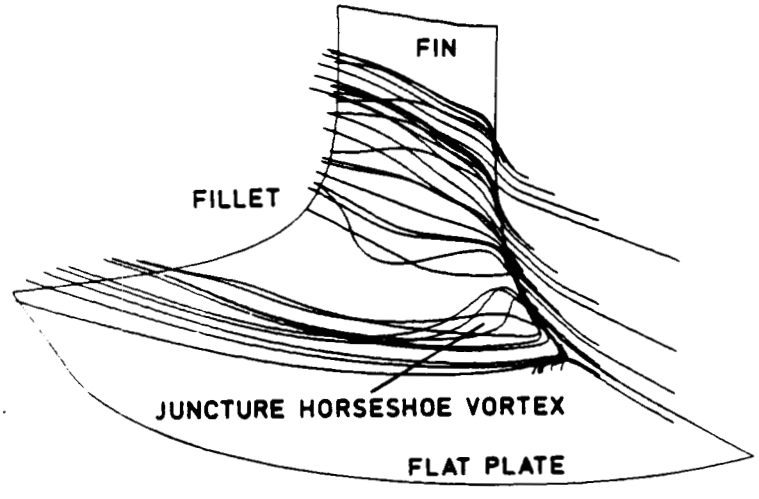

Fig. 6.43(continued) (e) continuous fillet ($\delta/D = 2$)

C-3

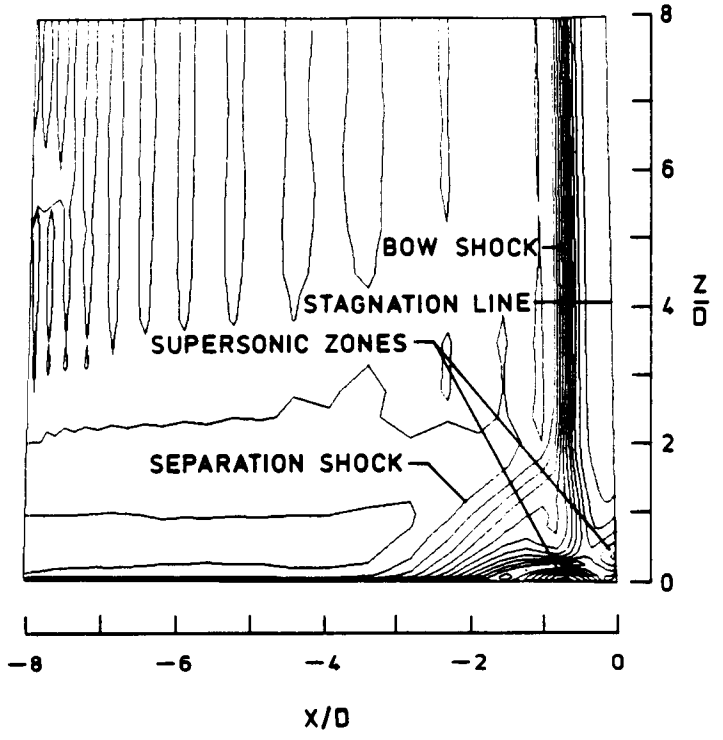

Fig. 6.44 Velocity magnitude contours in the plane of symmetry for various junctions: (a) unmodified junction ($\delta/D = 2$)

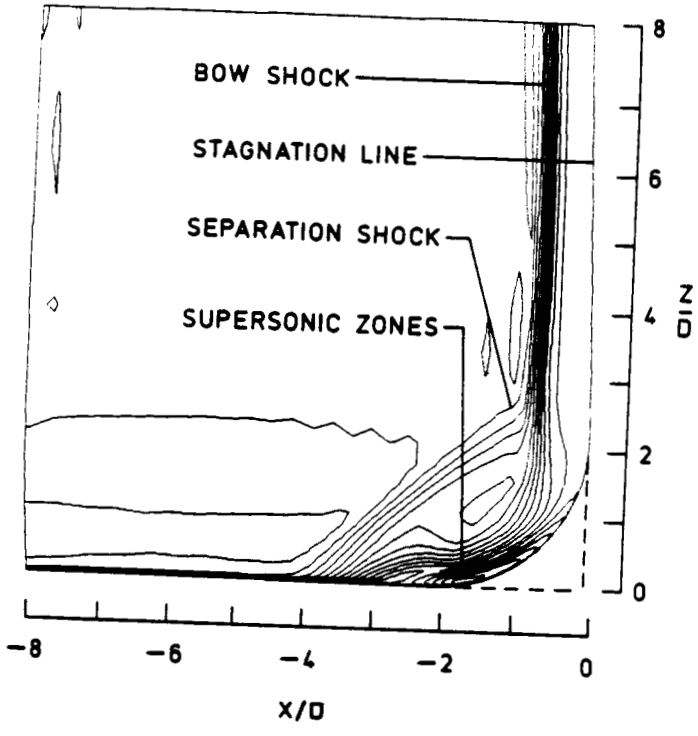

Fig. 6.44(continued) (b) circular fillet ($\delta/D = 2$, $R/D = 2$)

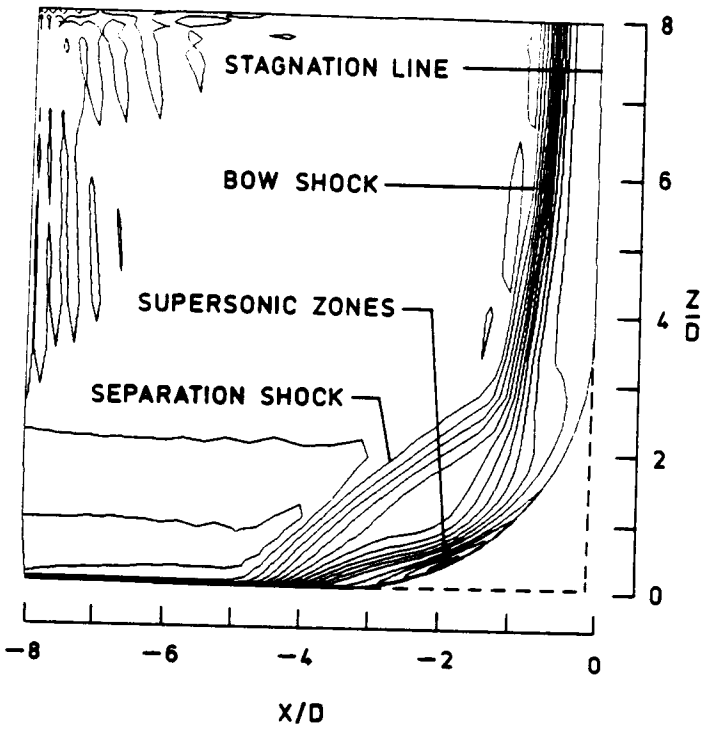

Fig. 6.44(continued) (c) circular fillet ($\delta/D = 2$, $R/D = 3.5$)

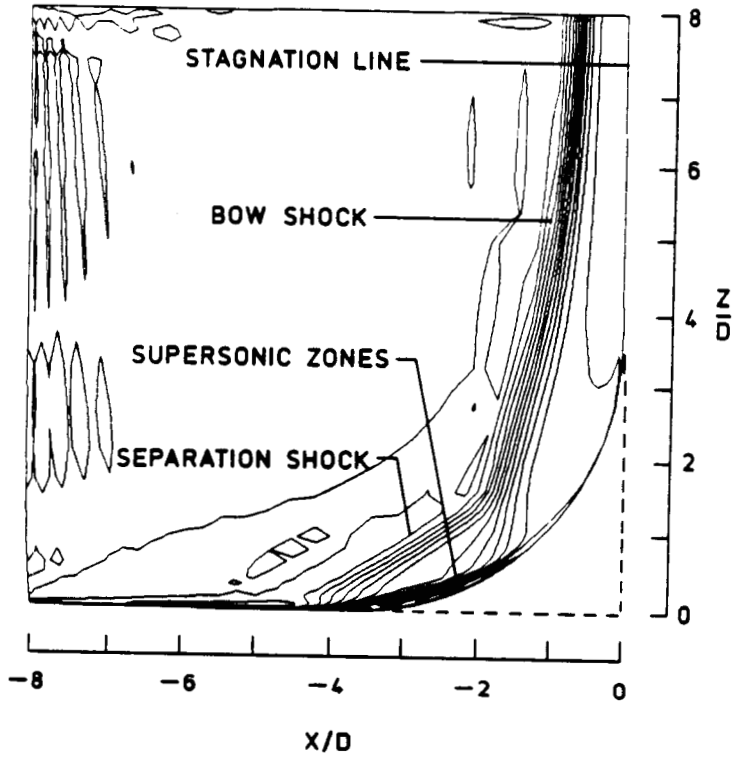

Fig. 6.44(continued) (d) circular fillet ($\delta/D = 0.2$, $R/D = 3.5$)

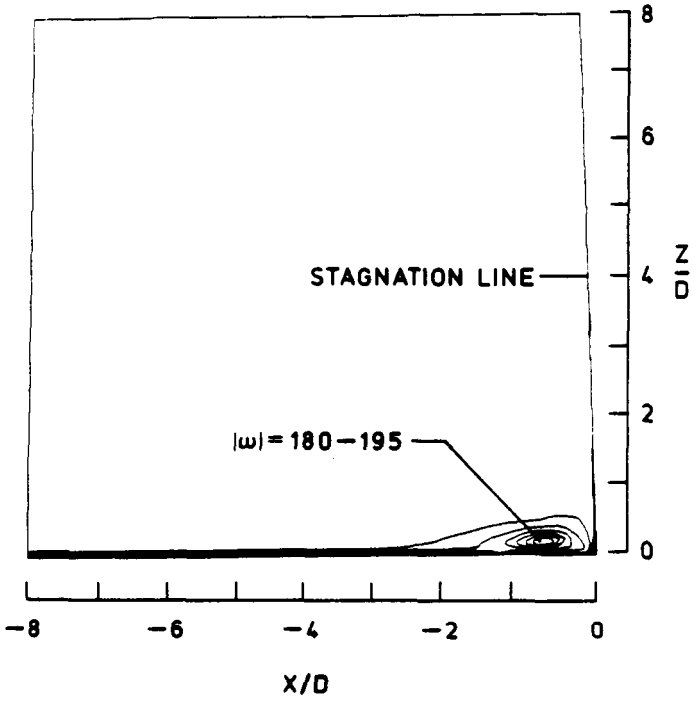

Fig. 6.45 Vorticity contours in the plane of symmetry for various functions: (a) unmodified junction ($\delta/D = 2$)

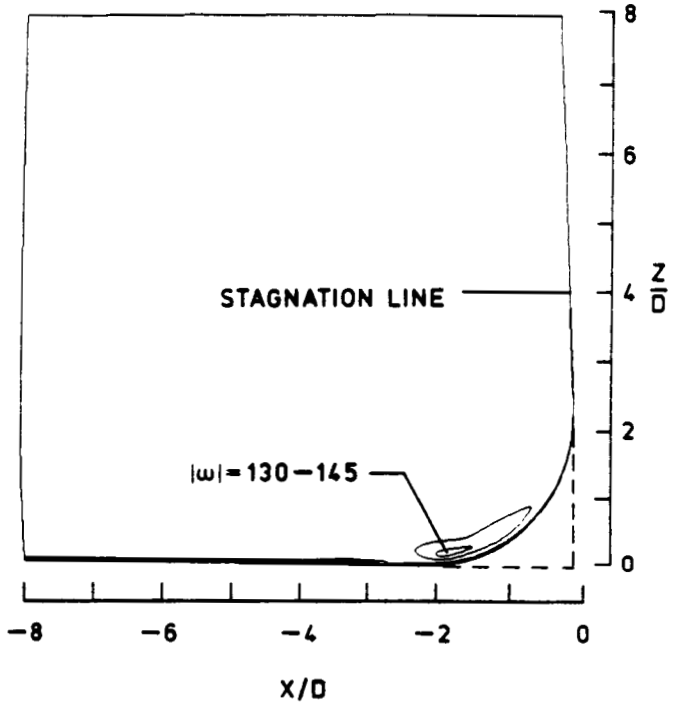

Fig. 6.45(continued) (b) circular fillet ($\delta/D = 2$, $R/D = 2$)

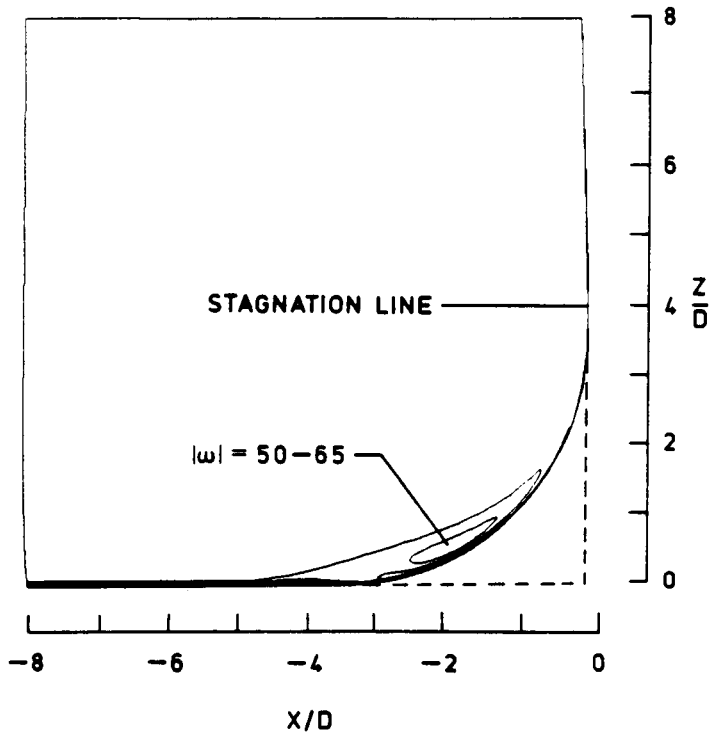

Fig. 6.45(continued) (c) circular fillet ($\delta/D = 2$, $R/D = 3.5$)

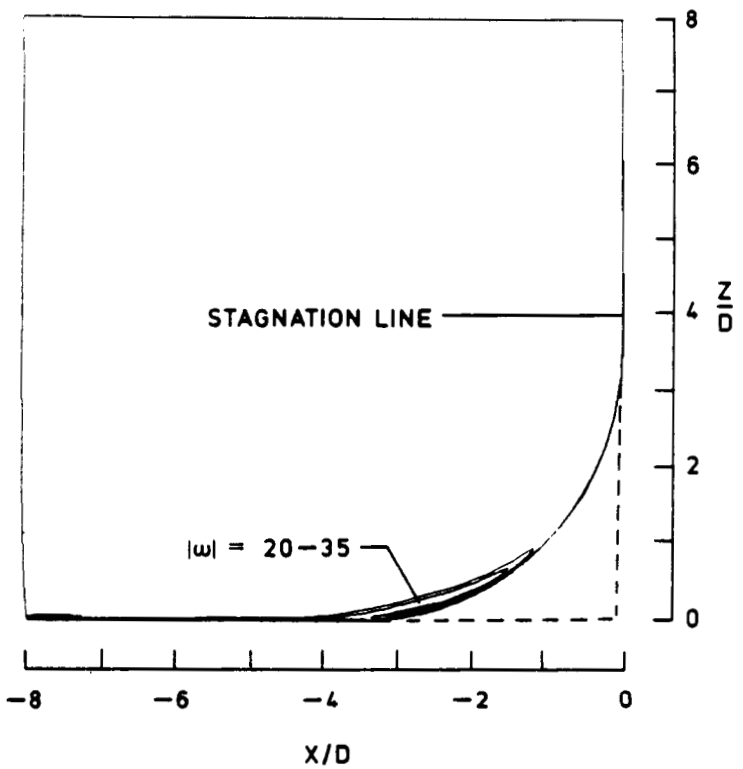

Fig. 6.45(continued) (d) circular fillet ($\delta/D = 0.2$, $R/D = 3.5$)

Chapter 7

CONCLUSIONS AND RECOMMENDATIONS

The supersonic flow past a wing/body junction is simulated numerically using a three-dimensional Navier-Stokes code. Results have been obtained for simplified geometries such as blunt fin/flat plate junction, sharp fin/flat plate junction, and filleted junction. Extensive parametric studies of grid resolution, Mach and Reynolds number variation have been conducted to understand their effects in modifying the interaction flow field. The influence of fillets and sweep on the computed flow field have been investigated extensively for a wide range of geometrical and flow conditions. In general, the computational results show that better agreement with experimental results can be obtained by refining the mesh. It has been noted that the fin sweep reduces considerably the spanwise extent of the interaction flow field. Some improvements in surface temperature are also observed due to sweep. The computed particle paths and limiting streamlines for swept junctions demonstrate clearly the dramatic influence of fin sweep in weakening the juncture horseshoe vortex. The results for sharp fin/flat plate junction show that the structure of three-dimensional separation is markedly different from that exhibited by the blunt fin/flat plate junction. The numerical study of filleted junctures clearly show that the flow streamlines lose much of their vortical character with proper filleting. It has been demonstrated that fillets with a radius of three and one-half times the fin

leading edge diameter are required to weaken the usual necklace vortex interaction for the Mach number and Reynolds number considered in the present study.

Based upon the present study, the following areas of research may be identified for further studies:

1. The sensitivity of grid refinement on the computed flow structure should be investigated using a much finer grid than used in the present study to define the minimum number of grid points required for an accurate resolution of flow features.
2. The simulated structure of the shock is smeared due to the nature of the algorithm applied in the present study. A numerical technique, such as a high resolution TVD scheme, can be incorporated in the code for providing a crisp representation of the shock.
3. The flow structure should be examined for physical conditions when there are four or more vortices present in the flow field.
4. The effect of changes in the turbulence model, such as a nonlinear k- model, can be examined to investigate its effect on the flow field simulation.
5. Since the flow is unsteady, one should investigate the oscillatory behavior of the horseshoe vortex.
6. It would be desirable to examine the chemistry and real gas effects using appropriate mathematical models.

REFERENCES

1. Norman, R.S., "On Obstacle Generated Secondary Flows in Laminar Boundary Layers and Transition to Turbulence," Ph.D Thesis, Illinois Institute of Technology, Chicago, December 1972.

2. Schwind, R., "The Three-Dimensional Boundary Layer Near a Strut," MIT Gas Turbine Laboratory Report, 1962.

3. Baker, C.J., "The Laminar Horseshoe Vortex," Journal of Fluid Mechanics, Vol. 95, Part 2, November 1979, pp. 347-367.

4. Kaul, U.K., Kwak, D., and Wagner, C., "A Computational Study of Saddle Point Separation and Horseshoe Vortex System," AIAA Paper 85-0182, January 1985.

5. Shabaka, I.M.M.A., "Turbulent Flow in a Simulated Wing/Body Junction," Ph.D Thesis, Imperial College, London, April 1979.

6. Shabaka, I.M.M.A. and Bradshaw, P., "Turbulent Flow in an Idealized Wing-Body Junction," AIAA Journal, Vol. 19, No. 12, February 1981, pp. 131-132.

7. Oguz, E. A., "An Experimental Investigation of the Turbulent Flow in the Junction of a Flat Plate and a Body of Constant Thickness," Ph.D Thesis, Georgia Institute of Technology, 1981.

8. McMahon, H., Hubbartt, J. and Kubendran, L., "Mean Velocities and Reynolds Stresses in a Junction Flow," NASA CR-3605, August 1982.

9. Hsing, T.D., and Teng, H.Y., "Experimental Study of the Behavior of 3-D Turbulent Boundary Layer in a Simplified Wing/Body Junction," AIAA Paper 84-1529, June 1984.

10. Briley, W.R. and McDonald, H., "Computation of Three-Dimensional Horseshoe Vortex Flow Using the Navier-Stokes Equations," Proceedings of the Seventh International Conference on Numerical Methods in Fluid Dynamics (W.C. Reynolds and R.W. MacCormack, Editors), Springer-Verlag, 1981, pp. 91-98.

11. Kubendran, L.R. and Harvey, W.D., "Juncture Flow Control Using Leading-Edge Fillets," AIAA Paper 85-4097, October 1985.

12. Mehta, R.D., "Effect of Wing Nose Shape on the Flow in a Wing/Body Junction," Aeronautical Journal, Vol. 88, December 1984, pp. 456-460.

13. Sung, C.H. and Lin, C.W., "Numerical Investigation on the Effect of Fairing on the Vortex Flows Around Airfoil/Flat-Plate Juncture," AIAA Paper 88-0615, January 1988.

14. Kubendran, L., Sung, C.H. and Yang, C.I., "Experiments and Code Validation for Juncture Flows," AGARD-CP-437, May 1988, Vol. 2, pp. 11.1-11.11.

15. Korkegi, R.H., "Survey of Viscous Interaction Associated with High Mach Number Flight," AIAA Journal, Vol. 9, May 1971, pp. 771-784.

16. Young, F.L., Kaufmann, L.G., and Korkegi, R.H., "Experimental Investigation of Interaction Between Blunt Fin Shock Waves and Adjacent Boundary-Layers at Mach Numbers 3 and 5," Aerospace Research Laboratories, ARL 68-0214, December 1968.

17. Price, A.E. and Stallings, R.L., "Investigation of Turbulent Separated Flows in the Vicinity of Fin Type Protuberances at Supersonic Mach Numbers," NASA TN D-3804, February 1967.

18. Westkaemper, J.C., "Turbulent Boundary Layer Separation Ahead of Cylinders," AIAA Journal, Vol. 6, July 1968, pp. 1352-1355.

19. Sedney, R., "A Survey of the Effects of Small Protuberances on Boundary Layer Flows," AIAA Journal, Vol. 11, June 1973, pp. 782-792.

20. Sedney, R. and Kitchens, C.W. Jr., "Separation Ahead of Protuberances in Supersonic Turbulent Boundary Layers," AIAA Journal, Vol. 15, April 1977, pp. 546-552.

21. Voitenko, D.M., Zubkov, A.I., and Panov, Y.A., "Supersonic Gas Flow Past a Cylindrical Obstacle on a Plate," Mekhanika Zhidkosti Gaza, Vol. 1, January/February 1966, pp. 121-125.

22. Voitenko, D.M., Zubkov, A.I., and Panov, Yu A., "Influence of Mach Number on Flow in a Three-Dimensional Separation Region," Moscow University Bulletin, Ser. I, Mathematics and Mechanics, Vol. 23, No. 2, 1968, pp. 115-118.

23. Uselton, J.C., "Fin Shock-Boundary Layer Interaction Tests on a Flat Plate with Blunted Fins at M = 3 and 5," Arnold Engineering Development Center-TR-67-113, June 1967.

24. Lucas, E.J., "Investigation of Blunt Fin-Induced Flow Separation Region on a Flat Plate at Mach Numbers 2.5 to 4.0," Arnold Engineering Development Center-TR-70-265, January 1971.

25. Kaufman, L.G., Korkegi, R.H., and Morton, L.C., "Shock Impingement Caused by Boundary Layer Separation Ahead of Blunt Fins," Aeronautical Research Lab., ARL 72-0118, August 1972.

26. Dolling, D.S., Cosad, C.D., and Bogdonoff, S.M., "An Examination of Blunt Fin-Induced Flows," AIAA Paper 78-159, January 1978.

27. Dolling, D.S., Cosad, C.D., and Bogdonoff, S.M., "An Examination of Blunt Fin-Induced Shock Wave Turbulent Boundary Layer Interactions," AIAA Paper 79-0068, January 1979.

28. Winkelman, A.E., "Experimental Investigations of a Fin Protuberance Partially Immersed in a Turbulent Boundary Layer at Mach 5," (Naval Ordinance Laboratory), NOLTR-72-33, January 1972.

29. Gillerlain, J.D., "Fine-Cone Interference Flow Field," AIAA Paper 79-0200, January 1979.

30. Dolling, D.S. and Bogdonoff, S.M., "Blunt Fin-Induced Shock Wave/Turbulent Boundary-Layer Interaction," AIAA Journal, Vol. 20, No. 12, December 1982, pp. 1674-1680.

31. Hung, C.M. and Buning, P.G., "Simulation of Blunt-Fin Induced Shock-Wave and Turbulent Boundary-Layer Interaction," Journal of Fluid Mechanics, Vol. 154, May 1985, pp. 163-185.

32. Hung, C.M., "Computation of Separation Ahead of Blunt Fin in Supersonic Turbulent Flow," NASA TM-89416, December 1986.

33. Stollery, J.F., Fomison, N.R., and Hussain, S., "The Effects of Sweep and Bluntness on Glancing Interactions at Supersonic Speeds," 15th Congress of the International Council of the Aeronautical Sciences, September 1986.

34. Gaitonde, D. and Knight, D., "Numerical Experiments on the 3-D Shock Wave-Boundary Layer Interaction Generated by a Sharp Fin," AIAA Paper 88-0309, January 1988.

35. Baldwin, B.S. and Lomax, H., "Thin Layer Approximation and Algebraic Model for Separated Turbulent Flows," AIAA Paper 78-257, January 1978.

36. Jones, W.P. and Launder, B.E., "The Prediction of Laminarization with a Two-Equation Model of Turbulence," International Journal of Heat and Mass Transfer, Vol. 15, February 1972, pp. 301-314.

37. Gorski, J.J., "Computation of the Turbulent Flow in the Corner of a Wing/Body Junction," M.S. Thesis, Department of Aerospace Engineering, Pennsylvania State University, University Park, December 1983.

38. Hanjalic, K. and Launder, B.E., "A Reynolds Stress Model of Turbulence and its Applications to Asymmetric Shear Flows," Journal of Fluid Mechanics, Vol. 52, April 1972, pp. 609-638.

39. Gorski, J.J., Govindan, T.R., and Lakshminarayana, B., "Computation of Three-Dimensional Turbulent Shear Flows in Corners," AIAA Journal, Vol. 23, May 1985, pp. 685-692.

40. Hung, C.M. and Kordulla, W., "A Time-Split Finite-Volume Algorithm for Three-Dimensional Flow Field Simulation, AIAA Journal, Vol. 22, No. 11, November 1984, pp. 1564-1572.

41. Hung, C.M. and MacCormack, R.W., "Numerical Solution of Three-Dimensional Shock Wave and Turbulent Boundary-Layer Interaction," AIAA Journal, Vol. 16, October 1978, pp. 1090-1096.

42. Buleev, N., "Theoretical Model of the Mechanism of Turbulent Exchange in Fluid Flows," Atomic Energy Research Establishment, AERE Translation, Hartwell, England, 1963.

43. Gersner, F., and Po, J., "A Reynolds Stress for Turbulent Corner Flows - Part II: Comparisons Between Theory and Experiment, Journal of Fluids Engineering, Transaction of ASME, Vol. 98, Series I No. 2, June 1976, pp. 269-277.

44. Thomas, P.D. and Middlecoff, J.F., "Direct Control of the Grid Point Distribution in Meshes Generated by Elliptic Equations," AIAA Journal, Vol. 18, No. 6, June 1980, pp. 652-656.

45. Harris, J.E. and Blanchard D.K., "Computer Program for Solving Laminar, Transitional, or Turbulent Compressible Boundary-Layer Equations for Two-Dimensional and Axisymmetric Flow," NASA TM-83207, February 1980.

46. Pulliam, T.H. and Steger, J.L., "Implicit Finite-Difference Simulations of Three-Dimensional Compressible Flow," AIAA Journal Vol. 18, February 1980, pp. 159-167.

47. Rizk, Y.M., Chaussee, D.S., and McRae, D.S., "Numerical Simulation of Viscous-Inviscid Interactions on Indented Nose Tips," AIAA Paper 82-0290, January 1982.

48. MacCormack, R.W., "A Numerical Method for Solving the Equations of Compressible Viscous Flow," AIAA Journal, Vol. 20, September 1982, pp. 1275-1281.

49. Kordulla, W. and Vinokur, M., "Efficient Computation of Volume in Flow Predictions," AIAA Journal, Vol. 21, June 1983, pp. 917-918.

50. Strang, G., "On the Construction and Comparison of Difference Schemes," SIAM Journal of Numerical Analysis, Vol. 5, September 1968, pp. 506-517.

51. Baldwin, B.S., and MacCormack, R., "A Numerical Method for Solving the Navier-Stokes Equations With Application to Shock Turbulent Boundary Layer Interaction," AIAA Paper No. 75-1, January 1975.

52. Özcan, O. and Holt, M.," Supersonic Separated Flow Past a Cylindrical Obstacle on a Flat Plate," AIAA Journal, Vol. 22, No. 5, May 1984, pp. 611-617.

53. Peake, D.J., "Three Dimensional Swept Shock/Turbulent Boundary Layer Separations with Control by Air Injection," National Research Council-Canada, July 1976.

54. Shapey, B., "3-D Shock Wave/Turbulent Boundary Layer Interaction for a 20° Sharp Fin at Mach 3" MSE Thesis, Mechanical and Aerospace Engineering Department, Princeton Unversity, Princeton, New Jersey, October 1986.

55. Edney, B., "Anomalous Heat Transfer and Pressure Distributions on Blunt Bodies at Hypersonic Speeds in the Presence of an Impinging Shock," Aeronautical Research Institute of Sweden, Stockholm, Sweden, Rept. 115, February 1968.

56. Horstman, C. and Hung, C.M., "Computation of Three Dimensional Turbulent Separated Flows at Supersonic Speeds," AIAA Paper No. 79-0002, January 1979.

57. Knight, D. Horstman, C., Shapey, B., and Bogdonoff, S.M., "The Flowfield Structure of the 3D Shock Wave-Boundary Layer Interaction Generated by 20° Sharp Fin at Mach 3," AIAA Paper 86-0343, January 1986.

58. McClure, W. and Dolling, D., "Flowfield Scaling in Sharp Fin-Induced Shock Wave Turbulent Boundary Layer Interaction," AIAA Paper 83-1754, July 1983.

59. Settles, G. and Bogdonoff, S., "Scaling of Two- and Three-Dimensional Shock/Turbulent Boundary-Layer Interactions at Compression Corners," AIAA Journal, Vol. 20, June 1982, pp. 782-789.

60. Dolling, D. and Bogdonoff, S., "Upstream Influence Scaling of Sharp Fin-Induced Shock Wave Turbulent Boundary Layer Interactions," AIAA Paper 81-0336, January 1983.

61. Lu, F. and Settles, G., "Conical Similarity of Shock/Boundary Layer Interactions Generated by Swept Fins," AIAA Paper 83-1756, July 1983.

62. Lakshmanan, B. and Tiwari, S.N., "Performance of a Three-Dimensional Navier-Stokes Code on Cyber 205 for High-Speed Juncture Flows," ASME Fluids Engineering Conference, Proceedings on Applications of Parallel Processing in Fluid Mechanics, FED-Vol. 47, June 1987, pp. 65-74.

63. Lakshmanan, B. and Tiwari, S.N., "Investigation of a Three-Dimensional Flow Field at a Wing/Body Junction," Deartment of Mechanical Engineering and Mechanics, College of Engineering and Technology, Old Dominion University, Norfolk, Virginia, TR NAS-1-17993-03, October 1987.

APPENDIX A

MAXIMUM ALLOWABLE TIME STEP FOR EXPLICIT ALGORITHM

An approximate linearized stability analysis [51] yields the following:

$$\Delta t_{\xi_{CFL}} = CFL \min_{i,J,k} \Delta t_{\xi}$$

$$\Delta t_{\eta_{CFL}} = CFL \min_{i,J,k} \Delta t_{\eta} \qquad (A.1)$$

$$\Delta t_{\zeta_{CFL}} = CFL \min_{i,J,k} \Delta t_{\zeta}$$

where $\min_{i,J,k}$ denotes the minimum value evaluated over all grid volumes which are updated by the explicit scheme, and

$$\Delta t_{\xi} = \frac{\Delta S_{\xi}}{|u_{\xi}| + a + \frac{2\theta}{\Delta S_{\eta}\rho}} \qquad (A.2)$$

$$\Delta t = \frac{\Delta S_{\eta}}{|u_{\eta}| + a + \frac{2\theta}{\Delta S_{\eta}\rho}} \qquad (A.3)$$

$$\Delta t = \frac{\Delta S_\zeta}{|u_\zeta| + a + \frac{2\theta}{\Delta S_\zeta \rho}} \tag{A.4}$$

$$\begin{aligned} \Delta S_\xi &= \Delta\xi / \sqrt{\xi_x^2 + \xi_y^2 + \xi_z^2} \\ \Delta S_\eta &= \Delta\eta / \sqrt{\eta_x^2 + \eta_y^2 + \eta_z^2} \\ \Delta S_\zeta &= \Delta\zeta / \sqrt{\zeta_x^2 + \zeta_y^2 + \zeta_z^2} \end{aligned} \tag{A.5}$$

and

$$\begin{aligned} u_\xi &= (u\,\xi_x + v\,\xi_y + w\,\xi_z) / \sqrt{\xi_x^2 + \xi_y^2 + \xi_z^2} \\ u_\eta &= (u\,\eta_x + v\,\eta_y + w\,\eta_z) / \sqrt{\eta_x^2 + \eta_y^2 + \eta_z^2} \\ u_\zeta &= (u\,\zeta_x + v\,\zeta_y + w\,\zeta_z) / \sqrt{\zeta_x^2 + \zeta_y^2 + \zeta_z^2} \end{aligned} \tag{A.6}$$

and

$$\theta = \max \left| 2(\mu+\xi) - \lambda \right|, \nu \left(\frac{\mu}{Pr} + \frac{\varepsilon}{P_{r_t}} \right) \tag{A.7}$$

The constant CFL is typically chosen to be 0.9.

AUTOBIOGRAPHICAL STATEMENT

The author was born on August 27, 1957 in Madras, India. He received his Bachelor's degree in Mechanical Engineering from Bhopal University, India in August 1979. He came to the United States of America in August 1980 to pursue higher education. He graduated with a Master's degree in Mechanical Engineering from Old Dominion University in May 1983. In August 1983, he enrolled in the Doctoral program in Mechanical Engineering at the Old Dominion University. During his graduate studies, the author was involved in research work pertaining to applied computational fluid dynamics sponsored by the Naval Air Development Center and the NASA Langley Research Center.